

Measurements of Higher-Order Cumulants
of Net-Proton Distributions
in 200 GeV $p + p$ Collisions at RHIC-STAR

Risa Nishitani

February 2022

Measurements of Higher-Order Cumulants
of Net-Proton Distributions
in 200 GeV $p + p$ Collisions at RHIC-STAR

Risa Nishitani
Doctral Program in Physics

Submitted to the Graduate School of
Pure and Applied Sciences
in Partial Fulfillment of the Requirements
for the Degree of Doctor of Philosophy in
Science

at the
University of Tsukuba

Abstract

The phase structure of the matter of quarks and gluons has been conjectured by many theories, which is depicted as quantum chromodynamics (QCD) phase diagram with respect to temperature (T) and baryon chemical potential (μ_B). Lattice QCD calculations predict a smooth crossover transition from the hadronic gas to a deconfined state in which quarks and gluons are free to move by weak coupling, so-called Quark-Gluon Plasma (QGP) at $\mu_B = 0$. On the other hand, the first-order phase transition is predicted at large μ_B region. The connecting point between the first-order phase boundary and crossover is called a QCD critical point.

The higher-order cumulant of conserved quantities is a powerful tool to probe the QCD phase structure. Various orders of cumulants of conserved quantities such as the number of net baryons, charge, and strangeness are expected to be proportional to the correlation length which diverges near the critical point. Furthermore, the fourth-order susceptibilities given by Lattice calculations predict a characteristic enhancement near the critical point. Experimentally, to understand the QGP properties and QCD phase structure, a hot and dense matter has been created by colliding two heavy ions. The Relativistic Heavy Ion Collider (RHIC) at Brookhaven National Laboratory (BNL) is one of the heavy-ion colliders. To explore the critical point and phase transition, the Beam Energy Scan program has been carried out in the RHIC-STAR experiment for Au+Au collisions from 7.7 to 200 GeV in center-of-mass energy. Through recent measurements on the fourth- and sixth-order cumulants of net-proton multiplicity distribution, it was found that the critical point could exist between $2.4 < \sqrt{s_{NN}} < 7.7$ GeV, and the phase transition at $\mu_B = 25$ GeV could be a smooth crossover.

Several signals of QGP formation have been observed in Au+Au collisions, on the other hand, it is still not clear whether the QGP is created in the small system such as high multiplicity events of $p+p$ or $p+A$ collisions. The strangeness enhancement and flow have been studied in $p+p$ collisions, while the results indicate that the signal of QGP formation is very uncertain. The fluctuation of conserved quantities is a new viewpoint to explore the phase transition signal. In this study, precise measurements of higher-order cumulants of net-proton number distributions were performed for $p+p$ collisions to determine physics baselines to be compared to those from Au+Au collisions. The goal of this study is to verify the possibility of phase transitions in high multiplicity events of $p+p$ collisions.

A lot of datasets have been analyzed to measure higher-order cumulants for Au+Au collisions, while this is the first time to measure the cumulants for $p+p$ collisions. We found that the particle multiplicity is significantly affected by pileup events (superposition of more than one single collision events) in $p+p$ collisions. This issue was taken care of in two ways: by applying scaling corrections as a function of luminosity, or by defining luminosity-independent particle multiplicity. The cumulants and their ratios are compared with statistical baseline and PYTHIA 8 calculations. The higher-order cumulants deviate from the statistical baselines at high multiplicity and the PYTHIA 8 calculations can not reproduce the multiplicity dependence for both ways. The multiplicity dependence of the cumulant ratios shows different trends for the two ways. PYTHIA 8 calculations can reproduce the multiplicity dependence with the later way for most order of cumulant ratios. Based on the agreement of cumulants among different luminosity groups, the later way was employed.

Acceptance and multiplicity dependence of cumulants and the ratios of net-proton distributions were measured up to the sixth-order in $p+p$ collisions at $\sqrt{s} = 200$ GeV. The acceptance $|y|$ and p_T dependence of cumulants and their ratios are below the statistical baselines and the deviations increase with increasing the rapidity and transverse momentum acceptance. The PYTHIA 8 calculations for cumulants increase with increasing acceptance and deviate from the Skellam, while PYTHIA 8 do not reproduce the observed values of both the observed cumulants and their ratios. The assumption of baryon number conservation within full phase space does not reproduce the deviation of normalized second-order cumulant for both observed and PYTHIA 8, which indicates the origin of the deviation of the observed result is beyond the effect of baryon number conservation. For the multiplicity dependence, observed cumulants up to fourth-order show increasing trends, while the increasing of fifth- and sixth-order cumulants are suppressed at high multiplicity. Values of sixth-order cumulant were found to stay positive, while they show decreasing trend with increasing of multiplicity. The observed cumulants and their ratios deviate from Skellam except for first-order cumulants and the larger deviations are shown in higher-order. The PYTHIA 8 calculation of C_4/C_2 , C_5/C_1 and C_6/C_2 show decreasing trends with peaks near the mean

multiplicity, which qualitatively reproduces the observed trend, while PYTHIA 8 do not overlap the observed multiplicity dependence and average values for most order of cumulants even if the effect of color reconnection is considered. The average values show $C_5/C_1 > 0$ and $C_6/C_2 > 0$ for $p+p$ collisions, while $C_5/C_1 < 0$ and $C_6/C_2 < 0$ for central Au+Au collisions. Furthermore, the results from $p+p$ collisions fit into the centrality dependence of Au+Au collisions at the same energy. Lattice QCD calculations show that the negative signs of fifth- and sixth-order cumulants indicate the chiral phase transition in the thermalized QCD matter. In the results for $p+p$ 200 GeV collisions, the values show decreasing from positive value and show significantly small values at high multiplicity.

Contents

1	Introduction	14
1.1	Quantum chromodynamics (QCD)	14
1.1.1	Asymptotic freedom	14
1.1.2	Confinement	14
1.2	QCD phase diagram	15
1.3	Observables	15
1.3.1	Definition	15
1.3.2	Properties	17
1.3.3	Statistical baseline	18
1.4	Experimental results on the QCD phase structure	19
1.4.1	QCD critical point	19
1.4.2	Crossover search	19
1.5	Indication of QGP droplet in small systems	21
1.6	Motivation	23
2	Experiment	24
2.1	Relativistic Heavy Ion Collider (RHIC)	24
2.2	The STAR Experiment	24
2.2.1	The Time Projection Chamber (TPC)	25
2.2.2	The Time of Flight (TOF)	27
2.2.3	Other sub-systems	28
2.3	Beam Energy Scan program	30
3	Analysis	32
3.1	Datasets	32
3.1.1	Event selection	32
3.1.2	Track selection	33
3.1.3	Particle identification	34
3.1.4	Event categorization	35
3.1.5	Run-by-run Quality Assurance (QA)	36
3.2	Efficiency correction	39
3.3	Centrality Bin Width Correction (CBWC)	41
3.4	Statistical uncertainties	42
3.5	Effect of pileup events	43
3.5.1	Effect of pileup events on cumulants	44
3.5.2	Effects of pileup events on TOF matching efficiencies	44
3.5.3	Effects of pileup events on (anti)protons	45
3.5.4	Luminosity correction of multiplicity	46
3.5.5	The necessary number of bins in net-proton distribution	52
3.5.6	Luminosity dependent efficiency correction	53
3.6	Systematic uncertainties	56
3.6.1	Barlow check	58

4	Results	60
4.1	Acceptance dependence of cumulants	60
4.2	Multiplicity dependence of net-proton cumulants	64
4.3	Luminosity independent multiplicity	66
5	Discussions	69
5.1	Effects of pions from Λ decay on multiplicity	69
5.2	Baryon number conservation	70
5.3	Pileup model	73
5.4	Comparison with Au+Au collision	76
6	Summary	78
A	Event and track selection	80
A.1	Run-by-run QA	80
A.2	Luminosity dependence of event and track variables	83
B	Efficiency	85
B.1	Mixed cumulants in efficiency correction	85
B.2	Multiplicity dependence of TOF matching efficiencies	86
B.3	Multiplicity and luminosity dependence of efficiencies	86
C	Theoretical model	89
C.1	Hadron resonance gas (HRG) model	89
C.2	Multiplicity distribution of PYTHIA 8	89
D	Analysis	91
D.1	Number of bins in net-proton distributions	91
	D.1.1 Multiplicity and luminosity dependence of cumulants	97
D.2	Systematic study	99
	D.2.1 Efficiency for DCA and nHitsFit	99
	D.2.2 Cumulants with different cut conditions	102
	D.2.3 Barlow check in systematic study	102
D.3	Luminosity independent multiplicity	121
D.4	TOF matched multiplicity in Au+Au collisions	123

List of Figures

1.1	Illustration of QCD phase diagram with predicted phase transition lines, critical point, and the range of BES collision energies [1].	15
1.2	Illustration of the distributions for third- (left) and fourth-order (right) cumulants with examples of skewness $S = 0, 0.5, 0.8$ and kurtosis $\kappa = 1, 0, -1$, respectively [2].	16
1.3	Temperature dependence of fourth-order fluctuations of number of baryon (χ_4^B), electric charge (χ_4^Q) and strangeness (χ_4^S) [3]. The quantities are respectively normalized by the number of free quarks.	18
1.4	Temperature dependence of the ratio between the fourth- and second-order fluctuation of baryon number. The solid line represents the Hadron Resonance Gas (HRG) model over 100 to 200 MeV.	18
1.5	Collision energy dependence of the $\kappa\sigma^2$ for net-proton distributions in Au+Au collisions at $\sqrt{s_{NN}} = 7.7 - 200$ GeV measured by STAR and $\sqrt{s_{NN}} = 2.4$ GeV measured by HADES experiment [4]. The results are shown for central (0 – 5%) collisions with filled circles and peripheral (70 – 80%) collisions with open squares within $0.4 < p_T < 2.0$ GeV/c and $ y < 0.5$. The statistical and systematic uncertainties are shown in narrow and wide bars, respectively.	19
1.6	Upper panel: A sketch of the κ_4 behavior near the critical point predicted by Lattice QCD. Lower panel: A sketch of the QCD phase diagram with the curve of freezeout and a possible mapping for the Ising coordinates t and H [5].	19
1.7	μ_B/T dependence of the cumulant ratios $R_{51}^B(T, \mu_B)$ and $R_{62}^B(T, \mu_B)$ from leading order (LO) and NLO of Taylor expansions of cumulants on Lattice with $N_\tau = 8$ [6]. Magenta and green bands show the sixth- and fifth-order fluctuations, respectively.	20
1.8	Temperature dependence of the ratios χ_6^B/χ_2^B for various μ_q/T corresponding to values at chemical freeze-out at RHIC [7]. The shaded area shows the chiral crossover region.	20
1.9	Number of participants (N_{part}) dependence of cumulant ratio C_6/C_2 measured in Au+Au collisions. The red marker shows the results measured in collision energy 200 GeV [8].	20
1.10	p_T -integrated yield ratios to pions ($\pi^+ + \pi^-$) as a function of $\langle dN_{ch}/d\eta \rangle$ measured in $ y < 0.5$ [9]. The error bars show the statistical uncertainty. The empty and dark-shaded boxes are the systematic uncertainty and the contribution uncorrelated across multiplicity bins, respectively. The values are compared to calculations from MC models, and results are obtained in p+Pb and Pb+Pb collisions at the LHC. For Pb+Pb results the ratio $2\Lambda/((\pi^+ + \pi^-))$ is shown.	21
1.11	Elliptic flow (v_2) as a function of N_{ch}^{rec} in the 13 TeV $p+p$ collisions measured by ATLAS (left) and CMS (right) experiments [10]. They were measured with different methods for $0.5 < p_T < 5$ GeV/c and $0.3 < p_T < 3$ GeV/c, respectively. The red bands show the calculation of superSONIC. The error bars are statistical uncertainties.	22
1.12	Collision energy dependence of the net-proton $S\sigma$, $\kappa\sigma^2$, and $(S\sigma)/\text{Skellam}$ for $p+p$ and Au+Au collisions [11]. Open squares, filled circles, and crosses are for the efficiency corrected results of 70 – 80%, and 0 – 5% Au+Au collisions, and $p+p$ collisions respectively. Skellam baselines for corresponding collision centralities are shown in the top panel. Shaded hatched bands show UrQMD model calculations. The solid bands in the middle and lower panels are the expectations assumed independent protons productions. The bandwidth shows the statistical uncertainties. The HRG results for middle and lower panels are unity. The bars and caps show statistical and systematic uncertainties, respectively. The values of $p+p$ and Au+Au 70 – 80% are slightly displaced horizontally.	23

2.1	The RHIC complex layout [12].	24
2.2	The sketch of the STAR detector.	25
2.3	Cutaway view of the STAR detector.	25
2.4	The TPC perspective view [13].	26
2.5	Momentum dependence of the dE/dx measured by the TPC in the magnetic field 0.25 T [13].	27
2.6	The particle momentum dependence of mass for deuterons, protons, kaons, and pions are measured as labeled with the time resolution $\Delta t = 100$ ps, path length resolution $\delta L/L = 0.2\%$, and momentum resolution $\delta p/p = 1.3\%$ [14]. The solid and dashed lines indicate the tracks near $\eta \sim 0$ and $\eta \sim 1$, respectively. The pair of upper and lower lines are shown for momentum dependence of $M + \Delta M$ and $M - \Delta M$, respectively.	28
2.7	A cutaway drawing of locations of the TOFP and pVPD with the TPC and the beam pipe [14].	28
2.8	One of the two identical VPD assemblies [14]. The "FEE & TIB" is the Front End Electronics and the Threshold Interface Board.	29
2.9	Cross-sectional view of STAR detector with the Barrel EMC covering $ \eta \leq 1.00$	29
2.10	Side view of the collision region of the ZDC location indicating deflection of protons and charged fragments with $Z/A \sim 1$ downstream of the dipole magnet [15].	30
3.1	Distribution of the z-vertex positions (V_Z) from the center of the TPC along the beamline. The red lines represent the required condition of $V_Z \pm 30$ cm.	32
3.2	Distribution of the vertex horizontal and vertical (V_y) positions in the transverse plane at the center of the TPC.	32
3.3	Difference between z-vertices positions measured by the VPD and TPC.	33
3.4	Multiplicity distribution in $ \eta < 1$ for all charged particles in track fitting except for protons and antiprotons.	33
3.5	Distribution of p_T as a function of y of charged particles. The dotted square shows the kinematic region used for fluctuation analysis.	34
3.6	DCA distribution of the charged particles.	34
3.7	Distribution of the number of hits used in track fitting in the TPC. The red dotted line shows the track cut of 20 hits.	34
3.8	The dE/dx distribution of charged tracks as a function of momentum over charge (p/q). Colored dots show the identified protons by the TPC and TOF depending on transverse momentum. The black bands in the background represent various charged inclusive particles.	35
3.9	The squared mass distribution from the TOF as a function of p/q . Contour points show the identified protons by the TPC and TOF depending on transverse momentum. The black bands in the background represent various charged inclusive particles.	35
3.10	Event-by-event proton and antiproton number distribution at $m_{ch} = 6$ at $0.4 < p_T < 2.0$ GeV/c and $ y < 0.5$.	35
3.11	Event-by-event net-proton number distributions for 3 multiplicity classes. Black filled (cross) markers show the net-proton distribution for $5 \leq m_{ch} < 30$ ($30 \leq m_{ch} < 50$) multiplicity events. Dotted lines are corresponding to $5 \leq m_{ch} < 50$.	35
3.12	Schematic representation of Glauber Model geometry from the side view of the nucleus-nucleus collision.	36
3.13	An illustration of the Glauber Monte-Carlo simulation in a $\sqrt{s_{NN}} = 200$ GeV Au+Au collision with the impact parameter $b = 6$ fm [16]. Left panel: geometry in the transverse plane. Right panel: geometry along the beam axis. Darker disks are participants, and lighter disks are spectator nucleons.	36
3.14	Multiplicity distribution with 13 class for $p+p$ collisions.	36
3.15	Average of event variables as a function of the run index. The red lines represent mean and green dotted lines represent $\mu \pm 3\sigma$. The bracket represents the average value over the event.	37
3.16	Average of track variables measured in the TPC as a function of the run index. The red lines represent mean (μ) and blue dotted lines represent $\mu \pm 3\sigma$. The bracket represents the average value over the event.	38

3.17	Transverse momentum p_T dependence of efficiencies at merged multiplicity over 2 to 30. Black dots and blue triangles show the TPC and TOF efficiency, respectively. Red squares show combined efficiency of them which are used at $0.8 < p_T < 2.0$ GeV/ c . Red dotted lines show the $p_T = 0.4, 0.8, 2.0$ GeV/ c .	40
3.18	Multiplicity dependence of p_T integrated efficiencies for protons and antiprotons. Black dots show the TPC tracking efficiency at $0.4 < p_T < 0.8$ GeV/ c . Red squares show combined efficiencies of the TPC and TOF at $0.8 < p_T < 2.0$ GeV/ c . Solid (open) markers are protons (antiprotons). Blue solid (dotted) lines represent the second-order polynomial function of fitting for protons (antiprotons).	40
3.19	C_n of net-proton distribution in Au + Au collisions at $\sqrt{s_{NN}} = 62.4$ GeV as a function of $\langle N_{part} \rangle$ [17]. The results are shown for 10%, 5%, and 2.5% centrality bins without CBWC and for nine centrality bins (0–5%, 5–10%, 10–20%, ..., 70–80%) with CBWC. The bars are the statistical uncertainties.	41
3.20	C_n of net-proton distribution in $p+p$ collisions at $\sqrt{s} = 200$ GeV as a function of multiplicity. The results of multiplicity bin-by-bin are shown in black dots. The results are shown for 100% (Multiplicity = 5 – 35) and 16% centrality bins without CBWC and for 100%, 20% centrality bins with CBWC. The bars are the statistical uncertainties.	41
3.21	Toy model simulation of fourth-order cumulants ($\langle Q^4 \rangle_c$) with statistical uncertainties calculated by the bootstrap method. The x-axis is the number of independent trials for $\langle Q^4 \rangle_c$ calculations up to 100. Dotted lines show the average value of $\langle Q^4 \rangle_c$ over iteration.	42
3.22	Averaged multiplicity as a function of the ZDC coincidence rate (Hz) at $-2 < V_z < 0$ cm in Au+Au collisions. Blue open diamonds indicate uncorrected multiplicity and red open squares show the corrected results. The red line represents the fitting linear function that is used for the corrections [18].	43
3.23	Averaged multiplicity as a function of the ZDC coincidence rate (Hz). Blue open circles indicate uncorrected multiplicity and red circles show the corrected reference multiplicity. The red line represents the fitting quadratic function that is used for the corrections.	43
3.24	Luminosity grouping in the ZDC coincidence rate as a function of the run. The dotted red lines show the boundary of grouping.	44
3.25	Distributions of absolute DCA value in three luminosity groups.	44
3.26	Multiplicity dependence of first-order cumulants in three luminosity groups.	44
3.27	The TOF matching efficiencies for three luminosity groups in $2 \leq \text{Reference Multiplicity (RefMult)} < 30$. Green, pink, yellow markers show high, middle, low luminosity groups, respectively.	45
3.28	TOF matching efficiencies with the EMC hits requirement for three luminosity groups in $2 \leq \text{Reference Multiplicity (RefMult)} < 30$. High, middle, low luminosity groups are shown in green, pink, yellow, respectively.	45
3.29	ZDC coincidence rate dependence of the average number of protons and antiprotons.	46
3.30	ZDC coincidence rate dependence of the average number of the TOF matched protons and antiprotons.	46
3.31	Distribution of the ZDC coincidence rate. Dotted lines represent the boundary line of 10 groups. Solid lines represent the average in each group.	46
3.32	Distribution of multiplicity for each luminosity group. Each distribution is normalized with the number of events.	47
3.33	The ZDC coincidence rate dependence of average multiplicity over the events. The blue circles show uncorrected data. The red circles are mean corrected results by the fitting of blue data as shown in the red dotted line. The fitting function is second-order polynomial.	48
3.34	Multiplicity distributions and an example of the definition of the distance “ d ”. The yellow and green distributions are measured at luminosity groups #0 and #9, respectively. The areas and heights of them are normalized.	49
3.35	Multiplicity dependence of distance d for luminosity groups #0 and #9, where d is defined by the difference of multiplicities between each i th luminosity groups (“Mult $_{\#i}$ ”) and the lowest luminosity (“Mult $_{\#0}$ ”). The x-axis is the multiplicity for each luminosity. Solid lines show fitting functions using the fourth-order polynomial.	49

3.36	Multiplicity dependence of distance d for luminosity groups #0 to #9. The functions with different colors show the corresponding luminosity groups. The x-axis is the multiplicity for each luminosity.	49
3.37	The ZDC coincidence rate dependence of scale factor $p(\#i)$ for i th luminosity groups. Red dotted lines show fitting functions using the second-order polynomial.	49
3.38	The distribution of luminosity corrected multiplicity for each luminosity group.	50
3.39	Shape corrected multiplicity distribution for each luminosity group. The area of the distributions is normalized to 1.	50
3.40	Multiplicity dependence of C_2 for each luminosity. The highest multiplicity values are merged over $27 \leq \text{Multiplicity} < 50$	50
3.41	Mean corrected multiplicity dependence of C_2 for each luminosity. The highest multiplicity values are merged over $18 \leq \text{Multiplicity} < 30$. Black solid squares show the average over luminosity with $1/\sigma^2$ weighting.	51
3.42	Shape corrected multiplicity dependence of C_2 for each luminosity. Multiplicities are merged from 18 to 30. The highest multiplicity values are merged over $25 \leq \text{Multiplicity} < 40$. Black solid squares show the average over luminosity with $1/\sigma^2$ weighting.	51
3.43	χ^2 distribution of C_2 with mean correction of multiplicity.	51
3.44	χ^2 distribution of C_2 with shape correction of multiplicity.	51
3.45	Net-proton distributions with 5, 6, 7 bins (upper panels) from left to right and bootstrap C_6 distributions from upper net-proton distribution with 5, 6, 7 bins (bottom panels) at $m_{ch} = 19$ in luminosity group #9, 8, 7, respectively.	52
3.46	Relationship between the number of bins (5, 6, 7 bins) of net-proton distribution and the average value of statistical uncertainties for C_6 over 10 luminosity groups at $18 < m_{ch} \leq 22$	52
3.47	Multiplicity distribution with 14 class for $p+p$ collisions.	53
3.48	Luminosity-dependent efficiencies as a function of multiplicity for proton at low p_T . The solid line represents the linear fitting function.	53
3.49	ZDC coincidence rate dependence of (anti)proton cumulants up to C_6 . Open and solid black markers show efficiency uncorrected and corrected cumulants, respectively. Solid blue markers show cumulants which are corrected by modified efficiencies. Diamond, circle, cross, and square indicate proton at low p_T , antiproton at low p_T , proton at high p_T , and antiproton at high p_T , respectively.	54
3.50	ZDC coincidence rate dependence of net-proton cumulants up to C_6 . Open and solid black squares show efficiency uncorrected and corrected cumulants, respectively. Solid blue squares show cumulants which are corrected by modified efficiencies.	55
3.51	The averaged value of C_4/C_2 over multiplicity with each cut condition. Each panels show different variables, $ n\sigma_P $, DCA, nHitsFit, m^2 , Efficiency, and Luminosity from top left to bottom right panel. The squares with different colors are each cut shown in the legends. The black stars show the C_4/C_2 with default cuts.	57
3.52	Distributions of Δ/σ_{sc} for net-proton cumulants up to sixth-order with $ n\sigma_P < 2.1$ cuts. Black dotted lines show the mean of the distributions. Red and blue dotted lines show 1σ and 2σ of the distribution, respectively. For each panel, the results of the 4 criteria, Mean(μ), RMS, Prob 1σ , Prob 2σ , and whether they are ‘‘Passed’’ or ‘‘Failed’’ are described, where the Prob $1(2)\sigma$ is the probability of entry within $\mu \pm 1(2)\sigma$	58
4.1	Rapidity (y) acceptance dependence of cumulants in $p+p$ collisions at $\sqrt{s} = 200$ GeV for $0.4 < p_T < 2.0$ GeV/ c and $ y < 0.1 - 0.5$. The red points are averaged values over multiplicity. The dotted lines represent the Skellam baselines. The statistical uncertainties are smaller than the size of the markers. The shaded gray bands show the systematic uncertainties. The light blue bands are PYTHIA 8 calculations. The blue dotted lines represent the Skellam of PYTHIA 8 calculations.	61
4.2	Rapidity (y) acceptance dependence of cumulant ratios in $p+p$ collisions at $\sqrt{s} = 200$ GeV for $0.4 < p_T < 2.0$ GeV/ c and $ y < 0.1 - 0.5$. The red points are averaged values over multiplicity. The dotted lines represent Skellam baselines. The statistical uncertainties are smaller than the size of the markers. The shaded gray bands show the systematic uncertainties. The light blue bands are PYTHIA 8 calculations. The blue dotted lines represent the Skellam of PYTHIA 8 calculations.	61

4.3	p_T acceptance dependence of cumulants at $\sqrt{s} = 200$ GeV $p+p$ collisions in $0.4 < p_T < 2.0$ GeV/ c and $ y < 0.1 - 0.5$. The red points are averaged values over multiplicity at $3 < m_{ch} < 30$. The dotted lines represent Skellam baselines. The bars indicate the statistical uncertainties. They are smaller than the size of markers. The shaded bands show the systematic uncertainties. The light blue bands are PYTHIA 8 calculations.	62
4.4	p_T acceptance dependence of cumulant ratios at $\sqrt{s} = 200$ GeV $p+p$ collisions in $0.4 < p_T < 2.0$ GeV/ c and $ y < 0.1 - 0.5$. The red points are averaged values over multiplicity at $3 < m_{ch} < 30$. The dotted lines represent Skellam baselines. The bars indicate the statistical uncertainties. They are smaller than the size of markers. The shaded bands show the systematic uncertainties.	63
4.5	Net-proton cumulants up to the sixth-order as a function of multiplicity in $p+p$ collisions at $\sqrt{s} = 200$ GeV for $0.4 < p_T < 2.0$ GeV/ c and $ y < 0.1 - 0.5$. Red points represent the average over the multiplicity region $3 < m_{ch} < 30$. The dotted lines represent Skellam baselines. The bars indicate the statistical uncertainties. The gray and green shaded bands show the systematic uncertainties for multiplicity bin and average values. The values at $17 < m_{ch} < 30$ are calculated in one centrality bin.	64
4.6	Multiplicity dependence of net-proton cumulant ratios in $p+p$ collisions in $p+p$ collisions at $\sqrt{s} = 200$ GeV for $0.4 < p_T < 2.0$ GeV/ c and $ y < 0.1 - 0.5$. Red points represent the average over the multiplicity region of $3 < m_{ch} < 30$. The dotted lines represent the Skellam baselines. The bars indicate the statistical uncertainties. The gray and green shaded bands show the systematic uncertainties for multiplicity bin and average values. The values at $14 < m_{ch} < 18$ and $17 < m_{ch} < 30$ are calculated as one multiplicity bin.	65
4.7	The ZDC coincidence rate dependence of the averaged number of TOF matched multiplicity m_{ch}^{TOF} over events.	66
4.8	Distributions of TOF matched multiplicity m_{ch}^{TOF} measured in different luminosity groups. Mean represents the average value of the TOF matched multiplicity distribution for each luminosity group.	66
4.9	ZDC coincidence rate dependence of efficiency corrected cumulants up to the sixth-order. The values are averaged over TOF matched multiplicity.	67
4.10	TOF matched multiplicity dependence of efficiency corrected cumulants up to the sixth-order. The red and blue bands and squares show bin-by-bin and average PYTHIA 8 calculations, respectively. The most right points represents $9 \leq m_{ch}^{\text{TOF}} < 20$	67
4.11	TOF matched multiplicity dependence of efficiency corrected cumulant ratios in different luminosity groups. The red and blue bands and squares show bin-by-bin and average PYTHIA 8 calculations, respectively. The most right points represents $9 \leq m_{ch}^{\text{TOF}} < 20$	68
5.1	Multiplicity distribution of charged particles calculated by PYTHIA 8 [19]. The black line shows the default multiplicity as used in data. The blue line shows the multiplicity with correlation from Λ decay.	69
5.2	The net-proton cumulant ratios with the refmult3A and the case of correlation from λ decay removed from centrality definition.	70
5.3	$ y $ distributions of (anti)protons by PYTHIA 8 in $p+p$ collisions at $\sqrt{s} = 200$ GeV with 100 million events in the CR-off configurations.	71
5.4	$ y $ distributions of (anti)baryons by PYTHIA 8 in $p+p$ collisions at $\sqrt{s} = 200$ GeV with 100 million events in the CR-off configurations.	71
5.5	Data and PYTHIA 8 calculation of y dependence of C_2 /Skellam in $p+p$ collisions at $\sqrt{s} = 200$ GeV for $0.4 < p_T < 2.0$ GeV/ c and $ y < 0.1 - 0.5$. The red points are observed average values over multiplicity. The solid magenta and blue lines are fitting of the data with linear and quadratic functions, respectively. The red and light blue bands show C_2 /Skellam and $1 - p$ calculated by PYTHIA 8. The blue and black solid lines are fitting for C_2 /Skellam and $1 - p$ calculated by PYTHIA 8, respectively. The statistical uncertainties are smaller than the size of the markers and bands. The shaded gray bands show the systematic uncertainties.	72
5.6	Multiplicity distributions for experimental data and demonstration of pileup filter. The yellow and green data show the distribution measured in luminosity groups #0 and #9, respectively. The red data is reproduced distribution from the yellow data.	73

5.7	Multiplicity distributions for experimental data and demonstration of pileup filter. The red and blue data correspond to pileup filtered distribution $\alpha P_{\#0}^{\text{pu}2}(N) + \beta P_{\#0}^{\text{pu}3}(N)$ and mean corrected distribution, respectively.	73
5.8	Multiplicity dependence of cumulants up to the sixth-order measured in the lowest and highest luminosity groups.	74
5.9	Multiplicity dependence of cumulants measured in lowest luminosity and calculated through the pileup filter.	74
5.10	Mean corrected multiplicity dependence of cumulants measured in the lowest luminosity and calculated through the pileup filter.	75
5.11	Mean corrected multiplicity dependence of cumulants up to the sixth-order measured in the lowest and highest luminosity groups.	75
5.12	Charged multiplicity dependence of the net-proton cumulant ratios, C_4/C_2 , C_5/C_1 and C_6/C_2 , from $\sqrt{s} = 200$ GeV $p+p$ and Au+Au collisions are shown as circles and triangles, respectively. The multiplicity ranges corresponding to the centrality classes in Au+Au collisions are also indicated in the plots. In $p+p$ collisions, the bars and bands are statistical and systematic uncertainties. The red, gold bands, and long-dashed lines indicate the calculations of Lattice QCD, PYTHIA 8, and Hadron Resonance Gas (HRG) models. In the PYTHIA 8, the option of color reconnection is off.	76
5.13	The relationship between TOF matched multiplicity and average values of mean corrected multiplicity.	76
A.1	Run division based on the vertex and phase information.	80
A.2	Histograms for event of the entries defined by the number of run with number of event weight for determination of mean and 3σ range in run-by-run QA.	81
A.3	Histograms for track of the entries which is the number of run with number of event weight for determination of mean and 3σ range in run-by-run QA.	82
A.4	Comparison of the C_n in the tightest (open red markers) and the loosest (solid blue markers) QA.	83
A.5	Comparison of the cumulant ratios in the tightest (open red markers) and the loosest (solid blue markers) QA.	83
A.6	Luminosity dependence of event and track quality observables— V_z , V_r , $V_z - V_z^{\text{VPD}}$, $ DCA $, DCA_{xy} , DCA_z , nHitsFit, nHitsDedx, nHitsR— from top left to right bottom panels, where the nHitsR represent the fraction of nHitsFit to number of possible hits on track.	84
B.1	Transverse momentum p_T dependence of efficiencies of the TPC, TOF with the EMC, and combination of them for protons at merged multiplicity over 2 to 30. Black dots show the TPC tracking efficiency. Green triangles show the TOF matching efficiency with the EMC hit requirement. Yellow squares show combined efficiencies of them. Red dotted lines represent $p_T = 0.4, 0.8, 2.0$ GeV/ c	86
B.2	Multiplicity dependence of p_T integrated efficiencies for the combination of the TPC and TOF with the EMC for protons and antiprotons. Black dots and red squares are shown region $0.4 < p_T < 0.8$ GeV/ c and $0.8 < p_T < 2.0$ GeV/ c , respectively. Solid (open) markers are protons (antiprotons). Blue solid (dotted) lines represent the linear function of fitting for protons (antiprotons).	86
B.3	Mean corrected multiplicity dependence of efficiencies measured in different luminosity groups for proton and antiproton at low and high p_T in $\sqrt{s} = 200$ GeV $p+p$ collisions. The solid lines are fitting by linear function.	87
B.4	Tofmatched dependence of efficiencies in different luminosity groups for proton and antiproton at low and high p_T in $\sqrt{s} = 200$ GeV $p+p$ collisions. The solid lines are fitting by linear function.	87
B.5	TOF matching efficiencies as a function of p_T in different luminosity groups for proton. The TOF matched multiplicity range $2 \leq m_{ch}^{\text{TOF}} < 20$ are shown.	88
B.6	Multiplicity dependence of efficiencies for $p+p$ and Au+Au collisions.	88

C.1	Multiplicity distributions of experimental data and PYTHIA 8. The blue data shows the PYTHIA 8 with color reconnection. The yellow data represents the measured data of luminosity groups #0 with mean correction.	90
D.1	Net-proton distributions for each Tofmatched in luminosity group #0.	91
D.2	Net-proton distributions for each Tofmatched in luminosity group #1.	92
D.3	Net-proton distributions for each Tofmatched in luminosity group #2.	92
D.4	Net-proton distributions for each Tofmatched in luminosity group #3.	93
D.5	Net-proton distributions for each Tofmatched in luminosity group #4.	93
D.6	Net-proton distributions for each Tofmatched in luminosity group #5.	94
D.7	Net-proton distributions for each Tofmatched in luminosity group #6.	94
D.8	Net-proton distributions for each Tofmatched in luminosity group #7.	95
D.9	Net-proton distributions for each Tofmatched in luminosity group #8.	95
D.10	Net-proton distributions for each Tofmatched in luminosity group #9.	96
D.11	Net-proton distributions for each Tofmatched in all luminosity group.	96
D.12	Multiplicity dependence of cumulants in different luminosity groups. The black square show average over luminosity. Multiplicity $27 \leq m_{ch} < 50$ are merged.	97
D.13	Shape corrected multiplicity dependence of cumulants in different luminosity groups. The black square show average over luminosity. Shape corrected multiplicity $25 \leq m_{ch} < 40$ are merged.	98
D.14	Mean corrected multiplicity dependence of p_T integrated efficiencies for proton at $0.4 < p_T < 0.8$ GeV/c in the lowest luminosity group as a function of multiplicity by combined the TPC and TOF with EMC in different cuts of DCA	99
D.15	Mean corrected multiplicity dependence of p_T integrated efficiencies for proton at $0.4 < p_T < 0.8$ GeV/c in the lowest luminosity group as a function of multiplicity by combined the TPC and TOF with EMC in different cuts of number of the TPC.	99
D.16	Tofmatched dependence of p_T integrated efficiencies for proton at $0.4 < p_T < 0.8$ GeV/c in the lowest luminosity group as a function of multiplicity by combined the TPC and TOF with EMC in different cuts of DCA	99
D.17	Tofmatched dependence of p_T integrated efficiencies for proton at $0.4 < p_T < 0.8$ GeV/c in the lowest luminosity group as a function of multiplicity by combined the TPC and TOF with EMC in different cuts of number of the TPC.	99
D.18	Multiplicity dependence of net-proton cumulants with different cut.	102
D.19	Multiplicity dependence of net-proton cumulants with different cut.	103
D.20	Multiplicity dependence of net-proton cumulant ratios with different cut.	103
D.21	Multiplicity dependence of net-proton cumulant ratios with different cut.	104
D.22	Average cumulants with different luminosity.	104
D.23	Average cumulants with different luminosity.	105
D.24	Average cumulant ratios with different luminosity.	105
D.25	Average cumulant ratios with different luminosity.	106
D.26	Δ/σ_{sc} distributions of cumulants up to sixth-order for different $n\sigma$ cuts. The black lines show mean values of the distributions. The red and blue dotted lines show $\mu \pm 1\sigma$ and $\mu \pm 2\sigma$, respectively.	106
D.27	Δ/σ_{sc} distributions of cumulants up to sixth-order for different $n\sigma$ cuts. The black lines show mean values of the distributions. The red and blue dotted lines show $\mu \pm 1\sigma$ and $\mu \pm 2\sigma$, respectively.	107
D.28	Δ/σ_{sc} distributions of cumulants up to sixth-order for different DCA cuts. The black lines show mean values of the distributions. The red and blue dotted lines show $\mu \pm 1\sigma$ and $\mu \pm 2\sigma$, respectively.	107
D.29	Δ/σ_{sc} distributions of cumulants up to sixth-order for different DCA cuts. The black lines show mean values of the distributions. The red and blue dotted lines show $\mu \pm 1\sigma$ and $\mu \pm 2\sigma$, respectively.	108
D.30	Δ/σ_{sc} distributions of cumulants up to sixth-order for different nHitsFit cuts. The black lines show mean values of the distributions. The red and blue dotted lines show $\mu \pm 1\sigma$ and $\mu \pm 2\sigma$, respectively.	108

D.31 Δ/σ_{sc} distributions of cumulants up to sixth-order for different nHitsFit cuts. The black lines show mean values of the distributions. The red and blue dotted lines show $\mu \pm 1\sigma$ and $\mu \pm 2\sigma$, respectively.	109
D.32 Δ/σ_{sc} distributions of cumulants up to sixth-order for different m^2 cuts. The black lines show mean values of the distributions. The red and blue dotted lines show $\mu \pm 1\sigma$ and $\mu \pm 2\sigma$, respectively.	109
D.33 Δ/σ_{sc} distributions of cumulants up to sixth-order for different efficiencies. The black lines show mean values of the distributions. The red and blue dotted lines show $\mu \pm 1\sigma$ and $\mu \pm 2\sigma$, respectively.	110
D.34 Δ/σ_{sc} distributions of cumulants up to sixth-order for different luminosity groups. The black lines show mean values of the distributions. The red and blue dotted lines show $\mu \pm 1\sigma$ and $\mu \pm 2\sigma$, respectively.	110
D.35 Δ/σ_{sc} distributions of cumulants up to sixth-order for different luminosity groups. The black lines show mean values of the distributions. The red and blue dotted lines show $\mu \pm 1\sigma$ and $\mu \pm 2\sigma$, respectively.	111
D.36 Δ/σ_{sc} distributions of cumulant ratios for different $n\sigma$ cuts. The black lines show mean values of the distributions. The red and blue dotted lines show $\mu \pm 1\sigma$ and $\mu \pm 2\sigma$, respectively.	111
D.37 Δ/σ_{sc} distributions of cumulant ratios for different $n\sigma$ cuts. The black lines show mean values of the distributions. The red and blue dotted lines show $\mu \pm 1\sigma$ and $\mu \pm 2\sigma$, respectively.	112
D.38 Δ/σ_{sc} distributions of cumulant ratios for different DCA cuts. The black lines show mean values of the distributions. The red and blue dotted lines show $\mu \pm 1\sigma$ and $\mu \pm 2\sigma$, respectively.	112
D.39 Δ/σ_{sc} distributions of cumulant ratios for different DCA cuts. The black lines show mean values of the distributions. The red and blue dotted lines show $\mu \pm 1\sigma$ and $\mu \pm 2\sigma$, respectively.	113
D.40 Δ/σ_{sc} distributions of cumulant ratios for different nHitsFit cuts. The black lines show mean values of the distributions. The red and blue dotted lines show $\mu \pm 1\sigma$ and $\mu \pm 2\sigma$, respectively.	113
D.41 Δ/σ_{sc} distributions of cumulant ratios for different nHitsFit cuts. The black lines show mean values of the distributions. The red and blue dotted lines show $\mu \pm 1\sigma$ and $\mu \pm 2\sigma$, respectively.	114
D.42 Δ/σ_{sc} distributions of cumulant ratios for different m^2 cuts. The black lines show mean values of the distributions. The red and blue dotted lines show $\mu \pm 1\sigma$ and $\mu \pm 2\sigma$, respectively.	114
D.43 Δ/σ_{sc} distributions of cumulant ratios for different efficiencies. The black lines show mean values of the distributions. The red and blue dotted lines show $\mu \pm 1\sigma$ and $\mu \pm 2\sigma$, respectively.	115
D.44 Δ/σ_{sc} distributions of cumulant ratios for different luminosity groups. The black lines show mean values of the distributions. The red and blue dotted lines show $\mu \pm 1\sigma$ and $\mu \pm 2\sigma$, respectively.	115
D.45 Δ/σ_{sc} distributions of cumulant ratios for different luminosity groups. The black lines show mean values of the distributions. The red and blue dotted lines show $\mu \pm 1\sigma$ and $\mu \pm 2\sigma$, respectively.	116
D.46 Systematic study for C_1 , C_2 , and C_3 as a function of TOF matched multiplicity.	116
D.47 Systematic study for C_4 , C_5 , and C_6 as a function of TOF matched multiplicity.	117
D.48 Systematic study for C_2/C_1 , C_3/C_2 , and C_4/C_2 as a function of TOF matched multiplicity.	117
D.49 Systematic study for C_5/C_2 , and C_6/C_2 as a function of TOF matched multiplicity.	118
D.50 TOF matched multiplicity dependence of efficiency corrected cumulants up to the sixth-order.	121
D.51 Average cumulants for TOF matched multiplicity and multiplicity. The values are not corrected by efficiency. The red and blue squares represent TOF matched multiplicity and mean corrected multiplicity, respectively. The range of averaging is $0 \leq m_{ch}^{TOF} < 20$ and $0 \leq m_{ch} < 30$, respectively.	121
D.52 Comparison of cumulants up to sixth-order with/without luminosity grouping.	122

D.53 Comparison of cumulant ratios up to sixth-order with/without luminosity grouping. . . .	122
D.54 ZDC coincidence rate dependence of average multiplicity measured in Au+Au collisions at $\sqrt{s_{NN}} = 200$ GeV. The blue circles are raw multiplicity and red circles are mean corrected multiplicity. The green circles are TOF matched multiplicity. The solid lines are linear fitting function.	123

List of Tables

2.1	Datasets of Beam Energy Scan program Phase 1 at the STAR experiment. Two collision systems, $p+p$ and Au+Au with energy, statistics, operation year, and μ_B are shown. . . .	30
2.2	Datasets for Au+Au collisions of BES-2 at the STAR experiment. The data of 3, 9.2, 11.5, and 13.7 GeV are obtained fixed target (FXT) mode.	31
3.1	Definition of multiplicity. The cuts for (a) charged particle selection and (b) proton and antiproton rejection are shown.	33
3.2	Definition of multiplicity class for $p+p$ collisions. Multiplicities $5 \leq m_{ch} < 15$ are studied bin-by-bin.	36
3.3	Definitions of event variables checked in QA.	37
3.4	Definitions of track variables checked in QA.	38
3.5	The information of the n variables, counted the number of bad runs, percentage of bad runs to the total, and available statistics.	38
3.6	Definition of four efficiency bins with two-particle and two p_T ranges.	39
3.7	Definition of the grouping of luminosity based on ZDC coincidence rate (ZDCCo.)	47
3.8	Mean values of the multiplicity distributions for each luminosity group.	47
3.9	Average $\langle \chi^2 \rangle$ for n th-order cumulants of uncorrected, mean corrected, and shape corrected multiplicity distributions, respectively.	51
3.10	Definition of multiplicity class for $p+p$ collisions. Multiplicities $3 \leq m_{ch} < 15$ are studied bin-by-bin.	53
3.11	Modification factor of efficiencies for each luminosity for proton and antiproton at low and high p_T region.	54
3.12	Variables and cut parameters for systematic study.	56
3.13	Acceptance for $ \eta $ and p_T	56
3.14	Four criteria of barlow check.	58
3.15	Contributions for systematic uncertainties (R_j) of cumulants and their ratios for six variables at $ y < 0.5$ and $0.4 < p_T < 2.0$ GeV/ c . The values of cumulants and their ratios are averaged over multiplicity.	59
3.16	Relative systematic uncertainties σ_{sys} (%) for cumulants and their ratios for five $ y $ acceptance and four p_T acceptance. The values of cumulants and their ratios are averaged over multiplicity.	59
4.1	Relative systematic uncertainty and R_j of average cumulants up to sixth-order.	68
5.1	Values of C_2 /Skellam, $\langle N_p \rangle$, $\langle N_B^{4\pi} \rangle$, p for each rapidity acceptance calculated by PYTHIA 8 in $p+p$ collisions at $\sqrt{s} = 200$ GeV with 100 million events in the CR-off configurations. . .	71
A.1	The definition of period for run-by-run QA of event variables (top) and track variables (bottom).	81
A.2	Definition of badrun in different condition and statistics.	82
B.1	TOF matching efficiencies in different luminosity groups for proton and anti-proton. . . .	86
D.1	Efficiency value and relative change of efficiency respect to the default cut for proton at low p_T , antiproton at low p_T , proton at high p_T , antiproton at high p_T for different cuts of DCA and number of the TPC hits. Efficiency values are averaged over multiplicity. . .	100

D.2	Averaged C_1 and modification factor(%) for protons at low p_T , antiprotons at low p_T , protons at high p_T , antiprotons at high p_T , net-proton at low p_T respect to the default cut.	101
D.3	Relative systematic uncertainty and R_j of cumulants up to sixth-order.	119
D.4	Relative systematic uncertainty and R_j of cumulant ratios.	120

Chapter 1

Introduction

1.1 Quantum chromodynamics (QCD)

One of the most fundamental goals in nuclear physics is to explore the constituents of matter and the mechanisms of their interactions. During the past century, it was found that nuclei are composed of nucleons, protons, and neutrons, and they are bounded by strong interactions over short distances. Furthermore, the hadrons represented by the nucleons have internal structures and components of partons, which was discovered in the deep inelastic scattering experiment in the 1960s. After that, the quark-parton model was constructed to describe the structure of hadrons. It shows that the gluons can propagate the interaction between quarks, which is strong interaction. Quarks and gluons are confined in hadrons by the strong interaction. quantum chromodynamics (QCD) is an effective quantum theory based on strong interaction. The quantum theory of electromagnetic interactions (QED) describes the mediation by exchanging photons, while QCD describes the mediation by the exchange of gluons between quarks. Instead the photon couples to the electric charge in QED, the gluon couples to a color charge of parton in QCD. The coupling strength in QCD is much larger than in QED. The fundamental properties of QCD theory are asymptotic freedom and confinement.

1.1.1 Asymptotic freedom

One of the properties of QCD theory is the asymptotic freedom at a short distance between quarks and gluons. The QCD potential (V_r) is composed of the Coulomb potential at short distance and confinement of quarks and gluons as:

$$V_r = -\frac{4}{3} \times \frac{\alpha_s}{r} + kr, \quad (1.1)$$

where the α_s is effective QCD coupling strength and r is the distance between two partons, and k is the string tension. The first term is corresponding to the case of short distance. In the strong interactions, the α_s is parameterized by the gauge coupling parameter g_s , which is written as:

$$\alpha_s(\mu) = \frac{g_s^2(\mu)}{4\pi}, \quad (1.2)$$

where μ is the momentum transfer scale.

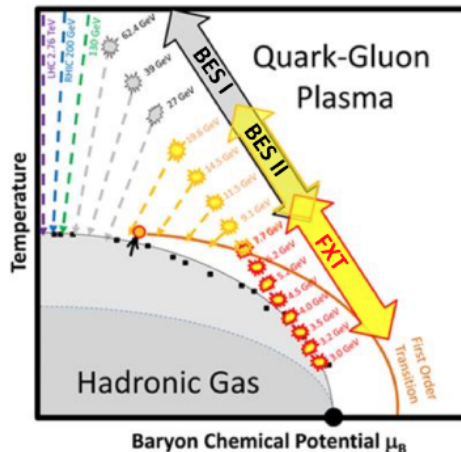
1.1.2 Confinement

As the experimental evidence of free quarks is not observed, it is believed that the quarks are confined within hadrons (quark confinement). At a long distance ($O(1\text{fm})$) between two quarks, the color force can work with $V_r = kr$ in Eq. 1.1. In this case, the quarks are connected to each other with constant tension. When the quarks are separated, a large amount of energy is stored on the connecting quarks. According to Heisenberg's uncertainty principle, quark pairs appear and disappear repeatedly in a vacuum. During the string connection of the quarks becomes long, they are separated into pieces, and then the pieces create many hadronic pairs (hadronization). The dynamics of strong interaction describe that gluons attract

each other (self-interactions). The separation of quarks requires an infinite amount of energy. As a result of gluon self-interactions, quarks and gluons are affected by color forces confined inside QCD potential. This quark confinement is numerically described by a first principle non-perturbative calculation called Lattice QCD.

1.2 QCD phase diagram

The phase of QCD matter is characterized by temperature (T) and baryon chemical potential (μ_B) which is depicted as the QCD phase diagram as shown in Fig. 1.1. There are the hadronic gas phase and Quark-Gluon Plasma (QGP) phase. In the $10\sim 20 \mu s$ after the Big Bang, the universe was filled with super-hot and dense matter. The QGP is a deconfined state in which quarks and gluons were free to move by weak coupling in that initial moment. In the heavy ion collisions, it is known that the QGP is hadronized into a hadron gas via chemical freeze-out [20]. Although the nature of the phase transition between these two phases is still experimentally uncertain, the transition at $\mu_B = 0$ MeV is shown to be a smooth crossover by Lattice QCD calculations [21, 22]. On the other hand, the phase transition is predicted to be the first-order transition at high μ_B region [23]. If those predictions at low and high μ_B are true, there should also exist the QCD critical point which is a connecting point between the smooth crossover and first-order transition. However, the locations of the critical point and phase transition lines are unclear.



The relationship between non-central and central moments for $n > 1$ can be written by:

$$\mu'_n = (-1)^n \mu^n + \sum_{m=1}^{n-1} \binom{n}{m} (-1)^{n-m} \mu^m \mu^{n-m} + \mu^n, \quad (1.5)$$

where the parentheses indicate binomial coefficients, $\binom{n}{m} = n!/\{n!(n-m)!\}$.

Cumulants are an alternative description of the moments to describe the shape of distributions. The n th-order cumulant C_n is expressed in terms of moments as:

$$C_1 = \langle N \rangle, \quad (1.6)$$

$$C_2 = \langle (\delta N)^2 \rangle = \mu_2, \quad (1.7)$$

$$C_3 = \langle (\delta N)^3 \rangle = \mu_3, \quad (1.8)$$

$$C_4 = \langle (\delta N)^4 \rangle - 3\langle (\delta N)^2 \rangle^2 = \mu_4 - 3\mu_2^3 \quad (1.9)$$

$$C_5 = \langle (\delta N)^5 \rangle - 10\langle (\delta N)^3 \rangle \langle (\delta N)^2 \rangle \quad (1.10)$$

$$C_6 = \langle (\delta N)^6 \rangle - 15\langle (\delta N)^4 \rangle \langle (\delta N)^2 \rangle - 10\langle (\delta N)^3 \rangle^2 + 30\langle (\delta N)^2 \rangle^3 \quad (1.11)$$

$$C_n = \mu_n - \sum_{m=2}^{n-2} \binom{n-1}{m-1} C_m \mu_{n-m}. \quad (1.12)$$

The relationships between cumulants and variance (σ^2), skewness (S), kurtosis (κ) are given by

$$\sigma^2 = \langle (\delta N)^2 \rangle = C_2, \quad (1.13)$$

$$S = \langle (\delta N)^3 \rangle / \sigma^3 = C_3 / (C_2)^{3/2}, \quad (1.14)$$

$$\kappa = \langle (\delta N)^4 \rangle / \sigma^4 = C_4 / (C_2)^2, \quad (1.15)$$

where S is the skewness and κ is the kurtosis that quantify the asymmetry and sharpness of the distributions, respectively. Figure 1.2 shows examples of skewness $S = 0, 0.5, 0.8$ and kurtosis $\kappa = 1, 0, -1$. It

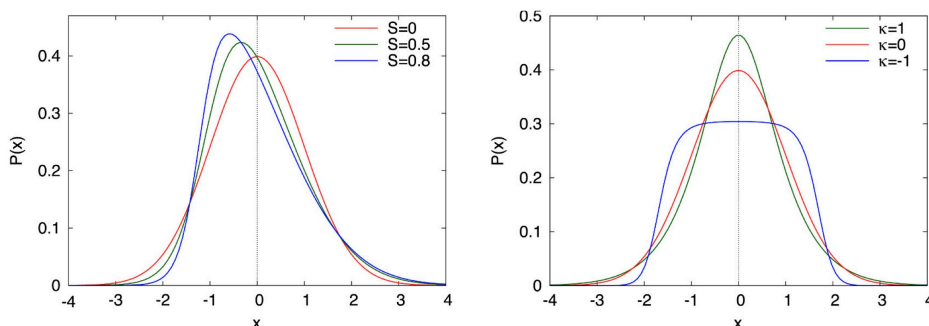


Figure 1.2: Illustration of the distributions for third- (left) and fourth-order (right) cumulants with examples of skewness $S = 0, 0.5, 0.8$ and kurtosis $\kappa = 1, 0, -1$, respectively [2].

is found that the larger the magnitude of the S is the more left-(or right-)skewed the distribution, and high kurtosis distributions have sharper peaks and wider tails.

In addition to the moments and cumulants, factorial moments and cumulants are used for efficiency correction which will be addressed in Sec. 3.2. The definition of the n th-order factorial moment f_n is given by

$$f_n = \langle N \times N(N-1) \times \dots \times N(N-n+1) \rangle = \left\langle \frac{N!}{(N-n)!} \right\rangle. \quad (1.16)$$

The relationships between factorial moment and factorial cumulant are the same as those between moments and cumulants:

$$\begin{aligned} \kappa_1 &= C_1, \quad \kappa_2 = -C_1 + C_2, \\ \kappa_3 &= 2C_1 - 3C_2 + C_3, \quad \kappa_4 = -6C_1 + 11C_2 - 6C_3 + C_4, \end{aligned} \quad (1.17)$$

where κ_1 is the mean for (anti-)protons. The factorial cumulants can be used to quantify differences from the Poisson distributions in terms of n -particle correlations [17].

1.3.2 Properties

For independent random variables X and Y each other, cumulants have additivity as:

$$C_n(X + Y) = C_n(X) + C_n(Y), \quad (1.18)$$

where the $C_n(X + Y)$ shows n th-order cumulants of probability distributions for their sum ($X + Y$). In the case of a distribution for difference between X and Y , cumulants are given by:

$$C_n(X - Y) = C_n(X) + (-1)^n C_n(Y), \quad (1.19)$$

where the odd-order cumulants are given by the difference of them, while even-order cumulants are sum of them.

Various order cumulants of conserved quantities are expected to be proportional to the correlation length (ξ) which diverges near the critical point [24] as:

$$C_2 = \langle (\delta N)^2 \rangle_c \approx \xi^2, \quad (1.20)$$

$$C_3 = \langle (\delta N)^3 \rangle_c \approx \xi^{4.5}, \quad (1.21)$$

$$C_4 = \langle (\delta N)^4 \rangle_c \approx \xi^7, \quad (1.22)$$

$$C_5 = \langle (\delta N)^5 \rangle_c \approx \xi^{9.5}, \quad (1.23)$$

$$C_6 = \langle (\delta N)^6 \rangle_c \approx \xi^{12}. \quad (1.24)$$

Since the cumulants have a trivial volume dependence, the ratio between different orders of cumulants is taken to cancel the volume terms. The products of cumulant ratios, $S\sigma$ and $\kappa\sigma^2$ can be directly compared to ratios of baryon number susceptibilities in theoretical calculation as:

$$S\sigma = \frac{C_3}{C_2} = \frac{\chi_B^{(3)}}{\chi_B^{(2)}}, \quad (1.25)$$

$$\kappa\sigma^2 = \frac{C_4}{C_2} = \frac{\chi_B^{(4)}}{\chi_B^{(2)}}, \quad (1.26)$$

where $\chi_B^{(n)}$ is n th-order thermodynamic susceptibilities for baryons calculated by Lattice QCD [3, 25–27]. Susceptibilities are defined by:

$$\chi_B^{(n)} = \frac{\partial^n (B/T^4)}{\partial (\mu_B/T)^2} = \frac{1}{VT^3} \times C_n^B, \quad (1.27)$$

where the μ_B and T are the finite baryon chemical potential and temperature, respectively, and V is the volume. The cumulants and their ratios are measured for the distribution of conserved quantities such as the number of net baryons, charge, and strangeness. Figure 1.3 shows the fourth-order susceptibilities calculated by Lattice calculations. It is found that a characteristic enhancement is observed near the critical point. The ratios between the fourth- and second-order fluctuations are shown in Fig. 1.4.

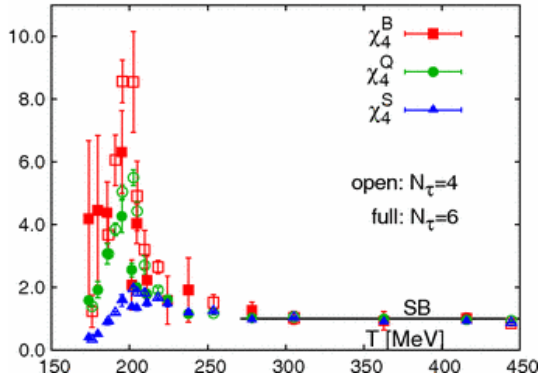


Figure 1.3: Temperature dependence of fourth-order fluctuations of number of baryon (χ_4^B), electric charge (χ_4^Q) and strangeness (χ_4^S) [3]. The quantities are respectively normalized by the number of free quarks.

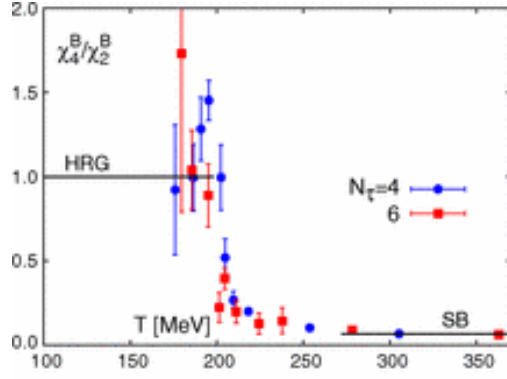


Figure 1.4: Temperature dependence of the ratio between the fourth- and second-order fluctuation of baryon number. The solid line represents the Hadron Resonance Gas (HRG) model over 100 to 200 MeV.

For the experimental accessibility, it is ensured that the net-proton cumulants can be a proxy of fluctuation of net-baryon by the theoretical calculations [28].

1.3.3 Statistical baseline

If the protons and antiprotons are distributed as the independent Poisson distributions, net-particles follow the Skellam distribution:

$$f(k; m_1, m_2) = e^{m_1+m_2} \left(\frac{m_1}{m_2}\right)^{k/2} I_{|k|}(2\sqrt{m_1 m_2}), \quad (1.28)$$

where the m_1 and m_2 are the mean of the Poisson distributions for particles 1 and 2, respectively, I_k is the Bessel function of the first kind. Various moments, M , σ , S , and κ of Skellam distribution are expressed as:

$$M = m_1 - m_2, \quad \sigma = \sqrt{m_1 + m_2}, \quad S = \frac{m_1 - m_2}{(m_1 + m_2)^{2/3}}, \quad \kappa = \frac{1}{m_1 + m_2}, \quad (1.29)$$

and their products, $S\sigma$ and $\kappa\sigma^2$ are written as:

$$S\sigma = \frac{m_1 - m_2}{m_1 + m_2}, \quad \kappa\sigma^2 = 1. \quad (1.30)$$

With the above definition, statistical baselines for odd- and even-order of measured net-proton cumulants, C_{odd} and C_{even} can be written as:

$$C_{odd} = C_1^p - C_1^{\bar{p}} \quad C_{even} = C_1^p + C_1^{\bar{p}}, \quad (1.31)$$

where the $C_1^{p(\bar{p})}$ are mean value of Poisson distributions for (anti-)proton. This leads to the statistical baseline of cumulant ratios as:

$$\frac{C_{even}}{C_{odd}} = \frac{C_1^p + C_1^{\bar{p}}}{C_1^p - C_1^{\bar{p}}}, \quad \frac{C_{odd}}{C_{even}} = \frac{C_1^p - C_1^{\bar{p}}}{C_1^p + C_1^{\bar{p}}}. \quad (1.32)$$

If there are only statistical fluctuations, C_4/C_2 , C_5/C_1 , and C_6/C_2 become unity as a statistical baseline.

Cumulants are measured from the distribution of conserved quantities, while several corrections are necessary to suppress various experimental artifacts.

1.4 Experimental results on the QCD phase structure

1.4.1 QCD critical point

It was suggested that higher-order fluctuations of conserved quantities are sensitive to the QCD critical point [5, 24, 29]. The fourth-order fluctuations ($\kappa\sigma^2$) of net-proton distributions were then measured at the STAR experiment in the RHIC BES program, and it was found that the results show non-monotonic beam energy dependence [4, 17] as shown in Fig. 1.5.

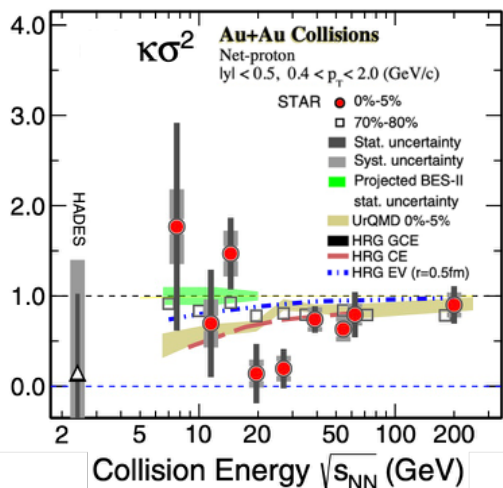


Figure 1.5: Collision energy dependence of the $\kappa\sigma^2$ for net-proton distributions in Au+Au collisions at $\sqrt{s_{NN}} = 7.7 - 200$ GeV measured by STAR and $\sqrt{s_{NN}} = 2.4$ GeV measured by HADES experiment [4]. The results are shown for central (0 – 5%) collisions with filled circles and peripheral (70 – 80%) collisions with open squares within $0.4 < p_T < 2.0$ GeV/c and $|y| < 0.5$. The statistical and systematic uncertainties are shown in narrow and wide bars, respectively.

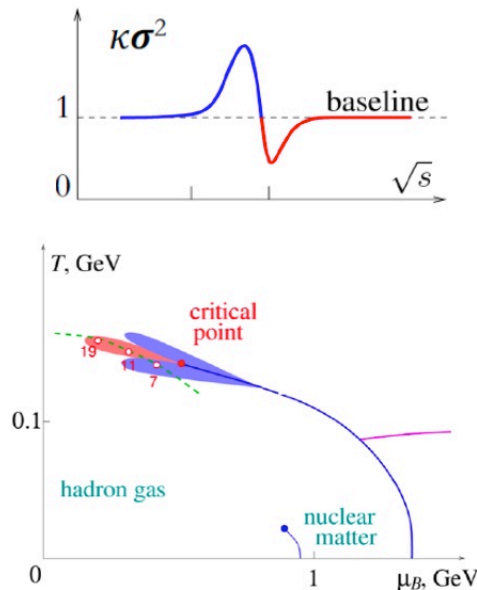


Figure 1.6: Upper panel: A sketch of the κ_4 behavior near the critical point predicted by Lattice QCD. Lower panel: A sketch of the QCD phase diagram with the curve of freezeout and a possible mapping for the Ising coordinates t and H [5].

The observed non-monotonic beam energy dependence for the most central Au+Au collisions is qualitatively similar to the theoretical prediction incorporating the critical point as shown in Fig. 1.6. The model expects that the fourth-order moment of the baryon number fluctuations possibly turns negative values near the QCD critical point from the crossover side. Thus, the results could indicate a possible signature of the critical point. In addition, at even lower energy 2.4 GeV, the results from the High Acceptance Di-Electron Spectrometer (HADES) experiment are shown. If the connection of enhancement at 20-7.7 GeV and the HADES result follows the upper panel of Fig. 1.6, a possibility of the peak at their gap energy, 2.4-7.7 GeV.

1.4.2 Crossover search

Theoretically, next-to-leading order (NLO) calculation of fifth- and sixth-order cumulants predicts negative signs at low μ_B/T [6]. Lattice QCD predicts that the cumulant ratios, $R_{51}^B(T, \mu_B)$ and $R_{62}^B(T, \mu_B)$, turn to negative as shown in Fig. 1.7. The ratio of baryon number fluctuation χ_6^B/χ_2^B is expected to decrease toward negative near the phase transition temperature [30]. Figure 1.8 shows the Polyakov loop extended Quark Meson (PQM) model calculation of sixth-order fluctuation of net-baryon number distributions. The results show negative enhancement near the $T/T_{pc} \sim 1$ in $\mu_q/T = 0, 0.14$.

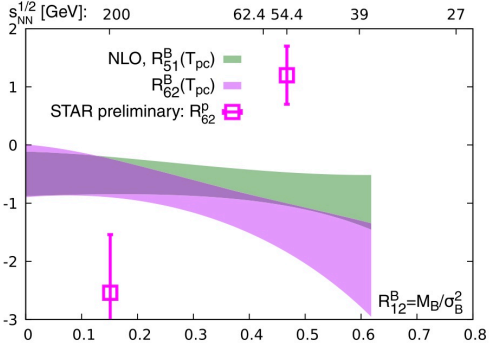


Figure 1.7: μ_B/T dependence of the cumulant ratios $R_{51}^B(T, \mu_B)$ and $R_{62}^B(T, \mu_B)$ from leading order (LO) and NLO of Taylor expansions of cumulants on Lattice with $N_\tau = 8$ [6]. Magenta and green bands show the sixth- and fifth-order fluctuations, respectively.

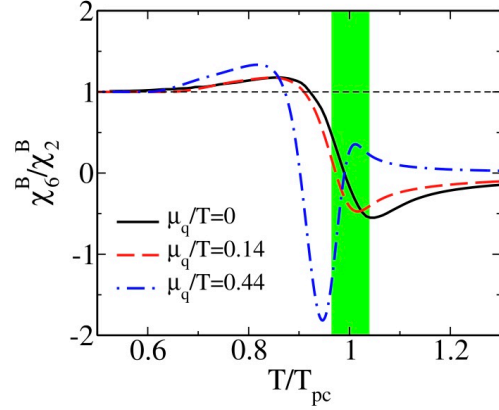


Figure 1.8: Temperature dependence of the ratios χ_6^B/χ_2^B for various μ_q/T corresponding to values at chemical freeze-out at RHIC [7]. The shaded area shows the chiral crossover region.

experimentally, the sixth-order fluctuations have been measured at the STAR experiment as shown in Fig. 1.9. The results show negative values in central Au+Au collisions at $\sqrt{s_{NN}} = 200$ GeV [8]. The negative sign is qualitatively consistent with the theoretical expectations as shown in Fig. 1.7 and 1.8. Therefore, it could be a signature of smooth crossover at RHIC top energy [30,31].

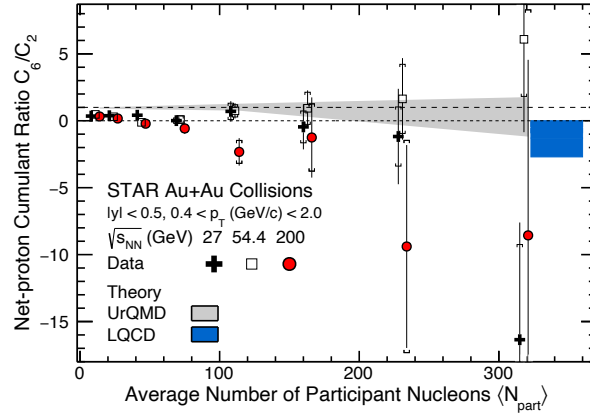


Figure 1.9: Number of participants (N_{part}) dependence of cumulant ratio C_6/C_2 measured in Au+Au collisions. The red marker shows the results measured in collision energy 200 GeV [8].

1.5 Indication of QGP droplet in small systems

Evidence for the formation of QGP is observed in the central of the Au+Au collisions. On the other hand, the QGP formation in the small systems is still unclear. Several studies have been reported in $p+p$ collisions at LHC in terms of the strangeness enhancement and flow measurements etc [32]. One of the discussed probes for QGP formation is the enhancement of strangeness in A+A collisions. In the initial state of high energy collisions, the strange quarks are sufficiently light to be created during the process of the collisions. Figure 1.10 shows the ratios of the yields for K_S^0 , Λ , Ξ to the pion yields as a function of average charged particle density ($\langle dN_{ch}/d\eta \rangle$). The results are compared to $p+Pb$ and Pb+Pb collisions. In $p+p$ collisions, the results show the enhancement of strange to non-strange hadron production with

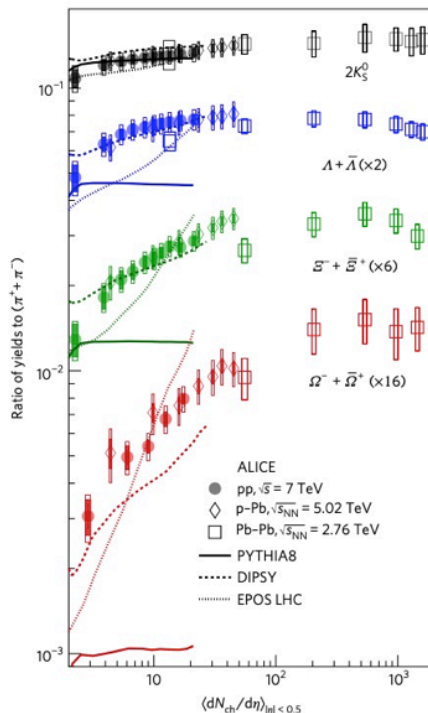


Figure 1.10: p_T -integrated yield ratios to pions ($\pi^+ + \pi^-$) as a function of $\langle dN_{ch}/d\eta \rangle$ measured in $|y| < 0.5$ [9]. The error bars show the statistical uncertainty. The empty and dark-shaded boxes are the systematic uncertainty and the contribution uncorrelated across multiplicity bins, respectively. The values are compared to calculations from MC models, and results are obtained in $p+Pb$ and Pb+Pb collisions at the LHC. For Pb+Pb results the ratio $2\Lambda/((\pi^+ + \pi^-))$ is shown.

increasing multiplicity. Both the values of the ratios and their multiplicity dependence resemble those of $p+Pb$ collisions at lower energy. At high multiplicity, the ratios reach values similar to those of Pb+Pb collisions. These results of the yields indicate that from $p+p$ to central Pb+Pb collisions, various systems are connected in different underlying physics.

On the other hand, results of the flow (v_2) measurements have been reported at LHC in $\sqrt{s} = 13$ TeV $p+p$ collisions [33]. The v_n characterize the modulation of the azimuthal angle distribution for a single particle. In A+A collisions, the $n = 2$ harmonic has been understood to result from an elliptic anisotropy in the initial state with a non-zero impact parameter. In the magnetic field, elliptic anisotropy of the viscous pressure tensor is characterized as a feature of QGP. The v_2 is defined as the second-order Fourier coefficients of the azimuthal angle distribution written as $dN/d\phi = \langle dN/d\phi \rangle (1 + \sum 2v_2 \cos(2(\phi - \Psi)))$, where the bracket is average over azimuthal angles, and ϕ and Ψ are the angle of particles and event plane, respectively. The values of the v_2 are obtained by two-particle correlation using charged particles detected with pseudorapidity separation $|\Delta\eta| > 2$. In $p+p$ collisions, the results from the CMS and ATLAS experiments are shown in the right and left-hand sides of Fig. 1.11, respectively. The ATLAS experiment adopted a template fitting procedure to remove back-to-back non-flow contribution to the correlation function. In the CMS experiment, the v_2 is measured as a function of number of pixel tracks ($N_{\text{trk}}^{\text{offline}}$) at $|\eta| < 2.4$ and $0.3 < p_T < 3.0$ GeV/c. It is found that the v_2 measured by CMS shows

the increasing trend with particle multiplicity. The multiplicity dependence show agreement with the hydrodynamic model. However, in the ATLAS results, the values do not show significant change over the multiplicity. These different results of v_2 indicate that the signal of QGP is very uncertain in $p+p$

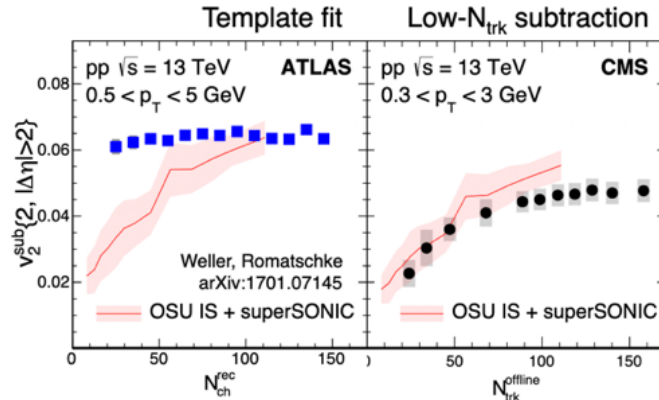


Figure 1.11: Elliptic flow (v_2) as a function of N_{ch}^{rec} in the 13 TeV $p+p$ collisions measured by ATLAS (left) and CMS (right) experiments [10]. They were measured with different methods for $0.5 < p_T < 5$ GeV/ c and $0.3 < p_T < 3$ GeV/ c , respectively. The red bands show the calculation of superSONIC. The error bars are statistical uncertainties.

collisions by these measurements.

Therefore, in this thesis, we focus on the fluctuation of conserved quantities to explore the phase transition signal. This can be achieved by measurement of fifth- and sixth-order fluctuations at high multiplicity events in $p+p$ collisions.

1.6 Motivation

The fluctuation measurements in $p+p$ collisions are expected to be a complementary reference study of physics baseline for Au+Au collisions as shown in Fig. 1.12. The collision energy dependence of $S\sigma$ and $\kappa\sigma^2$ are measured in $p+p$ and Au+Au collisions in 2014. However, the uncertainties are large to extract any physics message due to the insufficient statistics.

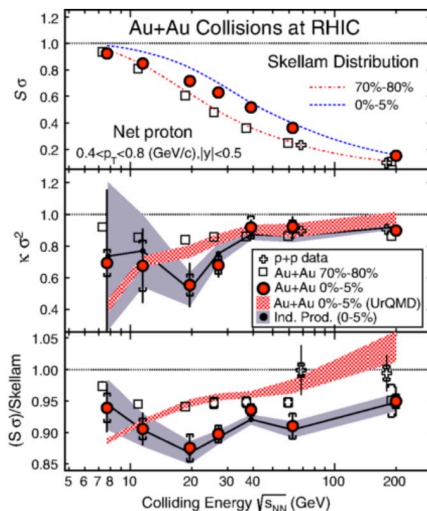


Figure 1.12: Collision energy dependence of the net-proton $S\sigma$, $\kappa\sigma^2$, and $(S\sigma)/\text{Skellam}$ for $p+p$ and Au+Au collisions [11]. Open squares, filled circles, and crosses are for the efficiency corrected results of 70 – 80%, and 0 – 5% Au+Au collisions, and $p+p$ collisions respectively. Skellam baselines for corresponding collision centralities are shown in the top panel. Shaded hatched bands show UrQMD model calculations. The solid bands in the middle and lower panels are the expectations assumed independent protons productions. The bandwidth shows the statistical uncertainties. The HRG results for middle and lower panels are unity. The bars and caps show statistical and systematic uncertainties, respectively. The values of $p+p$ and Au+Au 70 – 80% are slightly displaced horizontally.

In this analysis, precise measurements are performed with 70 times larger statistics than the previous study published in 2014. To study the effects of baryon number conservation on cumulants, the rapidity and transverse momentum acceptance dependence are measured. Furthermore, the large statistics make the first measurements of the multiplicity dependence of cumulants possible in $p+p$ collisions. This provides a precise baseline to the fluctuations measured in Au+Au collisions. Simultaneously, connections between $p+p$ and Au+Au central collisions are explored at the high multiplicity events, which provides the information on possible phase transition in $p+p$ collisions based on positive/negative signs of fifth- and sixth-order fluctuation.

The main goal of this thesis is to determine the precise physics baselines of the higher-order fluctuations of net-proton number distributions measured in Au+Au collisions. This can also explore the question—whether QGP is generated at high multiplicity events— by fluctuation measurements in $p+p$ collisions.

This thesis is organized as follows. In Chapter 2, experimental circumstances are described. In Chapter 3, analysis methods are explained to study the effect. In Chapter 4, the results are discussed. In Chapter 5, the summary and outlook are shown.

Chapter 2

Experiment

2.1 Relativistic Heavy Ion Collider (RHIC)

The Relativistic Heavy Ion Collider (RHIC) at Brookhaven National Laboratory (BNL) is the world's first collider to create hot dense matter by accelerating heavy ions. The RHIC consists of double superconducting rings, called “Yellow” and “Blue” rings, in 3.8 km circumference as shown in Fig. 2.1. There are six interaction points in the RHIC, and four of them are equipped with detectors, BRAHMS, PHENIX, PHOBOS, and STAR. The collisions of heavy ions are achieved in the center of mass collision energy $3.3 \leq \sqrt{s_{NN}} \leq 200$ GeV. The 1740 superconducting magnets can deflect and focus the stored large amount of particles with high luminosity, $20 \times 10^{26} \text{ cm}^{-2} \text{ s}^{-1}$. RHIC acceleration system is mainly composed of three accelerators, Tandem Van de Graaff, booster Synchrotron, and Alternating Gradient Synchrotron (AGS). Accelerated ions at LINAC with 200 MeV are injected into AGS to polarize protons to 25 GeV, then only one of the 12 rf buckets is injected into the RHIC. Tandem Van de Graaff can accelerate gold with 1 MeV per nucleon which strips the electric charge of 31 of 79 electrons from the gold atom.

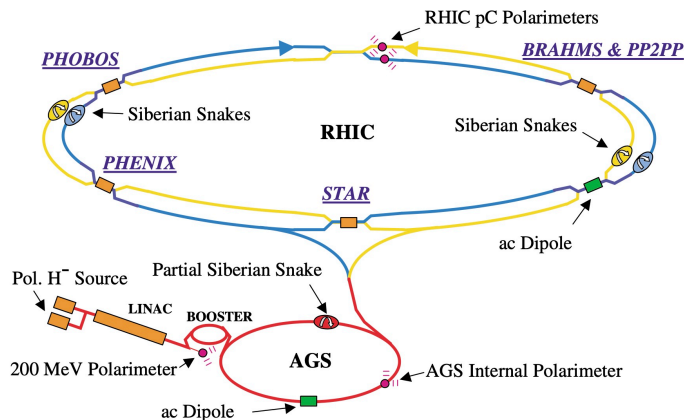


Figure 2.1: The RHIC complex layout [12].

2.2 The STAR Experiment

The Solenoidal Tracker at RHIC (STAR) experiment aims to explore the properties of QGP as one of its scientific missions. The STAR detector is located at 8 o'clock in the RHIC ring. The structure specializes in the simultaneous measurements of hadron production with a large angle and uniform acceptance, which is suitable for the precise fluctuation measurements. The overview of the STAR detector is shown in Fig. 2.2. The main tracker called Time Projection Chamber (TPC) is centered on the magnet with several sub-systems as shown in Fig. 2.3. The outermost part of the devices is the cylindrical solenoid magnet with 7.32 (m) for the diameter of the outer radius, which can produce a near-uniform field along

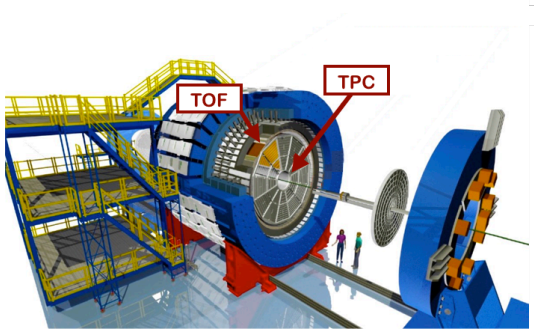


Figure 2.2: The sketch of the STAR detector.

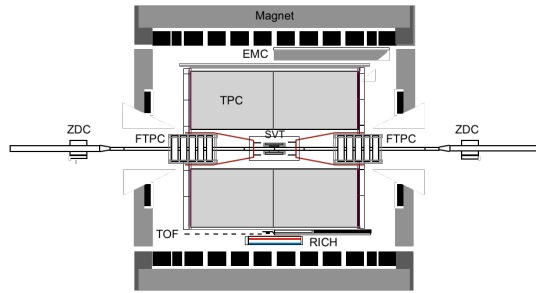


Figure 2.3: Cutaway view of the STAR detector.

the beamline over $0.25 < B_z < 0.5$ (T). Charged tracks bent by the magnet are captured by surrounding detectors over full azimuthal angle ($\Delta\phi = 2\pi$) and large pseudo-rapidity coverage ($|\eta| < 2$). The TPC is also provided particle identification, momentum, and vertex position. To obtain collisions vertex, Vertex Position Detectors (VPD) are installed near the beam pipe. The main operating calorimeters are Electro-Magnetic Calorimeter (EMC) systems located outside the TPC. For the monitoring of collider luminosity, Zero Degree Calorimeters (ZDC) are used. In this analysis, the TPC is used for proton identification and measurement of vertex positions. TOF is used to extract protons in the high momentum region where the protons cannot be identified by the TPC. VPD is used for removing pileup events and triggering collision events. EMC hits are included in tracking to remove pileup tracks making use of its fast speed for the estimation of the efficiencies. ZDC is used to measure luminosity.

2.2.1 The Time Projection Chamber (TPC)

The Time Projection Chamber (TPC) is the main tracking device to provide tracking information, particle identification, momentum, and vertex position. The TPC is designed as shown in Fig. 2.4. The 4.2 m cylindrical chamber is designed to be concentric with beam pipe over 0.5(2.0) m in the inner(outer) radius. TPC covers the full azimuthal angle $0 < \phi < 2\pi$ and pseudo-rapidity acceptance $|\eta| < 2$. The charged particles with transverse momentum $p_T > 0.04$ GeV/c and $|\eta| < 1$ can reach the TPC active volume with radius > 0.5 m due to the relationship between limits of magnetic field and spiral radius of particles. Electrons released from tracks drift in the P10 gas (90% Ar and 10% CH₄) to the endcap along the electric field 135 V/cm with velocity 5.45 cm/ μ s. The signal of electrons passing through the P10 gas is received and reconstructed by the readout system. The readout system is based on the multi-wire proportional chamber which is composed of a pad plane and several wire planes. One of the readout layers, anode wire, is set perpendicular direction to the radial tracks with the highest p_T and the width is 20 μ m. At anode wires, the image charges are generated by an avalanche of drift electrons with 1000 ~ 3000 amplification of the signal. By reading out the induced charge from the avalanche using a total of 136,000 adjacent pads, the position of the original track can be precisely reconstructed to small fractions of pad width. The position resolutions are determined by the diffusion of the electrons and their number. At the gating grid, the entry of drifting electrons into the pad plane is controlled by switching the voltage on every other wire with 110 V "open" and ± 75 V "close". The positive ions generated from the wire chamber are also blocked to enter the drift volume by the gating grid with opening time 2.1 μ s. TPC tracking efficiency is estimated by the tracking performance of embedded particles with GEANT simulation inside the real events. The momentum resolution, $\delta p/p$, is 1-2 %, and resolution on tracks for total path length is less than 0.5 cm. The tracking systems and capability provide momentum measurement, particle identification, and vertex reconstruction.

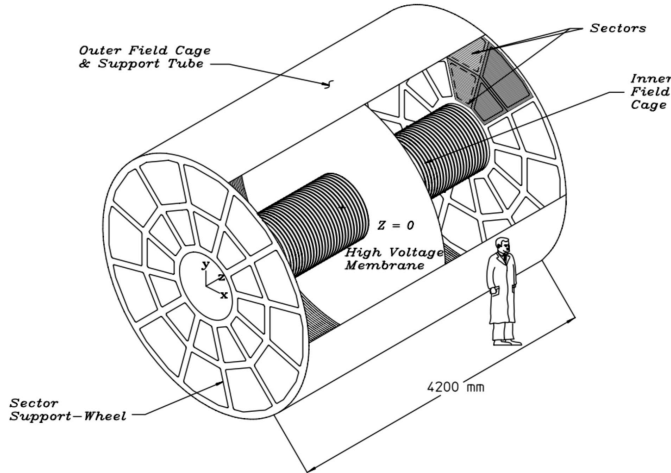


Figure 2.4: The TPC perspective view [13].

To reconstruct the position, the coordinates x , y , and z are defined by the measured charges where the x is along the pad row direction, y is the perpendicular direction to the x , and z is along the beamline direction, respectively. For simplicity, at a Gaussian distribution on the pads, the x is determined by:

$$x = \frac{\sigma^2}{2w} \ln(h_3/h_1), \quad (2.1)$$

where h_1 , h_2 , and h_3 are the amplitudes measured by three adjacent pads with the pad h_2 centered at $y = 0$, and σ is the width of the signal with pad width w . The relationship between σ and w is written by $\sigma^2 = x^2 / \ln(h_2^2/h_1h_3)$. The z is determined by the drift velocity and drift time of the secondary electrons from the original point to the anodes at the endcap. To calculate the drift time of the cluster of secondary electrons, the arrival time of electrons in buckets of 100 ns is measured by weighting the average by charge for each bucket. At the length of the signal arriving at the pad, L , the ionization electrons are diffused along the beam direction with distance $L/\tan\theta$ where the θ is the angle between the drift direction and particle momentum. It is necessary for the conversion of time into position to obtain the drift velocity of electrons with high precision of 0.1% and to control the timing offset between the first bucket and the collision. The drift velocity is varied by gas composition and atmospheric pressure, which are minimized by tuning the cathode voltage and the independent measurements of drift velocity with artificial tracks by lasers beam. With the drift velocity, the timing offset caused by the trigger delay, time spent of electron drift, and shaping signal is adjusted. It can be performed by matching the interaction vertex reconstructed from the half side of the TPC with the vertex found using the data from the other side. The drift time is related to the interaction rate of collision pileups depending on the luminosity and vertex resolution. During the drift with 40 μsec , events at high luminosity above $2 \times 10^{26} \text{ cm}^{-2}\text{s}^{-1}$ can cause overlap for Au + Au collisions, which can be backgrounds at the distance closer to vertex position than the TPC capability. This pileup study will be discussed later part of the next chapter. The vertex resolution depends on the number of tracks, which is achieved to be approximately 350 μm with more than 1000 tracks.

The particle identifications are performed in $0.15 < p_T < 30 \text{ GeV}/c$ via ionization energy loss (dE/dx) in the gas. The resolution of dE/dx is limited by the finite length of tracks and ionization fluctuations, which is optimized to obtain more ionization electrons for statistical improvement. To separate protons and pions up to 1.2 GeV/c , a relative dE/dx resolution of 7% is necessary. At high momentum region, it is hard to separate particle species with above 0.7 GeV/c velocities due to the reduction of mass dependence of the dE/dx , which can be resolved by using the TOF discussed in the next subsection. Figure 2.5 shows the momentum dependence of the measured dE/dx in the magnetic field 0.25 T. The plotted data includes primary and secondary particles. The bands of protons, deuterons, and muons are generated from secondary interactions in the beam pipe and decay of pions and kaons. The mean dE/dx is described by Bethe-Bloch and the deviation from the values defined as $n\sigma$ is used for particle identification.

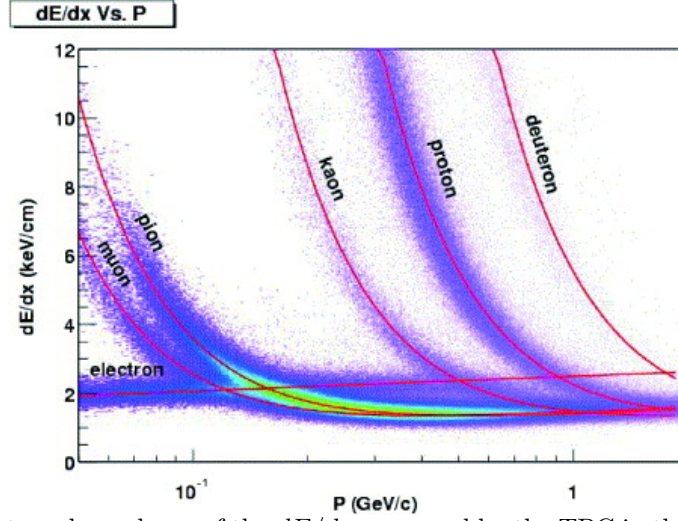


Figure 2.5: Momentum dependence of the dE/dx measured by the TPC in the magnetic field 0.25 T [13].

2.2.2 The Time of Flight (TOF)

The Time of Flight (TOF) detector is used to provide the particle identification for the spectra of charged hadrons. The TOF measures the passing time of charged particles from the primary vertex of collisions. At a given flight time t and path length L of charged tracks, the velocity β and mass m are calculated by:

$$\beta = \frac{v}{c} = \frac{L}{ct} \quad (2.2)$$

$$m^2 = p \times \left(\frac{1 - \beta^2}{\beta^2} \right) = p \times \frac{(ct)^2 - L^2}{L^2}. \quad (2.3)$$

The resolution of mass is described as:

$$\frac{\Delta M}{M} = \frac{\Delta p}{p} + \gamma^2 \times \left(\frac{\Delta t}{t} + \frac{\Delta L}{L} \right). \quad (2.4)$$

The TOF is located at the cylindrical radius of the TPC with the full azimuthal angle 2π and rapidity acceptance $|\eta| < 2$. Its total time interval resolution (Δt) of 100 ps provides the capabilities of particle identification shown in Fig. 2.6. The particle momentum dependence of mass for deuterons, protons, kaons, and pions are measured as labeled with the path length resolution $\delta L/L = 0.2\%$, and momentum resolution $\delta p/p = 1.3\%$. The solid and dashed lines indicate the tracks near $\eta = 0$ and $\eta = 1$, respectively. At $\eta \sim 1$, the path length is approximately 50% longer compared to $\eta \sim 0$. The pair of upper and lower lines are shown for momentum dependence of $M + \Delta M$ and $M - \Delta M$, respectively, where ΔM is obtained by Eq. 2.4. In this figure, the maximum momentum at which particles can be identified in “2 σ ” is shown by the momentum at which the upper line of the particle intersects the lower line of other particles. It is found that for tracks near $\eta \sim 0(1)$, the pion/kaons/protons are identified up to $\sim 1.7(1.9)$ GeV/ c and direct protons/(pions + kaons) are identified up to $\sim 2.6(3.1)$ GeV/ c . In the proton identification, the figure also provides that the pions are the first particles to lead to backgrounds with increasing momentum.

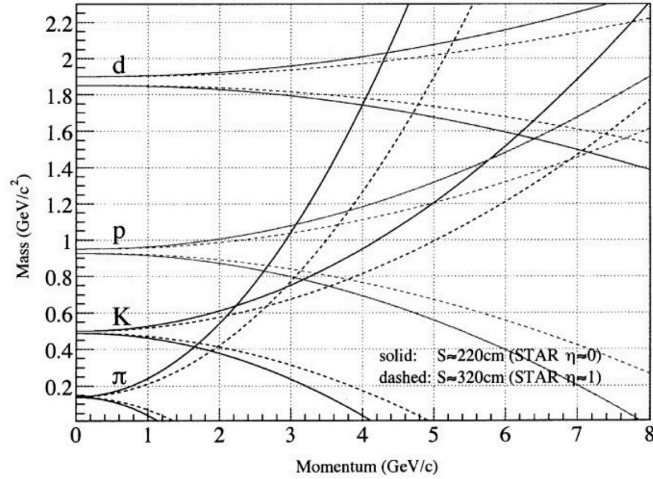


Figure 2.6: The particle momentum dependence of mass for deuterons, protons, kaons, and pions are measured as labeled with the time resolution $\Delta t = 100$ ps, path length resolution $\delta L/L = 0.2\%$, and momentum resolution $\delta p/p = 1.3\%$ [14]. The solid and dashed lines indicate the tracks near $\eta \sim 0$ and $\eta \sim 1$, respectively. The pair of upper and lower lines are shown for momentum dependence of $M + \Delta M$ and $M - \Delta M$, respectively.

The TOF system consists of two subsystems, Pseudo Vertex Position Detectors (pVPD) and Time of Flight Patch (TOFp), for “start” and “stop” detector, respectively [14]. Figure 2.7 shows the positions of the TOFp and pVPD with respect to the TPC and the RHIC beam pipe. These sub-detectors are based on the technology of scintillator and phototube. The start timing is given by the two VPDs positioned along the beam pipe at each 5.7 m away from the center of the TPC. The effective timing resolution is 140 ps in 200 GeV $p+p$ collisions. More details of the VPD are addressed in Sec. 2.2.3. The TOFp is located outside the barrel of the TPC and inside the magnet. It has 120 aluminum boxes (“trays”) of 1.27 mm-thick and each tray consists of 32 Multi-gap Resistive Plate Chamber (MRPC) modules with 6 readout pads along the azimuthal direction on each module. MRPC is a stack of resistive plates with float glass of 0.54 mm and five gas gaps of 220 μm . The outer plates of 20 cm length are composed of graphite electrodes with ~ 14 kV voltage gap. inner plates for keeping the voltage in avalanches at a strong electric field. The time resolution to detect particles is less than 80 ps. Detecting efficiency for the charged particle is above 95% at $p_T > 0.5$ GeV/c in a gas of 95% freon and 5% isobutane on the voltage of 154 kV.

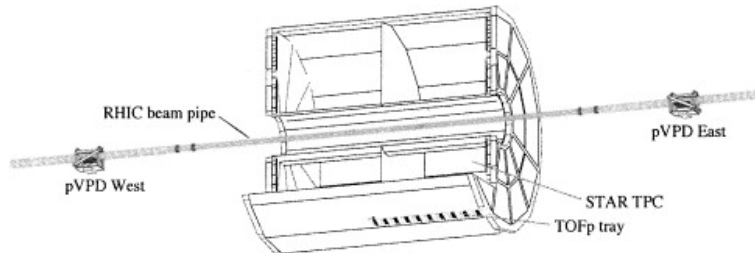


Figure 2.7: A cutaway drawing of locations of the TOFp and pVPD with the TPC and the beam pipe [14].

2.2.3 Other sub-systems

Vertex Position Detector (VPD)

As described in Sec. 2.2.2, the VPD is used to provide start timing to the TOF detector. The VPD is composed of two identical detectors installed close to the beam pipe at a distance of $|Z| = 5.6$ m and outside the STAR magnet. These equally spaced detectors measure the prompt pulses of photons produced from the collision vertex. Measuring their arrival time provides the location of the vertex along the beam pipe. The event start time is determined by the average of two arrival times of the pulses. To

measure the time interval, stop times are provided by the TOFp detector, and these signals from the VPDs and TOFp are digitized and interfaced with the STAR data stream. Figure 2.8 shows one of the two VPD assemblies. The VPD consists of three elements—an aluminum base plate, two faceplates, and aluminum rails, on each side. They are located at a distance of ~ 5 m from the intersection range. The design of the VPD read-out system is based on the technology of plastic scintillator by photomultiplier tubes. The electrons converted from the photons at the scintillator layer provide large PMT signals and start timing.

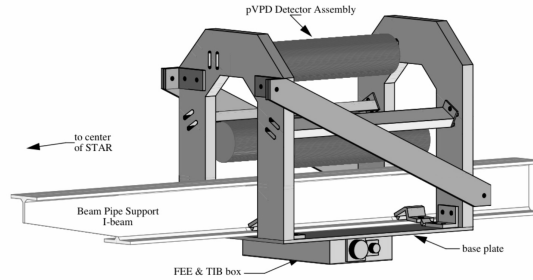


Figure 2.8: One of the two identical VPD assemblies [14]. The "FEE & TIB" is the Front End Electronics and the Threshold Interface Board.

Electro-Magnetic Calorimeter (EMC)

The EMC is used to determine the trigger on the photons, electrons, and decaying hadrons. EMC systems are composed of Barrel Electro-Magnetic Calorimeter (BEMC) and Endcap Electro-Magnetic Calorimeter (EEMC). They are located inside the aluminum coil of the solenoid. The coverage of BEMC and EEMC is $|\eta| < 1$ and $1 < \eta < 2$, respectively, and full azimuthal acceptance. Figure 2.9 schematically shows the cross-sectional view of the STAR detector with BEMC. The front of the calorimeter is located at a radius of 220 cm from and parallel to the beam axis. In the particle momentum range of $p_T > 0.5$ GeV/c, the time resolution is less than 80 ps [34]. The design of BEMC consists of 120 calorimeter modules and they are mounted 60 in ϕ by 2 in η . The full BEMC is composed of 4800 towers with segmented modules into 40 towers, 2 in ϕ , and 20 in η . The sampling system is based on lead and plastic scintillators for the detection of electromagnetic energy. To detect a scintillation light, optical structures with photomultiplier tubes (PMT) are used. There are 21 scintillation layers in the calorimeter. These layers alternate with 20 layers of lead absorber plates of 5 mm thick. The signal from each tile of the scintillator is read out by wavelength-shifting fibers. A 2.1 m multi-fiber optical cable carries the light to decoder boxes located at the outer surface of the magnet. In the decoder, the light from 21 tiles in a single tower is merged into a single PMT. The mean quantum efficiency of PMT is 13.3% at the wavelength delivered by the fibers of BEMC.

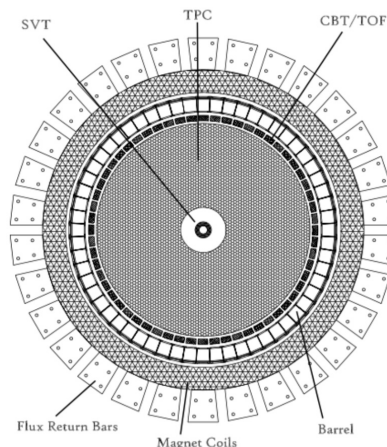


Figure 2.9: Cross-sectional view of STAR detector with the Barrel EMC covering $|\eta| \leq 1.00$

Zero Degree Calorimeter (ZDC)

The ZDC is used to detect neutrons and measure their total energy of them in the forward direction. The two identical ZDCs are centered in 0° and polar angle coverage < 2.5 mrad. Since the ZDC coincidence rate of the two-beam direction is a minimum bias selection in heavy ion collisions, it is used for the luminosity monitor [35] and event trigger. The ZDCs are located at each side with 18 (m) distance as shown in the vertical line with “A-A” of Fig. 2.10. After the charged particles are bent by the dipole magnet, the outgoing neutral particles are detected by the ZDC. The total width of the calorimeters is designed within 10 cm which is a nuclear interaction length in tungsten.

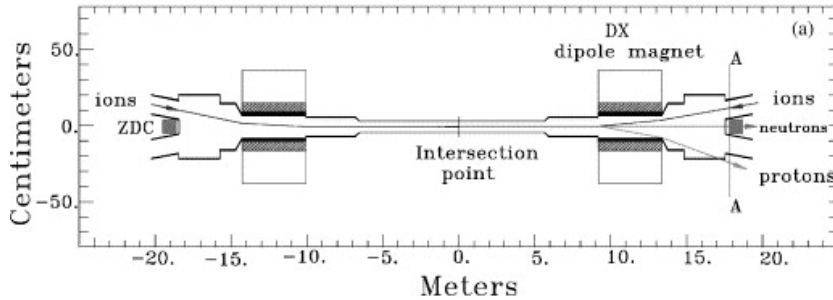


Figure 2.10: Side view of the collision region of the ZDC location indicating deflection of protons and charged fragments with $Z/A \sim 1$ downstream of the dipole magnet [15].

Generally, the neutrons are emitted from both target and beam nuclei in high energy collisions. They diverge by < 2 mrad from the beam axis in the RHIC with 100 GeV/nucleon. The neutral beam fragments are detected in THE “zero-degree” region at less than 44 mrad, where the charged fragments are too close to the beam trajectory.

The energy resolution is approximately a 10% of $\delta E/E \leq 20\%$ at neutron energy $E_n = 100$ GeV. This capability is reasonable to resolve the single neutron peak at peripheral nuclear collisions. The technique of sampling is based on transporting Cherenkov light created by charged shower secondaries in an optical fiber. Since the light is emitted nearly aligned with the optical fiber axis, the ZDC is most sensitive to charged particles which cross at around 45° to the fiber axis, which suppresses the lower energy shower component.

2.3 Beam Energy Scan program

To explore the phase structure, Beam Energy Scan (BES) program has been carried out in the STAR experiment for Au+Au collisions from 7.7 to 200 GeV. Table 2.1 shows the datasets collected at the STAR experiment for BES and $p+p$ collisions in 2012.

Table 2.1: Datasets of Beam Energy Scan program Phase 1 at the STAR experiment. Two collision systems, $p+p$ and Au+Au with energy, statistics, operation year, and μ_B are shown.

System	$\sqrt{s_{NN}}$	Events (10^6)	Year	μ_B (MeV)
Au+Au	200	238	2010	25
	62.4	43	2010	73
	54.4	550	2017	83
	39	92	2010	112
	27	31	2011	156
	19.6	14	2011	206
	14.5	14	2014	264
	11.5	7	2010	315
$p+p$	7.7	2.2	2010	420
$p+p$	200	220	2012	—

As mentioned in Sec. 1.4.1, the measurements between 2.4 – 7.7 GeV can be focused in the RHIC BES program phase two (BES-2) expected to achieve the uncertainties shown in the green shaded bands in Fig. 1.5. The BES-2 is ongoing with the upgrade of several detectors. They provide the better dE/dx resolution for PID and centrality determination. Table 2.2 shows the collision energy and corresponding μ_B for BES-2 datasets in Au+Au collisions.

Table 2.2: Datasets for Au+Au collisions of BES-2 at the STAR experiment. The data of 3, 9.2, 11.5, and 13.7 GeV are obtained fixed target (FXT) mode.

$\sqrt{s_{NN}}$	Events (M)	Year	μ_B MeV
27	560	2018	56
19.6	582	2019	06
14.6	324	2019	62
11.5	235	2020	16
9.2	162	2020	73
7.7	101	2021	20
3.0	565+	2018	21

Chapter 3

Analysis

3.1 Datasets

In this study, 200 million events taken in 2012 for $p+p$ collisions at $\sqrt{s} = 200$ GeV were analyzed to measure higher-order cumulants of net-proton distributions. In the STAR experiment, a minimum bias trigger is determined by a coincidence between the two ZDCs, which provides a minimally-biased indication of an interaction of heavy ions. The data were collected with the minimum bias events trigger provided by the VPD.

3.1.1 Event selection

The collision vertex positions are required to be within 30 cm from the center of the TPC along the beamline, and within 2 cm in the radial direction from the center of the beamline to remove the background events due to the interaction with beam pipe, respectively as shown in Fig. 3.1 and Fig. 3.2. During the long drift time of electrons in the TPC, superimposing of more than single-collision events are called pileup events. The pileup events can be suppressed by requiring the difference of the vertex positions along the beamline measured by the TPC and VPD to be within ± 3 cm as shown in Fig. 3.3. The events are required to have at least one primary track associated with a TOF hit with $\beta > 0.1$ to ensure that the TOF works properly.

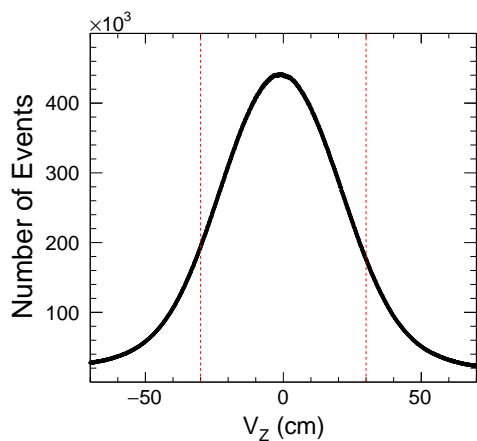


Figure 3.1: Distribution of the z-vertex positions (V_Z) from the center of the TPC along the beamline. The red lines represent the required condition of $V_Z \pm 30$ cm.

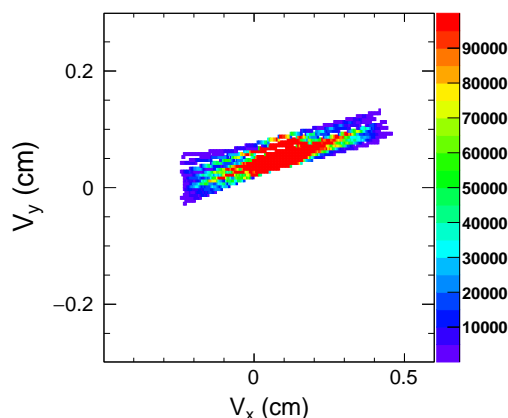


Figure 3.2: Distribution of the vertex horizontal and vertical (V_y) positions in the transverse plane at the center of the TPC.

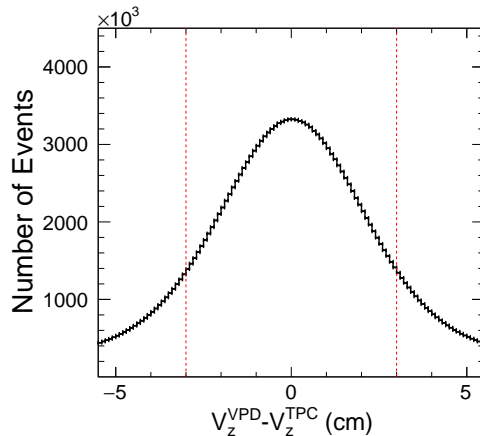


Figure 3.3: Difference between z-vertices positions measured by the VPD and TPC.

The multiplicity (m_{ch}) is defined by charged tracks excluding protons and antiprotons to suppress the autocorrelation effects. The detailed definition is listed in Tab. 3.1 with the cuts for (a) charged particle selection and (b) proton and antiproton rejection, where DCA represents the absolute value of the distance of closest approach, nHitsFit is the number of the TPC hits, m^2 means particle squared mass. The distribution of the multiplicity is shown in Fig. 3.4. Note that the cuts in (a) are looser than the track cuts for fluctuation analysis. In this study, events with $m_{ch} \geq 5$ are used for physics analysis. In the analysis of the heavy-ion collision, multiplicity is used for the centrality determination. The details are addressed in Section 3.1.4.

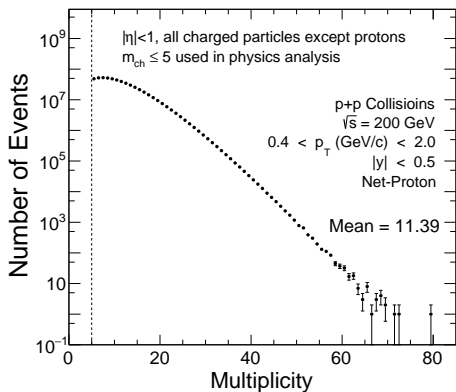


Figure 3.4: Multiplicity distribution in $|\eta| < 1$ for all charged particles in track fitting except for protons and antiprotons.

Table 3.1: Definition of multiplicity. The cuts for (a) charged particle selection and (b) proton and antiproton rejection are shown.

	Variable	Cuts
(a)	p_T	$> 0.1 \text{ GeV}/c$
	$ \eta $	< 1.0
	$ DCA $	$< 3 \text{ cm}$
	nHitsFit	≥ 10
(b)	$n\sigma_P$	< -3
	m^2	$< 0.4 (\text{GeV}/c)^2$

3.1.2 Track selection

Acceptance for protons and antiprotons are shown in Fig. 3.5 with respect to the rapidity and transverse momentum. The lower limit of p_T is set to remove the protons knocked out from the beam pipe. Figure 3.6 shows the distance of closest approach (DCA) distribution with the peak around 0.25 cm. To suppress secondary particles from Λ , DCA is required to be less than 1 cm. Figure 3.7 shows the distribution of the number of hits in the TPC (nHitsFit). To ensure the quality of the tracking, at least 20 hits in the TPC are required. In addition, 52% hits out of the number of possible hits on tracks are required to be used in track fitting. At least 5 hits are required to calculate dE/dx . The difference of the results calculated from the different track cuts will be included in the systematic uncertainties.

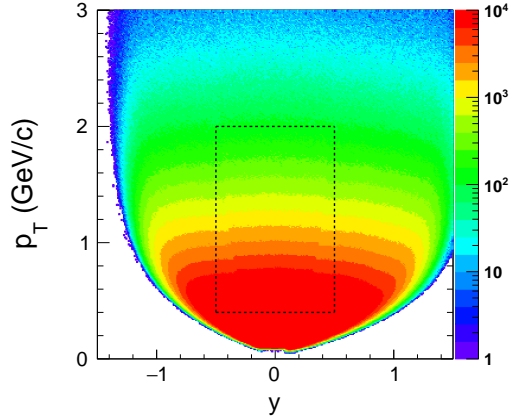


Figure 3.5: Distribution of p_T as a function of y of charged particles. The dotted square shows the kinematic region used for fluctuation analysis.

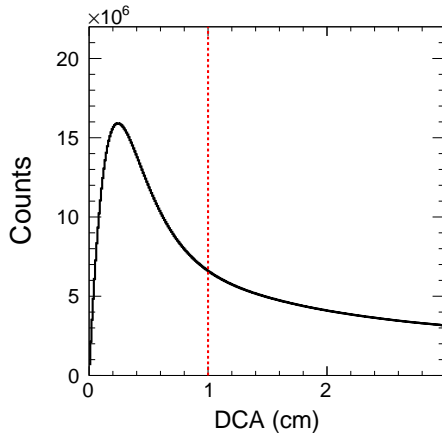


Figure 3.6: DCA distribution of the charged particles.

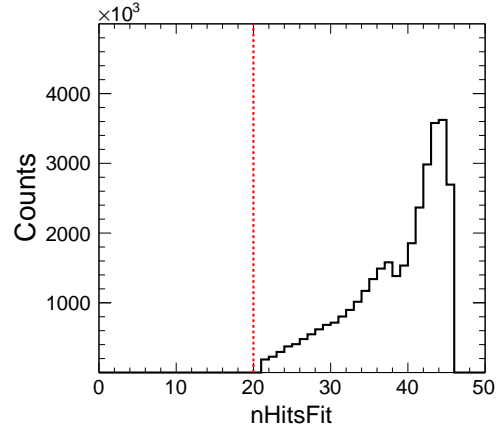


Figure 3.7: Distribution of the number of hits used in track fitting in the TPC. The red dotted line shows the track cut of 20 hits.

3.1.3 Particle identification

Protons and antiprotons are identified by the TPC and/or TOF for $0.4 < p_T < 2.0$ GeV/ c . Fig. 3.8 shows the momentum dependence of dE/dx of charged tracks measured by the TPC. In $0.4 < p_T < 0.8$ GeV/ c , protons and antiprotons can be separated from the other particle bands using the sigmatized width of dE/dx distributions ($|n\sigma_p| < 2$). On the other hand, the identified (anti)protons and other particle species merge at higher momentum regions, and thus dE/dx alone is insufficient to select (anti)protons with good purity. Figure 3.9 shows the momentum dependence of squared mass m^2 measured by the TOF. It is found that the (anti)proton distributions are separated from other particles. Therefore, a cut on the m^2 distribution, $0.6 < m^2 < 1.2$ (GeV/ c)², is additionally applied at $0.8 < p_T < 2.0$ GeV/ c . These are the cut conditions employed in net-proton fluctuation analysis for Au+Au collisions. It should be noted that, in this study for $p+p$ collisions, the m^2 cuts are required for the entire the p_T region, $0.4 < p_T < 2.0$ GeV/ c . More details will be discussed in Sec. 3.5.2.

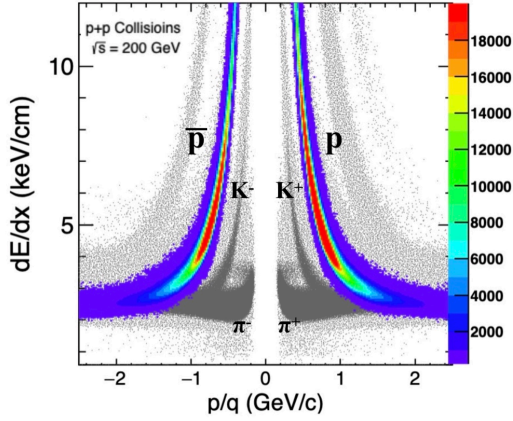


Figure 3.8: The dE/dx distribution of charged tracks as a function of momentum over charge (p/q). Colored dots show the identified protons by the TPC and TOF depending on transverse momentum. The black bands in the background represent various charged inclusive particles.

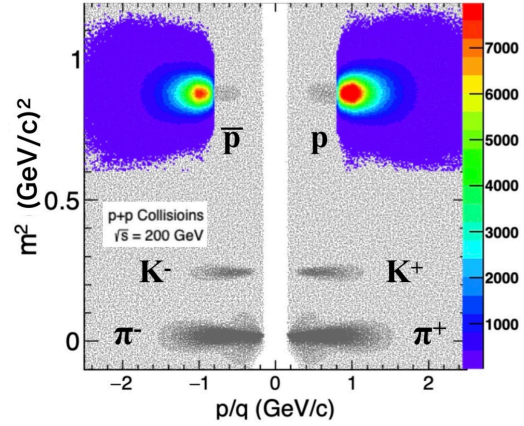


Figure 3.9: The squared mass distribution from the TOF as a function of p/q . Contour points show the identified protons by the TPC and TOF depending on transverse momentum. The black bands in the background represent various charged inclusive particles.

The event-by-event number of protons (N_p) and antiprotons ($N_{\bar{p}}$) are measured for each multiplicity as shown in Fig. 3.10. Event-by-event net-proton number (ΔN_p) distributions are shown in Fig. 3.11.

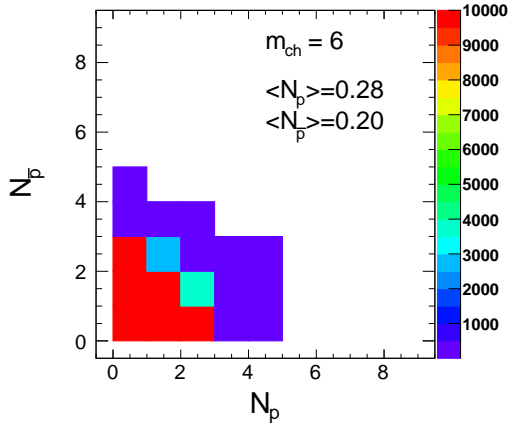


Figure 3.10: Event-by-event proton and antiproton number distribution at $m_{ch} = 6$ at $0.4 < p_T < 2.0$ GeV/c and $|y| < 0.5$.

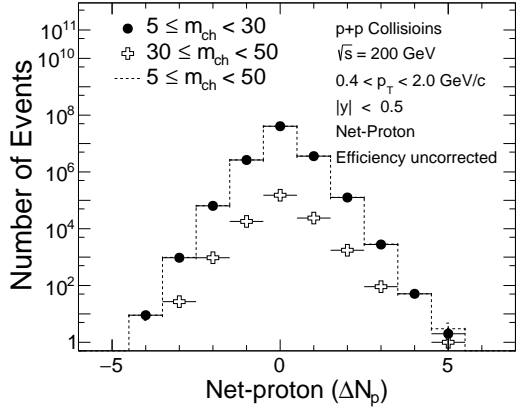


Figure 3.11: Event-by-event net-proton number distributions for 3 multiplicity classes. Black filled (cross) markers show the net-proton distribution for $5 \leq m_{ch} < 30$ ($30 \leq m_{ch} < 50$) multiplicity events. Dotted lines are corresponding to $5 \leq m_{ch} < 50$.

3.1.4 Event categorization

In heavy-ion collisions, various observables depend on the overlapping region of the two nuclei. Therefore, it is important to measure the observables divided into several centrality classes. The centrality is defined by impact parameter b . The b is the distance between the centers of each nucleus in the transverse direction as shown in Fig. 3.12, while it cannot be directly measured. For the centrality determination, the measured number of particles depending on b is used. The multiplicity distribution cannot be directly used due to decreasing of the trigger efficiency in the peripheral collisions. Therefore, multiplicity after correcting for the trigger efficiency using Monte-Carlo (MC) Glauber simulation is used. Figure 3.13 shows the drawing of a Glauber MC event with $b = 6$ fm in an Au+Au collision. The N_{part} is defined by

the number of nucleons having at least one inelastic collision as shown in the darker disks in the figure. The N_{coll} is defined as the number of inelastic collisions.

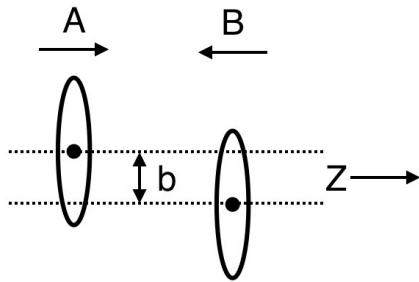


Figure 3.12: Schematic representation of Glauber Model geometry from the side view of the nucleus-nucleus collision.

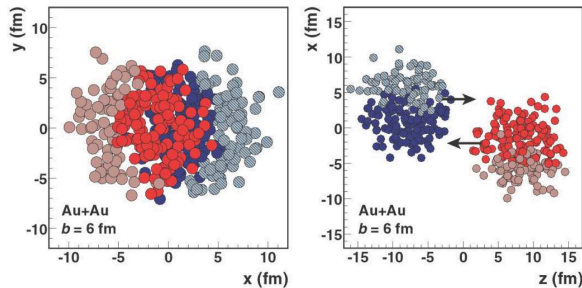


Figure 3.13: An illustration of the Glauber Monte-Carlo simulation in a $\sqrt{s_{NN}} = 200$ GeV Au+Au collision with the impact parameter $b = 6$ fm [16]. Left panel: geometry in the transverse plane. Right panel: geometry along the beam axis. Darker disks are participants, and lighter disks are spectator nucleons.

In this study, cumulants are calculated as a function of multiplicity. Several multiplicity classes are defined as Fig. 3.14 with Tab. 3.2. Multiplicities $5 \leq m_{ch} < 15$ are studied bin-by-bin, on the other hand, the region $m_{ch} > 16$ is divided into two wide multiplicity bin. The detail of this class definition is addressed in Sec. 3.5.5.

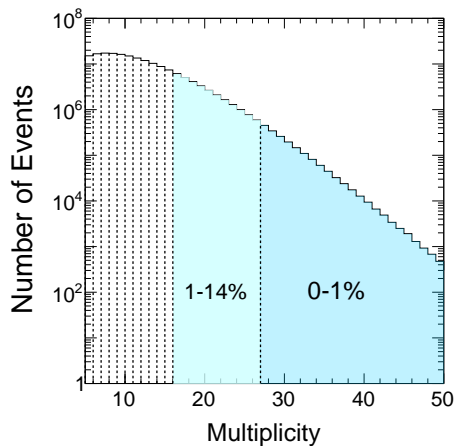


Figure 3.14: Multiplicity distribution with 13 class for $p+p$ collisions.

Table 3.2: Definition of multiplicity class for $p+p$ collisions. Multiplicities $5 \leq m_{ch} < 15$ are studied bin-by-bin.

Class	Multiplicity	Number of events (M)
Bin-by-bin	5	15
	6	17
	7	17
	8	17
	9	16
	10	15
	11	13
	12	12
	13	10
	14	9
	15	7
1-14%	$16 \leq m_{ch} < 27$	29
0-1%	$27 \leq m_{ch} < 50$	2

3.1.5 Run-by-run Quality Assurance (QA)

The data sets analyzed in this study were collected from February 8th to March 12th in 2012. In the fluctuation measurements, it is very important to ensure that the beam condition and the detector performance are stable in this long duration of the data taking [36].

The stability of the quality of the data sets has been checked as a function of “run”. The run represents one unit of the data taking, which is determined by the start/stop buttons in the data acquisition system. Each run roughly corresponds to 20 minutes in $p+p$ 200 GeV experiment in 2012. Event- and track-wise variables employed in the check are summarized in Tabs. 3.3 and 3.4. Those variables are averaged over all events and/or tracks within one run and plotted as a function of the run number in Figure 3.15. We

Table 3.3: Definitions of event variables checked in QA.

Observable	Definition	Detector
RefMult	Number of π^\pm, K^\pm, p^\pm at $ \eta < 0.5$	TPC
TofMult	RefMult measured in TOF	TOF
TofMatched	Number of the TOF matching tracks	TOF
TofMatchedbeta	Number of the TOF matching tracks with $\beta > 0.1$	TOF
V_x	Vertex in x-axis	TPC
V_y	Vertex in y-axis	TPC
V_r	Vertex for the radial direction	TPC
V_z	Vertex positions along the beam line	TPC
VPD V_z	Vertex positions along the beam line	VPD
Zdc Coincidence Rate	Coincidence rate	ZDC

first calculate the average value μ in each period for each variable, which is shown in the red solid line in Figs. 3.15 and 3.16. Next, the standard deviation, σ , is calculated within the period. The values for $\mu \pm 3\sigma$ are shown in green dashed lines. Runs outside the $\mu \pm 3\sigma$ lines are then labeled as bad runs and excluded from the analysis. As mentioned above, the known changes of the beam/trigger/detector conditions are reflected in the step-like structure in Fig 3.15. Hence the entire runs are divided into 6 periods, and the mean and sigma are evaluated for each period.

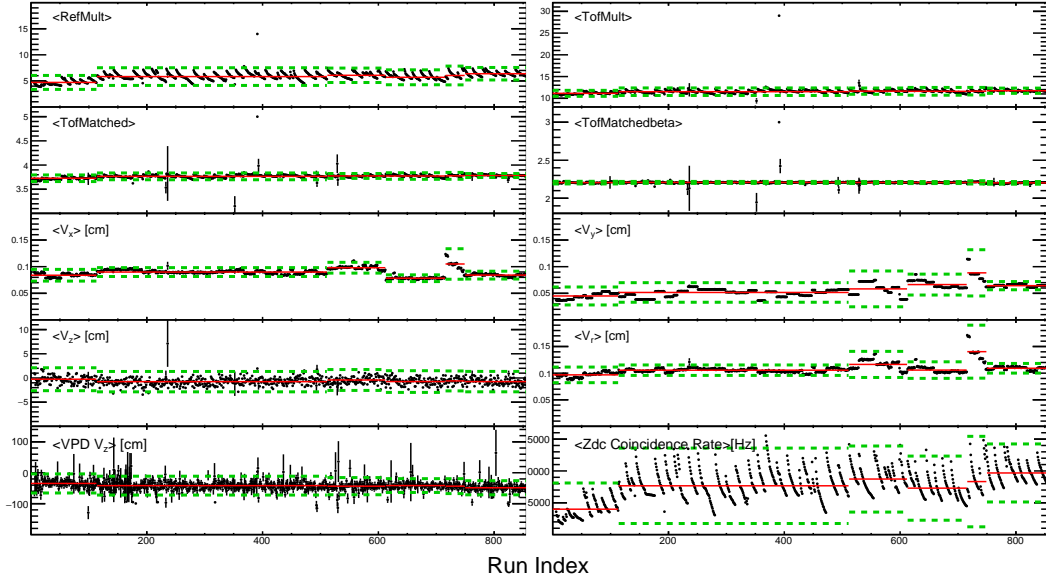


Figure 3.15: Average of event variables as a function of the run index. The red lines represent mean and green dotted lines represent $\mu \pm 3\sigma$. The bracket represents the average value over the event.

Based on Figs. 3.15 and 3.16, 8 sets of the bad run lists are defined. For each run, 10 event-wise variables and 8 track-wise variables are scanned. If greater than n variables are outside $\mu \pm 3\sigma$, then the run is labeled as the bad run. The procedures are done for each run and repeated by varying n from 0 to 7. Table A.2 shows the number of bad runs, percentage of bad runs to the total, and available statistics, for each value of n . To determine the final bad runs for fluctuation analysis, we calculated net-proton cumulants using the tightest and loosest cuts and found that both the results are consistent with each other within statistical uncertainties. Therefore, the bad run list for $n = 0$ was employed to keep as many statistics as possible, and finally 13 runs were excluded from the analysis.

Table 3.4: Definitions of track variables checked in QA.

Observable	Definition
p_T	Transverse momentum
η	Pseudo rapidity
ϕ	Azimuthal angle
$ DCA $	Absolute value of Distance Closest Approach
nHitsFit	Number of the TPC hits
nHitsDedx	Number of hits used for dE/dx
DCA_{xy}	DCA in x-y plane
DCA_z	DCA along the beam line

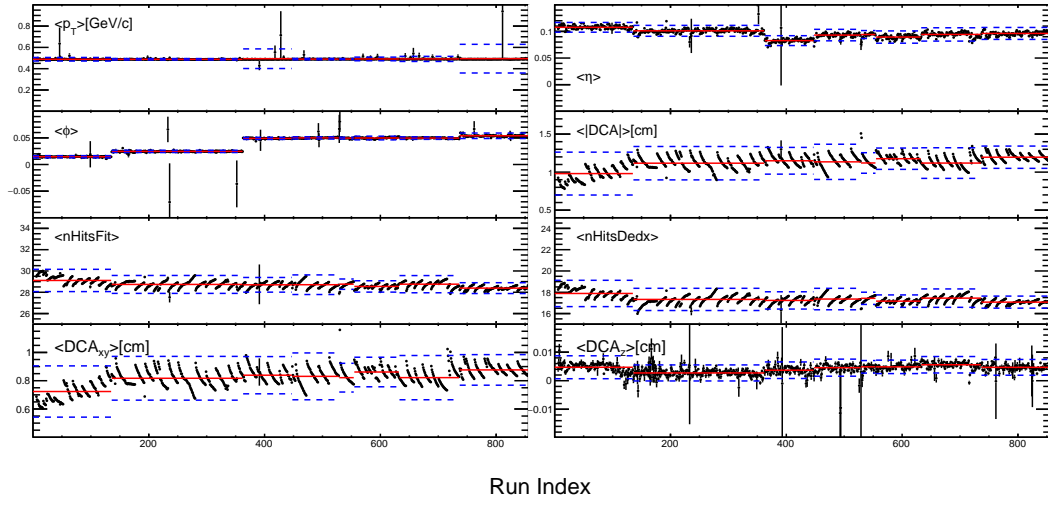


Figure 3.16: Average of track variables measured in the TPC as a function of the run index. The red lines represent mean (μ) and blue dotted lines represent $\mu \pm 3\sigma$. The bracket represents the average value over the event.

Table 3.5: The information of the n variables, counted the number of bad runs, percentage of bad runs to the total, and available statistics.

n variables	Number of bad run	Bad run fraction(%)	Available statistics
≥ 1 (the tightest)	133	7%	207M
≥ 2	51	1%	220M
≥ 3	26	0.1%	223M
≥ 4	22	0.1%	223M
≥ 5	18	0.07%	223M
≥ 6	16	0.001%	223M
≥ 7	13	0.001%	223M
≥ 8 (the loosest)	13	0.001%	223M

3.2 Efficiency correction

Emitted particles from nucleus collisions are missed by detectors with finite probability called efficiency. Since this imperfect efficiency can affect the shape of the net-proton distributions and their cumulants, measured cumulants need to be corrected for efficiencies. Correction methods have been developed in Refs. [37–39] based on the assumption that the efficiencies follow the binomial distribution [28, 37, 39–44].

$$B_{p,N}(n) = \frac{N!}{n!(N-n)!} p^n (1-p)^{N-n}, \quad (3.1)$$

where N and n are the numbers of produced and observed particles, respectively. However, it is known that the computational cost drastically increases if one employs more efficiency bins to take account into the non-uniformity of the detector efficiencies. To solve the issue, more efficient formulas were proposed in Ref. [44], which were derived using the factorial cumulants. The correction formulas are given by:

$$\langle Q \rangle_c = \langle q_{(1,1)} \rangle_c \quad (3.2)$$

$$\langle Q^2 \rangle_c = \langle q_{(1,1)}^2 \rangle_c + \langle q_{(2,1)} \rangle_c - \langle q_{(2,2)} \rangle_c \quad (3.3)$$

$$\langle Q^3 \rangle_c = \langle q_{(1,1)}^3 \rangle_c + 3\langle q_{(1,1)}q_{(2,1)} \rangle_c + \langle q_{(3,1)} \rangle_c - 3\langle q_{(3,2)} \rangle_c + 2\langle q_{(3,3)} \rangle_c \quad (3.4)$$

$$\begin{aligned} \langle Q^4 \rangle_c = & \langle q_{(1,1)}^4 \rangle_c + 6\langle q_{(1,1)}^2q_{(2,1)} \rangle_c - 6\langle q_{(1,1)}^2q_{(2,2)} \rangle_c + 4\langle q_{(1,1)}q_{(3,1)} \rangle_c + 3\langle q_{(2,1)}^2 \rangle_c + 3\langle q_{(2,2)}^2 \rangle_c \\ & - 12\langle q_{(1,1)}q_{(3,2)} \rangle_c + 8\langle q_{(1,1)}q_{(3,3)} \rangle_c - 6\langle q_{(2,1)}q_{(2,2)} \rangle_c \langle q_{(4,1)} \rangle_c - 7\langle q_{(4,2)} \rangle_c + 12\langle q_{(4,3)} \rangle_c - 6\langle q_{(4,4)} \rangle_c, \end{aligned} \quad (3.6)$$

with

$$q_{(r,s)} = q(a^r, \epsilon^s) = \sum_{i=1}^M (a_i^r / \epsilon_i^s) n_i, \quad (3.7)$$

where a is the sign of electric charge (-1 or +1) of the particles and ϵ is efficiency and n is number of tracks. With Eqs. 3.2–3.7, corrections are performed based on four efficiency bins defined by the charge and p_T ranges of using detectors as shown in Tab. 3.6. As explained in Chap. 2, the TPC is used for

Table 3.6: Definition of four efficiency bins with two-particle and two p_T ranges.

Particle species	p_T (GeV/c) range
Proton	$0.4 < p_T < 0.8$
	$0.8 < p_T < 2.0$
Anti-Proton	$0.4 < p_T < 0.8$
	$0.8 < p_T < 2.0$

(anti-)proton identification, and the TOF is additionally used at $0.8 < p_T < 2.0$ GeV/c.

Tracking efficiencies of the TPC are estimated in the embedding simulations. Monte-Carlo tracks of (anti)protons are embedded into the real data and reconstructed through the STAR-GEANT framework. The simulation is done for 1 million events. Then the fraction of the number of reconstructed tracks to embedded particles is used as an efficiency. TOF matching efficiencies are defined by using the experimental data as:

$$\epsilon_{\text{TOF}} = \frac{|n\sigma_P| < 2 \cap \text{TOF hit}}{|n\sigma| < 2}, \quad (3.8)$$

where the “ $|n\sigma_P| < 2$ ” is the number of identified protons reconstructed by the TPC, and “TOF hit” is the number of tracks matched to TOF hits. Figure 3.17 shows the p_T dependence of the TPC tracking efficiencies, TOF matching efficiencies, and total efficiencies obtained by multiplication of the TPC tracking efficiency and TOF matching efficiency for protons over the entire multiplicity region. The TPC tracking efficiency is at around 80%, while the TOF matching efficiencies are around 50% and combined efficiencies show 40 – 50% at high p_T . At low p_T , they are significantly decreasing with decreasing p_T , since low p_T tracks have fewer hits in the TPC and TOF, then the probability to reconstruct them

becomes small. Multiplicity-dependent corrections of cumulants are performed using the fit functions in Fig. 3.18. It should be noted that we finally took into account the luminosity dependence of efficiencies as well, which will be discussed in Sec. 3.5. For the centrality calibration, z-vertex positions are corrected so that the mean of their distributions becomes consistent among different luminosities.

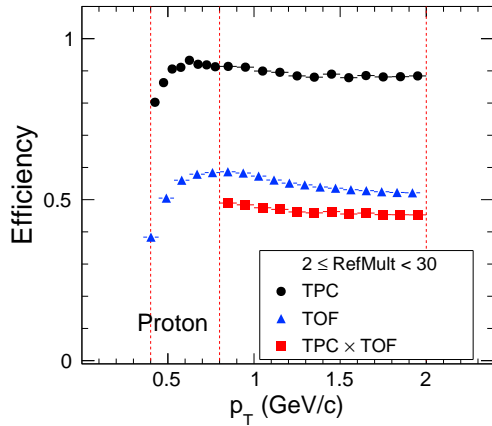


Figure 3.17: Transverse momentum p_T dependence of efficiencies at merged multiplicity over 2 to 30. Black dots and blue triangles show the TPC and TOF efficiency, respectively. Red squares show combined efficiency of them which are used at $0.8 < p_T < 2.0$ GeV/c. Red dotted lines show the $p_T = 0.4, 0.8, 2.0$ GeV/c.

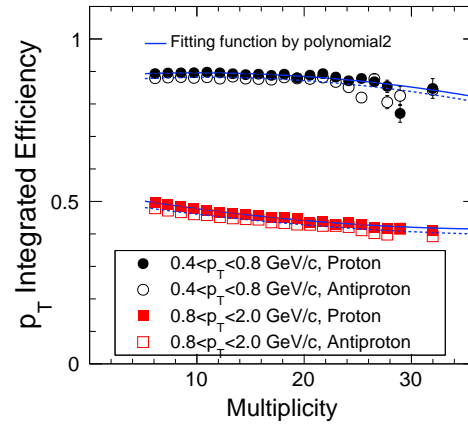


Figure 3.18: Multiplicity dependence of p_T integrated efficiencies for protons and antiprotons. Black dots show the TPC tracking efficiency at $0.4 < p_T < 0.8$ GeV/c. Red squares show combined efficiencies of the TPC and TOF at $0.8 < p_T < 2.0$ GeV/c. Solid (open) markers are protons (antiprotons). Blue solid (dotted) lines represent the second-order polynomial function of fitting for protons (antiprotons).

3.3 Centrality Bin Width Correction (CBWC)

Since the initial collision geometry cannot be directly measured, centrality is determined by the number of charged particles measured by the TPC. This leads to the volume fluctuations which arise from the variation of the initial geometry within one wide centrality bin (centrality bin width effects). Consequently, values of cumulants are enhanced by the volume fluctuations in heavy-ion collisions. To suppress the volume fluctuations, Centrality Bin Width Correction (CBWC) [45, 46] is applied. This correction is the weighted average of cumulants for each multiplicity bin with the number of events, which is given by:

$$C_n^{\text{CBWC}} = \frac{\sum_{i=0} w_i C_{(n,i)}}{\sum_{i=0} w_i}, \quad (3.9)$$

where w_i and $C_{(n,i)}$ are weight and cumulants in i th multiplicity bin, respectively. Figure 3.19 shows the examples of cumulants in Au+Au collisions up to fourth-order as a function of average number of participant nucleons $\langle N_{\text{part}} \rangle$ at $\sqrt{s_{NN}} = 62.4$ GeV [17]. It is found that the higher-order cumulants

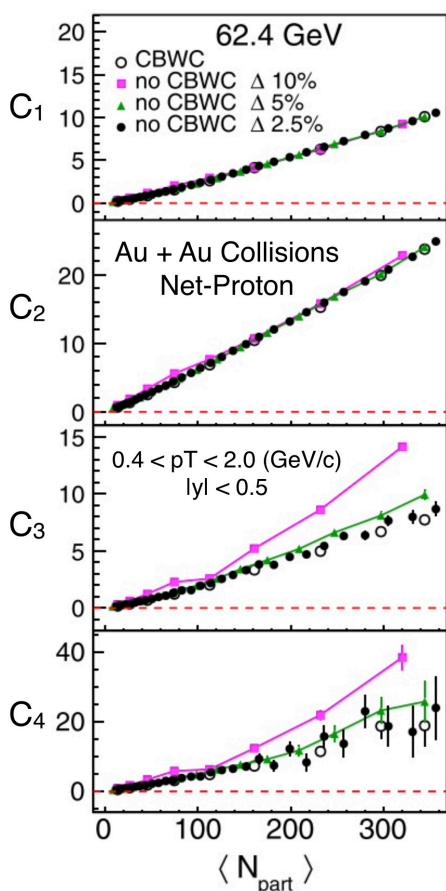


Figure 3.19: C_n of net-proton distribution in Au + Au collisions at $\sqrt{s_{NN}} = 62.4$ GeV as a function of $\langle N_{\text{part}} \rangle$ [17]. The results are shown for 10%, 5%, and 2.5% centrality bins without CBWC and for nine centrality bins (0–5%, 5–10%, 10–20%, ..., 70–80%) with CBWC. The bars are the statistical uncertainties.

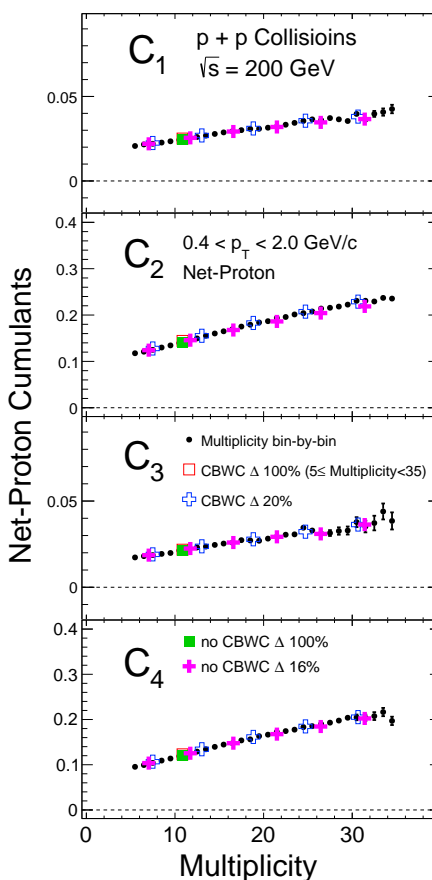


Figure 3.20: C_n of net-proton distribution in $p+p$ collisions at $\sqrt{s} = 200$ GeV as a function of multiplicity. The results of multiplicity bin-by-bin are shown in black dots. The results are shown for 100% (Multiplicity = 5 – 35) and 16% centrality bins without CBWC and for 100%, 20% centrality bins with CBWC. The bars are the statistical uncertainties.

without CBWC in 10% centrality bin width show significant enhancement at central collisions compared to the results of 5% and 2.5% bin width. On the other hand, the results in finer centrality bins become closer to the CBWC results. Therefore, the enhancement of cumulants with the wide centrality bin

width can be interpreted as the effect from the volume fluctuations in heavy-ion collisions, which can be suppressed by CBWC. In $p+p$ collisions, on the other hand, one expects no initial volume fluctuations since two protons always participate in the collisions. Figure 3.20 shows the results with and without CBWC of cumulants as a function of multiplicity in $p+p$ collisions at 200 GeV. It is found that the results of them almost overlap with multiplicity bin-by-bin cumulants, which indicates there are no effects of initial volume fluctuation. Consequently, the CBWC in $p+p$ collisions simply means the event average of cumulants over multiplicity.

3.4 Statistical uncertainties

Several methods such as Delta theorem [47] and Sub-group [48] have been developed to estimate statistical uncertainties in the fluctuation analysis. A general method that can be applied to correction by detector efficiencies in cumulant calculations is needed. An effective method is a bootstrap [43, 46], which is a numerical way to determine the statistical uncertainties. In the bootstrap, the original distribution is randomly sampled to make a new distribution. This procedure is repeated for 100 times, and the variation of the cumulants over the 100 iterations is taken as the statistical uncertainties.

To check the validity of this method, a toy model simulation is performed for a Skellam distribution with 100k events generated by two independent Poisson distributions with mean $m_1=10$ and $m_2=8$, respectively. Figure 3.21 shows 100 independently calculated fourth-order cumulants ($\langle Q^4 \rangle_c$) with the statistical uncertainties by bootstrap. It is found that they are around mean ($\langle Q^4 \rangle_c \sim 19$), and 62% $\sim 1\sigma$

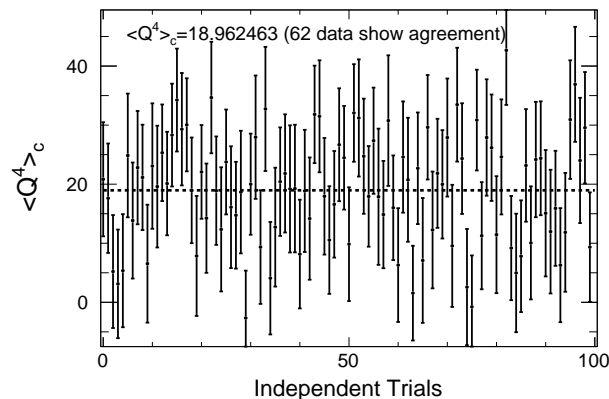


Figure 3.21: Toy model simulation of fourth-order cumulants ($\langle Q^4 \rangle_c$) with statistical uncertainties calculated by the bootstrap method. The x-axis is the number of independent trials for $\langle Q^4 \rangle_c$ calculations up to 100. Dotted lines show the average value of $\langle Q^4 \rangle_c$ over iteration.

of total results show agreement with the mean within statistical uncertainties, which indicates that the uncertainties are reasonably estimated by the bootstrap.

3.5 Effect of pileup events

Based on Sec. 3.1, to investigate the effects of pileup events, it is necessary to study several observables in terms of luminosity. In the STAR experiment, the coincidence rate of the ZDC is used as a proxy of luminosity. It is known that in Au+Au collisions the average multiplicity decreases with increasing the luminosity as shown in Fig. 3.22. This effect can be interpreted as convolutions two effects in high

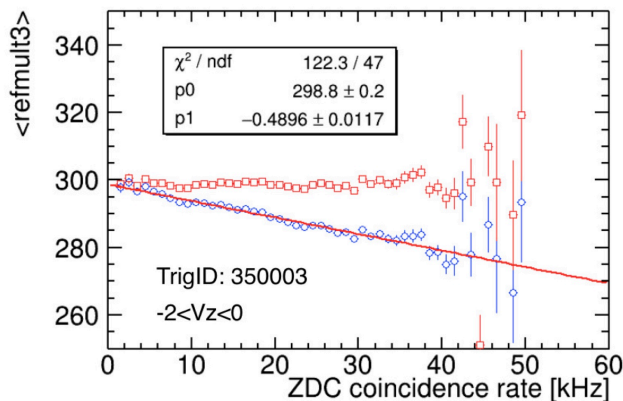


Figure 3.22: Averaged multiplicity as a function of the ZDC coincidence rate (Hz) at $-2 < V_z < 0$ cm in Au+Au collisions. Blue open diamonds indicate uncorrected multiplicity and red open squares show the corrected results. The red line represents the fitting linear function that is used for the corrections [18].

luminosity events: (1) Increasing of pileup backgrounds. (2) Decreasing of efficiency. It seems, in Au+Au collisions, the effect of (2) would be more significant compared to (1). To correct these effects, a correction is performed for each event by using the fit function in the red solid line. On the other hand, the luminosity dependence of the multiplicity looks opposite in $p+p$ collisions as shown in Fig. 3.23, which could indicate that the effect (1) is larger than (2). In Au+Au collisions, the luminosity dependence of the multiplicity can be understood as the decreasing of the detector efficiencies, and hence the effect on cumulants can be easily corrected in efficiency correction. On the other hand, the effect of pileup events on cumulants is not understood very well. In the following section, we have studied the effect of pileup events in some systematic approaches.

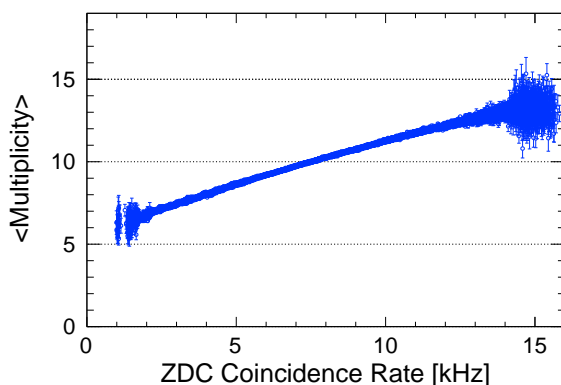


Figure 3.23: Averaged multiplicity as a function of the ZDC coincidence rate (Hz). Blue open circles indicate uncorrected multiplicity and red circles show the corrected reference multiplicity. The red line represents the fitting quadratic function that is used for the corrections.

3.5.1 Effect of pileup events on cumulants

To understand the effect of luminosity on cumulants, the range of luminosity is divided into high, middle, and low luminosity as shown in Fig. 3.24. The DCA distributions in these groups are shown in Fig. 3.25. A longer tail is seen in the high luminosity group as shown in green than those in the lower luminosity groups, which would indicate the increasing of backgrounds with luminosity. Further, Fig. 3.26 shows multiplicity dependence of C_1 for different luminosity groups, which looks different depending on the multiplicity. Although the lowest luminosity events have the fewest background, the statistics are reduced by the rejection of the events in higher luminosity regions. Therefore, we use the data in the whole luminosity region with the tuning of several variables depending on the luminosity. To do this, new methods of luminosity-dependent corrections of efficiency and multiplicity are needed for efficiencies and multiplicities.

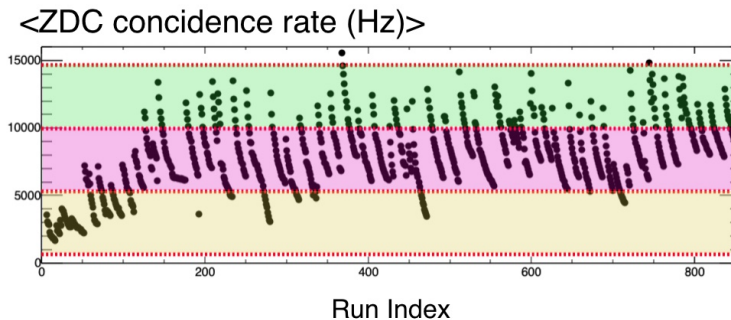


Figure 3.24: Luminosity grouping in the ZDC coincidence rate as a function of the run. The dotted red lines show the boundary of grouping.

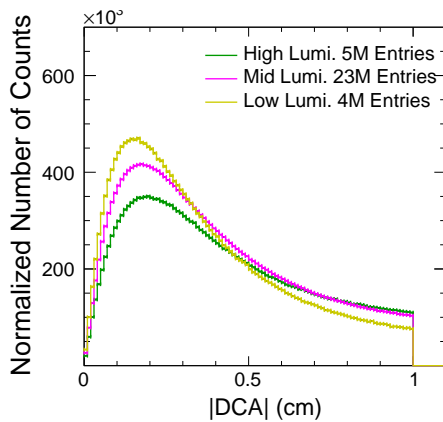


Figure 3.25: Distributions of absolute DCA value in three luminosity groups.

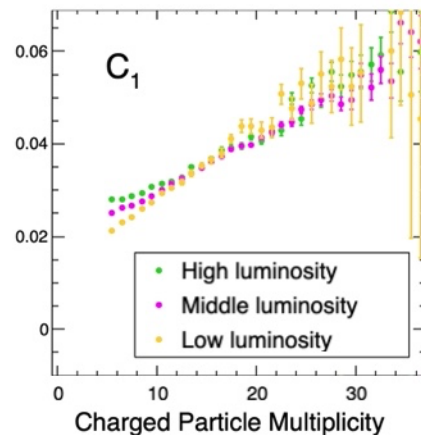


Figure 3.26: Multiplicity dependence of first-order cumulants in three luminosity groups.

3.5.2 Effects of pileup events on TOF matching efficiencies

As discussed in Sec. 3.5.1, the TOF matching efficiencies are estimated in the real data according to Eq. 3.8. The approach has been employed in Au+Au collisions in the STAR experiment. In $p+p$ collisions, however, the denominator in Eq. 3.8 includes backgrounds from pileup events inside the TPC, and hence the TOF matching efficiency cannot be estimated properly. Figure 3.27 shows the TOF matching efficiencies in low, middle, and high luminosity groups. It is found that they show different values for each luminosity over the entire p_T regions, which can be understood as effects from pileup events. Therefore, a proper approach is needed to extract the TOF matching efficiencies.

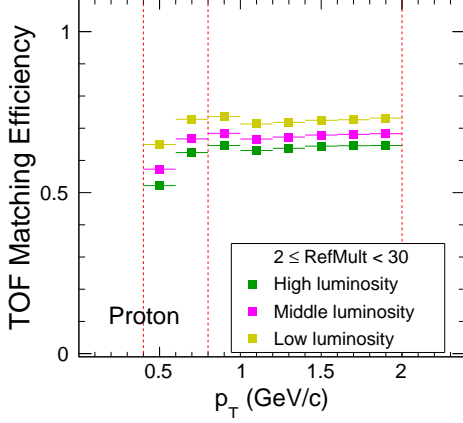


Figure 3.27: The TOF matching efficiencies for three luminosity groups in $2 \leq \text{Reference Multiplicity (RefMult)} < 30$. Green, pink, yellow markers show high, middle, low luminosity groups, respectively.

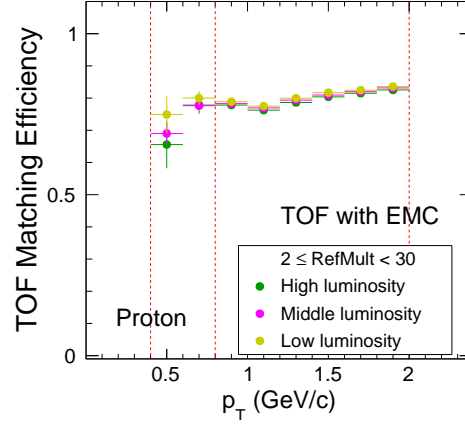


Figure 3.28: TOF matching efficiencies with the EMC hits requirement for three luminosity groups in $2 \leq \text{Reference Multiplicity (RefMult)} < 30$. High, middle, low luminosity groups are shown in green, pink, yellow, respectively.

To extract the pure efficiency of the TOF, a new definition of the TOF matching efficiency (ϵ') has been introduced, where the tracks are required to have hits in EMC as shown in Eq. 3.10.

$$\epsilon' = \frac{|n\sigma_P| < 2 \cap \text{TOF hit} \cap \text{EMC hit}}{|n\sigma_P| < 2 \cap \text{EMC hit}}. \quad (3.10)$$

Figure 3.28 shows the ϵ' as a function of p_T for these groups. It is found that the deviations between different luminosity results are reduced compared to Fig. 3.27, and the values become higher compared to Fig. 3.27.

3.5.3 Effects of pileup events on (anti)protons

Figure 3.29 shows the ZDC coincidence rate dependence of the average number of protons and antiprotons used for fluctuation analysis. They are identified using the TPC and TOF in $0.8 < p_T < 2.0 \text{ GeV}/c$, while only the TPC is used in $0.4 < p_T < 0.8 \text{ GeV}/c$. It is found that both of them increase with luminosity, which can be understood as effects from the pileup events. To suppress the effects, the TOF hits are required for all p_T regions as shown in Fig. 3.30. Now $\langle N_p \rangle$ and $\langle N_{\bar{p}} \rangle$ seems flat with respect to the ZDC coincidence rate, and therefore the effects from pileup events on (anti)protons for fluctuation analysis can be removed by requiring hits in TOF.

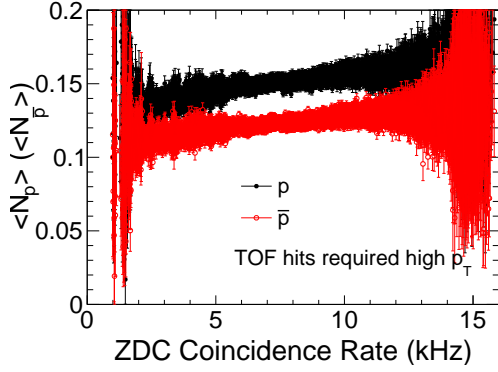


Figure 3.29: ZDC coincidence rate dependence of the average number of protons and antiprotons.

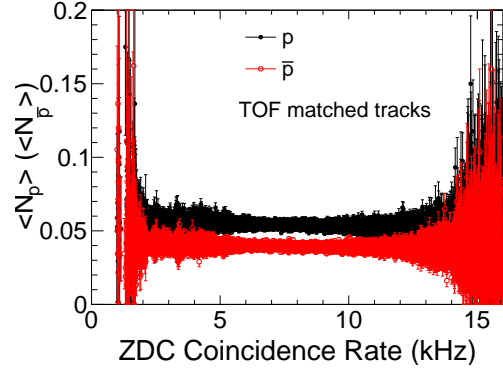


Figure 3.30: ZDC coincidence rate dependence of the average number of the TOF matched protons and antiprotons.

3.5.4 Luminosity correction of multiplicity

To study the luminosity dependence of multiplicity and efficiencies more systematically, ZDC coincidence rate distribution is divided into 10 groups so that each group has a comparable number of events as shown in Fig. 3.31. Grouping is performed based on the Tab. 3.7 with 21M events for each group. The $\langle \text{ZdcCo.} \rangle$ means the average number of ZDC coincidence rate calculated by event weighting from distribution in Fig. 3.31. The groups are named from lowest to highest as Group #0, #1, ..., #9.

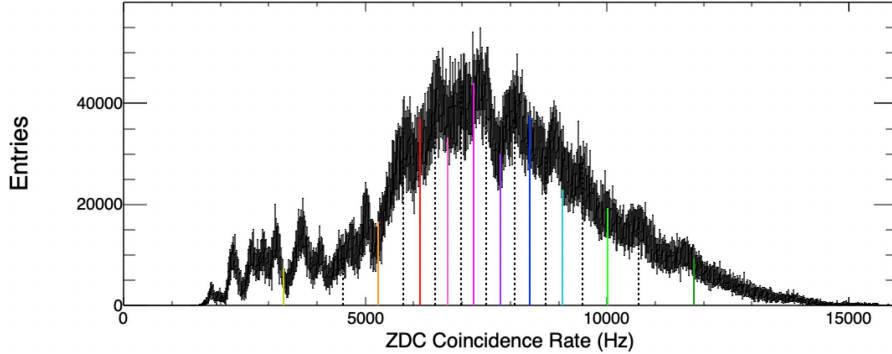


Figure 3.31: Distribution of the ZDC coincidence rate. Dotted lines represent the boundary line of 10 groups. Solid lines represent the average in each group.

Measured multiplicity distributions are shown in Fig. 3.32 for different luminosity groups.

The distributions show different mean values and shapes depending on the luminosity. To correct them, two methods of “Mean” and “Shape” corrections are developed.

Table 3.7: Definition of the grouping of luminosity based on ZDC coincidence rate (ZDCCo.) .

Lumi.No.	Start of ZDCCo. (Hz)	End of ZDCCo. (Hz)	$\langle \text{ZdcCo.} \rangle$
0	0	4530	3311
1	4531	5782	5273
2	5783	6439	6123
3	6440	6984	6708
4	6985	7496	7245
5	7497	8094	7794
6	8095	8726	8396
7	8727	9484	9084
8	9485	10656	10019
9	10657	16000	11800

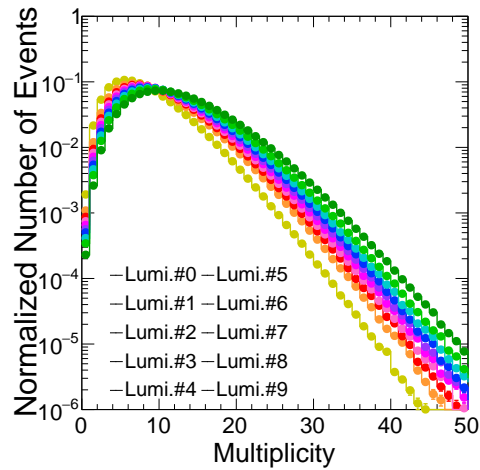


Figure 3.32: Distribution of multiplicity for each luminosity group. Each distribution is normalized with the number of events.

Table 3.8: Mean values of the multiplicity distributions for each luminosity group.

Lumi.#	Mean value of the distribution
0	7.60
1	8.78
2	9.25
3	9.57
4	9.86
5	10.15
6	10.45
7	10.80
8	11.26
9	12.09

Mean correction

For the mean correction, a luminosity-dependent scaling factor is multiplied to the multiplicity event-by-event. The scaling factor is determined by fitting the Fig. 3.23 using a polynomial function $f(x) = -0.0097x^2 + 0.67x + 5.5$. Figure 3.33 shows the uncorrected/corrected results in blue/red markers, respectively.

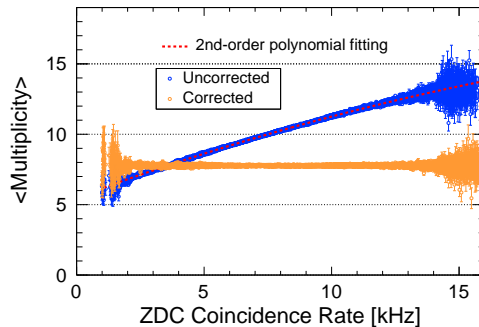


Figure 3.33: The ZDC coincidence rate dependence of average multiplicity over the events. The blue circles show uncorrected data. The red circles are mean corrected results by the fitting of blue data as shown in the red dotted line. The fitting function is second-order polynomial.

Shape correction

A shape correction modifies the multiplicity distribution at #1 – #9 so the shape becomes consistent with that in #0. To do this modification, the subtraction factor d is determined by: $d = \text{Mult}_{\#i} - \text{Mult}_{\#0}$, where $\text{Mult}_{\#i}$ is multiplicity in i th luminosity groups. The subtraction factor d is calculated at the same relative number of events as a difference between two high-normalized multiplicity distributions at two luminosities, one from the low (reference) luminosity and another one from the high luminosity as shown in Fig 3.34 for the luminosity group #9 at a given multiplicity. The factor d increases non-linearly with increasing the multiplicity as shown in Fig. 3.35. Similarly, the d in luminosity groups #0 – #8 are calculated as shown in black dots in Fig. 3.36. In order to obtain the subtraction factor d for the different luminosities from #0 to #8, the fitted function “ $f_d(\text{Mult})$ ” for the factor d of luminosity #9 is rescaled instead of the individual fitting for each luminosity. The scaling constants $p(\#i)$ for $i = 0 - 8$ are obtained by: $\langle d(\#i) \rangle / \langle d(\#9) \rangle$, where bracket represents the average value over multiplicity. As a results, the function “ $p(\#i)f_d(\text{Mult})$ ” of the factor d for all luminosity groups are obtained as shown in solid color lines in Fig. 3.37. For event-by-event measured luminosity, the values of d are obtained with respect to the ZDC coincidence rate by the fitting of $p(\#i)$ as shown in Fig. 3.37.

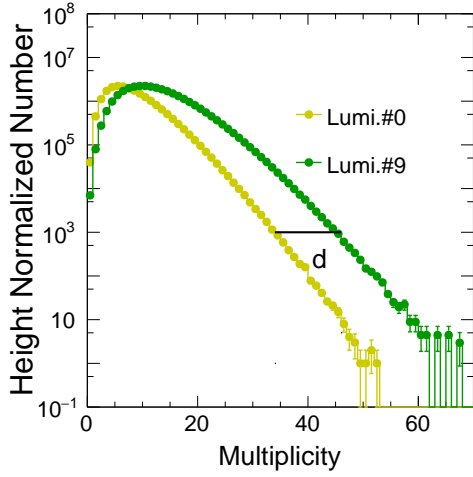


Figure 3.34: Multiplicity distributions and an example of the definition of the distance “ d ”. The yellow and green distributions are measured at luminosity groups #0 and #9, respectively. The areas and heights of them are normalized.

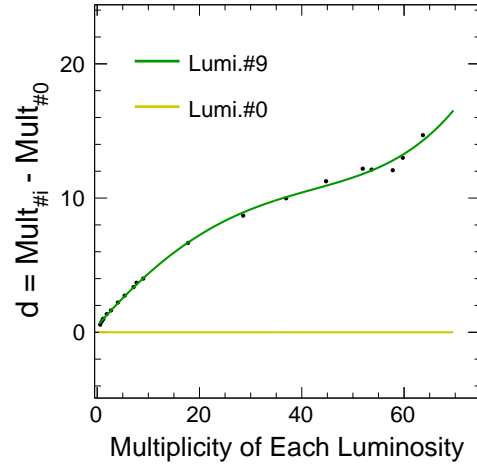


Figure 3.35: Multiplicity dependence of distance d for luminosity groups #0 and #9, where d is defined by the difference of multiplicities between each i th luminosity groups (“ $\text{Mult}_{\#i}$ ”) and the lowest luminosity (“ $\text{Mult}_{\#0}$ ”). The x-axis is the multiplicity for each luminosity. Solid lines show fitting functions using the fourth-order polynomial.

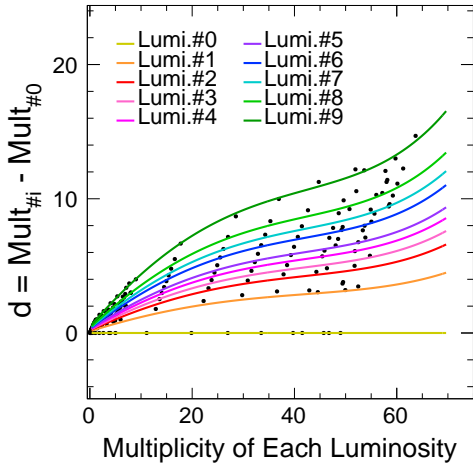


Figure 3.36: Multiplicity dependence of distance d for luminosity groups #0 to #9. The functions with different colors show the corresponding luminosity groups. The x-axis is the multiplicity for each luminosity.

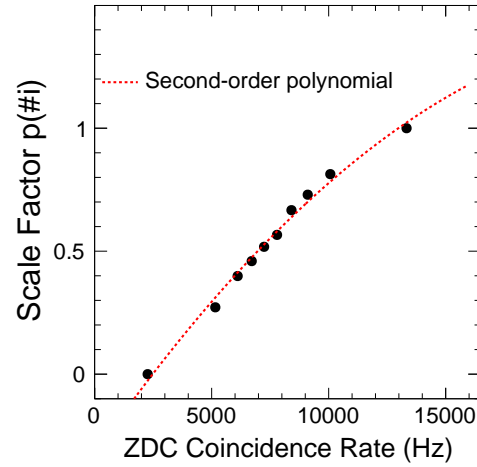


Figure 3.37: The ZDC coincidence rate dependence of scale factor $p(\#i)$ for i th luminosity groups. Red dotted lines show fitting functions using the second-order polynomial.

Validity of the method

The results of these two corrections are shown in Fig. 3.38 and 3.39, respectively. It is found that the mean values are consistent among different luminosity groups, which indicates the mean correction works well. However, there are visible differences in the tails of the distributions. For the shape correction, on the other hand, the distributions perfectly match each other. Figure 3.40 shows the multiplicity dependence of net-proton C_2 for different luminosity groups without any correction of multiplicity, which shows 20 ~ 30% deviation depending on the luminosity. Cumulants as a function of mean and shape

corrected multiplicity are shown in Fig. 3.41 and 3.42, respectively. It is found for both the methods that cumulants become closer compared to Fig. 3.40 among luminosity groups after corrections. In order to quantitatively evaluate the consistency of C_2 values among luminosity groups, χ^2 is calculated as follows:

$$\chi^2 = \frac{|C_n^{i,j} - C_n^{\text{average}}|}{\sqrt{\sigma_{n,i,j}^2 + \sigma_{n,\text{average}}^2}}, \quad (3.11)$$

where C_n^{average} or $\sigma_{n,\text{average}}$ are luminosity averaged results of C_n and statistical errors, and $C_n^{i,j}$ or $\sigma_{n,i,j}$ are for the i th multiplicity and j th luminosity. Figures 3.43 and 3.44 show the χ^2 distributions of C_2 with mean and shape corrections, respectively. It is found that the mean correction shows a smaller value of $\langle\chi^2\rangle$ compared to the shape correction. Similar studies are performed for the other orders of cumulants, and resulting $\langle\chi^2\rangle$ values are summarized in Tab. 3.9. For most orders of cumulants, $\langle\chi^2\rangle$ values are smaller for mean correction than shape correction, and therefore we decided to employ the mean correction.

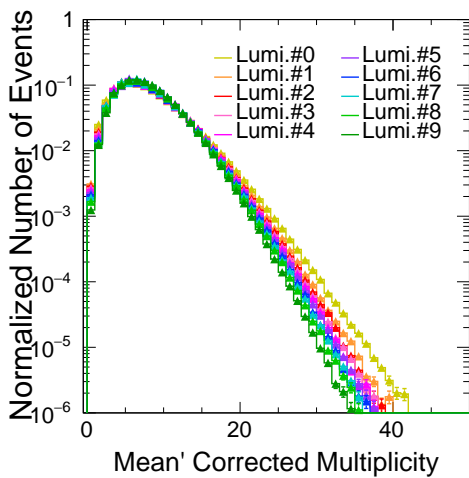


Figure 3.38: The distribution of luminosity corrected multiplicity for each luminosity group.

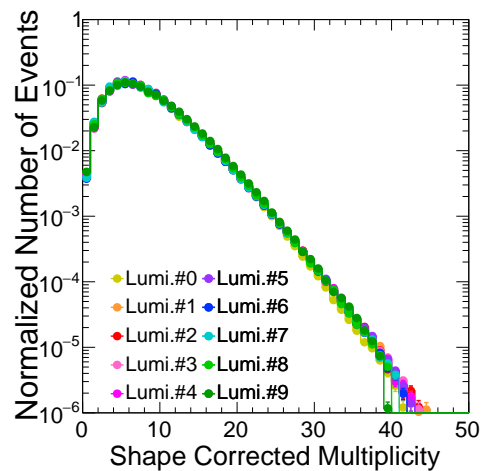


Figure 3.39: Shape corrected multiplicity distribution for each luminosity group. The area of the distributions is normalized to 1.

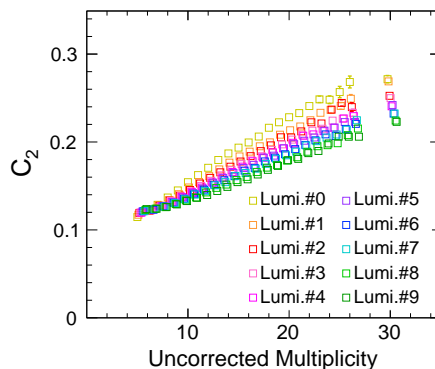


Figure 3.40: Multiplicity dependence of C_2 for each luminosity. The highest multiplicity values are merged over $27 \leq \text{Multiplicity} < 50$.

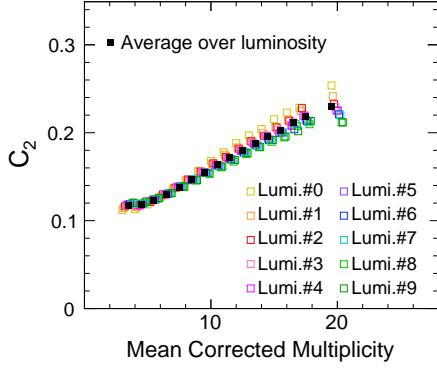


Figure 3.41: Mean corrected multiplicity dependence of C_2 for each luminosity. The highest multiplicity values are merged over $18 \leq \text{Multiplicity} < 30$. Black solid squares show the average over luminosity with $1/\sigma^2$ weighting.

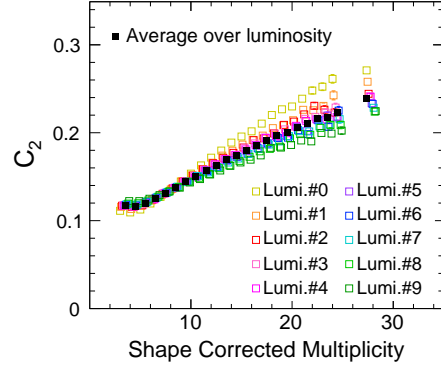


Figure 3.42: Shape corrected multiplicity dependence of C_2 for each luminosity. Multiplicities are merged from 18 to 30. The highest multiplicity values are merged over $25 \leq \text{Multiplicity} < 40$. Black solid squares show the average over luminosity with $1/\sigma^2$ weighting.

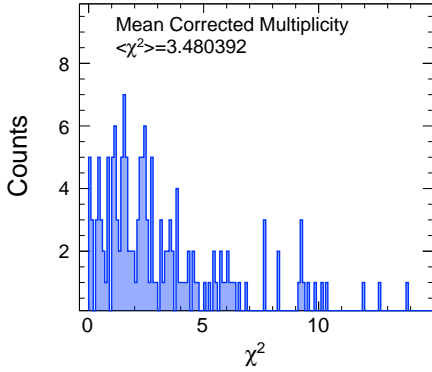


Figure 3.43: χ^2 distribution of C_2 with mean correction of multiplicity.

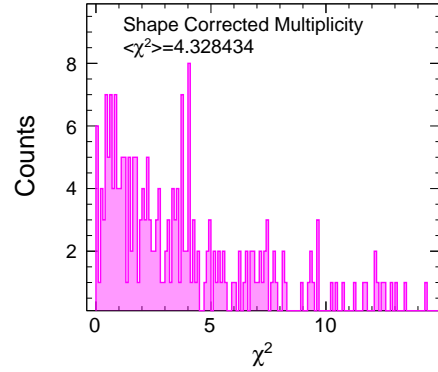


Figure 3.44: χ^2 distribution of C_2 with shape correction of multiplicity.

Table 3.9: Average $\langle \chi^2 \rangle$ for n th-order cumulants of uncorrected, mean corrected, and shape corrected multiplicity distributions, respectively.

C_n	Before correction	Mean correction	Shape correction
C_1	1.42	0.93	1.17
C_2	6.60	3.48	4.33
C_3	1.01	0.77	0.83
C_4	2.14	1.11	1.31
C_5	0.81	0.67	0.71
C_6	0.90	0.77	0.73

3.5.5 The necessary number of bins in net-proton distribution

In this analysis, cumulants are calculated in several parts of statistics to measure the multiplicity and luminosity dependence. Furthermore, a small number of particles in $p+p$ collisions affects the number of bins in net-proton distributions. In this section, we will discuss the important procedures for the calculation of cumulants to handle the artificial effects arising from the small number of bins.

The number of bins of the distribution is an important factor for the precise calculation of higher-order cumulants and their statistical uncertainties. For instance, C_1 represents the average value of the distribution, hence the distribution should have at least one bin. C_2 represents the width of the distribution so at least two bins are necessary. Similarly, one naively expects that n bins are needed in the distribution to calculate C_n .

Experimentally, the number of bins for net-proton distributions tends to decrease with increasing the multiplicity due to less event statistics at the tail of the distribution. At $m_{ch} \leq 18$, the net-proton number distributions have 6 bins. However, at the higher multiplicity, the 5 bins or fewer distributions appear in several luminosity groups. Top panels in Fig. 3.45 show the net-proton multiplicity distributions from one of the bootstrap samplings at $m_{ch} = 19$ for the luminosity group #9, #8, and #2. The distributions have 5, 6, and 7 bins, respectively. The lower three panels show the distribution of C_6 calculated for 100 bootstrap samplings. It is found that the distributions of bootstrap C_6 from the distributions having 5 bins show sharp peaks and short tails compared to those calculated from distributions with 6 or more bins. The width of the distributions are corresponding to statistical uncertainties of C_6 , and therefore the statistical uncertainties of C_6 cannot be properly estimated for the distributions having fewer bins than 6. Figure 3.46 shows the relationship between the number of bins of net-proton distribution and mean of statistical errors in C_6 over $18 \leq m_{ch} < 22$ and all luminosity data. The smaller errors are obtained in most 5 bin distributions than the 6 and 7 bin cases. Therefore, the multiplicity distribution is rebinned for $m_{ch} > 18$ to keep the number of bins above 6 in any luminosity. More details of net-proton number distributions and their number of bins are shown in App. D.1.

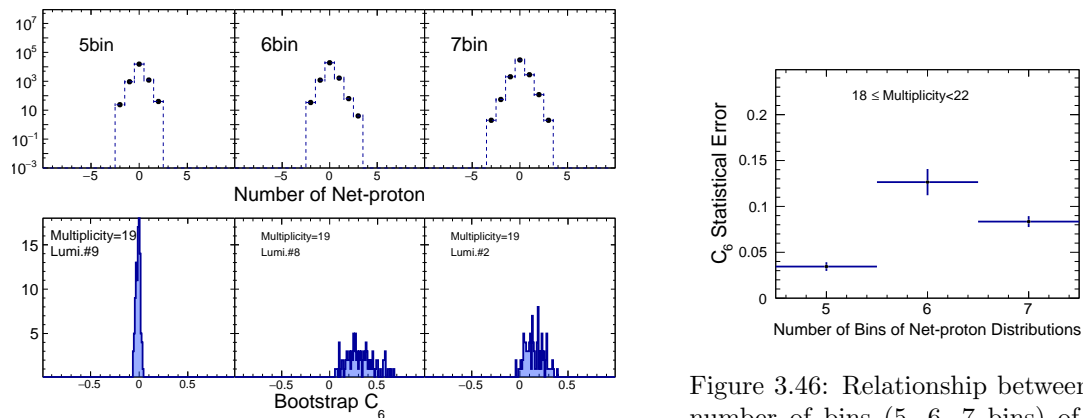


Figure 3.45: Net-proton distributions with 5, 6, 7 bins (upper panels) from left to right and bootstrap C_6 distributions from upper net-proton distribution with 5, 6, 7 bins (bottom panels) at $m_{ch} = 19$ in luminosity group #9, 8, 7, respectively.

Figure 3.46: Relationship between the number of bins (5, 6, 7 bins) of net-proton distribution and the average value of statistical uncertainties for C_6 over 10 luminosity groups at $18 < m_{ch} \leq 22$.

The multiplicity classes shown in Fig. 3.14 are based on the discussion in this section. The classes for mean corrected multiplicity distribution are determined as shown in Fig. 3.47 and Tab. 3.10. The cumulants are calculated based on the 14 multiplicity classes with $3 \leq m_{ch} < 15$ bin-by-bin and two wide bin at $m_{ch} \geq 15$.

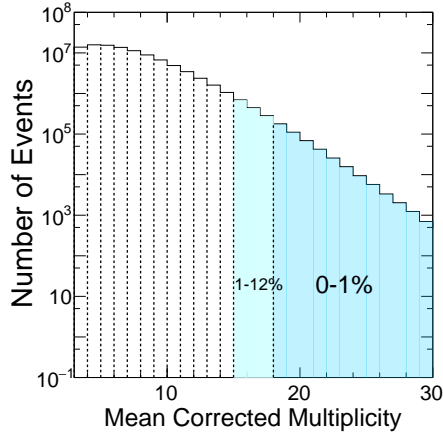


Figure 3.47: Multiplicity distribution with 14 class for $p+p$ collisions.

Table 3.10: Definition of multiplicity class for $p+p$ collisions. Multiplicities $3 \leq m_{ch} < 15$ are studied bin-by-bin.

Class	Multiplicity	Number of events (M)
Bin-by-bin	3	14
	4	16
	5	15
	6	14
	7	11
	8	9
	9	7
	10	5
	11	3
	12	2
	13	2
14	1	
1-12%	$15 \leq m_{ch} < 18$	29
0-1%	$18 \leq m_{ch} < 30$	2

3.5.6 Luminosity dependent efficiency correction

Efficiency for each luminosity

Luminosity dependent efficiencies are estimated for the TPC tracking efficiencies and the TOF matching efficiencies according to the methods discussed in Sec. 3.2. Figure 3.48 shows multiplicity dependence of the TPC \times TOF combined efficiencies for each luminosity group at $0.4 < p_T < 0.8$ GeV/c. The values are similar for most luminosity groups except for #0 and #9. Corresponding linear fitting functions are used for luminosity-dependent efficiency corrections.

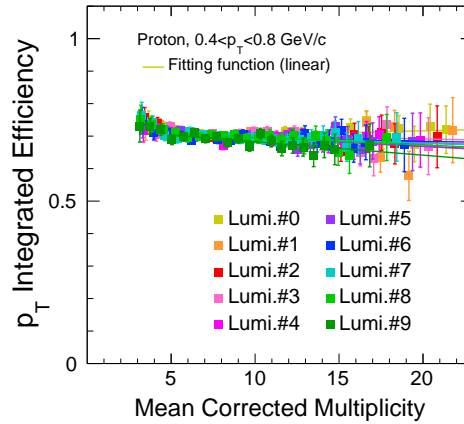


Figure 3.48: Luminosity-dependent efficiencies as a function of multiplicity for proton at low p_T . The solid line represents the linear fitting function.

Efficiency tuning

In the luminosity group $\#i$, the efficiency corrected C_1 ($C_1(i)$) should be identical between $i = 0 - 9$. However, since the measured $C_1(n)$ still have deviations between different luminosity, efficiencies need to be tuned. This tuning is based on the $C_1(0)$. Efficiencies ϵ in higher luminosity are then modified with factor $C_1(i)/C_1(0)$, where $C_1(i)$ are averaged C_1 over multiplicity in i th luminosity group. Modification factors are summarized in Tab. 3.11. Corrected efficiencies can be obtained by $\epsilon \times C_1(i)/C_1(0)$, where luminosity increases with increasing i . Figures 3.49 and 3.50 show the ZDC coincidence rate dependence

of (anti)proton and net-proton cumulants which are efficiency uncorrected, corrected, and corrected with modified efficiencies. The corrected C_1 averaged over multiplicity using the modified efficiencies are flat to the luminosity as shown in blue markers for both results of (anti)proton and net-proton. Since the efficiency tunings are based on the C_1 averaged over the multiplicity bin, remaining variations except for multiplicity dependence of cumulants will be taken into account in systematic uncertainties.

Table 3.11: Modification factor of efficiencies for each luminosity for proton and antiproton at low and high p_T region.

Lumi.No.	p, low p_T	\bar{p} , low p_T	p, high p_T	\bar{p} , high p_T
0	1	1	1	1
1	0.97	0.98	0.98	0.97
2	0.96	0.97	0.97	0.97
3	0.95	0.96	0.97	0.97
4	0.96	0.97	0.97	0.97
5	0.95	0.96	0.97	0.97
6	0.95	0.96	0.97	0.96
7	0.94	0.95	0.97	0.96
8	0.93	0.95	0.95	0.95
9	0.92	0.95	0.95	0.95

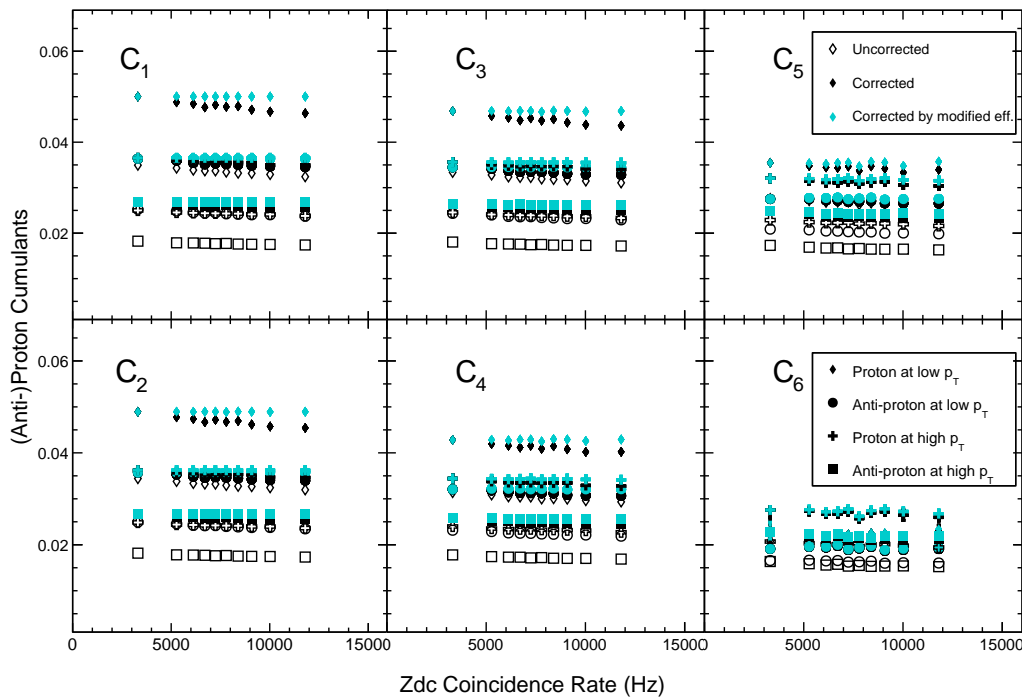


Figure 3.49: ZDC coincidence rate dependence of (anti)proton cumulants up to C_6 . Open and solid black markers show efficiency uncorrected and corrected cumulants, respectively. Solid blue markers show cumulants which are corrected by modified efficiencies. Diamond, circle, cross, and square indicate proton at low p_T , antiproton at low p_T , proton at high p_T , and antiproton at high p_T , respectively.

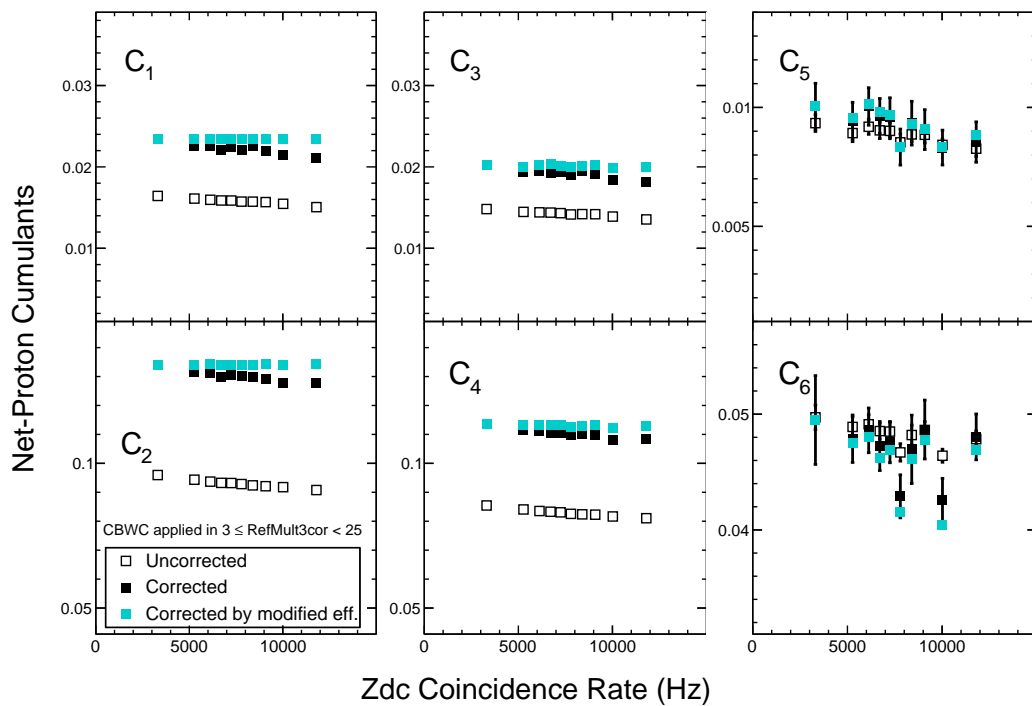


Figure 3.50: ZDC coincidence rate dependence of net-proton cumulants up to C_6 . Open and solid black squares show efficiency uncorrected and corrected cumulants, respectively. Solid blue squares show cumulants which are corrected by modified efficiencies.

3.6 Systematic uncertainties

Systematic uncertainties are estimated by varying the cut conditions for particle identification, track quality, efficiencies, and luminosity as shown in Tab. 3.12. The systematic calculation includes cut

Table 3.12: Variables and cut parameters for systematic study.

Variable	Default cut	Changed cut
$ n\sigma_p $	< 2.0	$< 2.5, < 2.3, < 2.1, < 1.9, < 1.7, < 1.5$
DCA(cm)	< 1.0	$< 1.5, < 1.3, < 1.1, < 0.9, < 0.7, < 0.5$
Number of the TPC hits	> 20	$> 15, > 17, > 19, > 21, > 23, > 25$
m^2	0.6-1.2	0.8-1.4, 0.7-1.3, 0.65-1.25, 0.75-1.35
Efficiency	0%	+5%, -5%, -5%(low p_T)+5%(high p_T), +5%(low p_T)-5%(high p_T)
ZDC coincidence rate (Hz)	0-16000	0- 4530, 4531-5782, 5783-6439, 6440-6984, 6985-7496, 7497-8094, 8095-8726, 8727-9484, 9485-10656, 10657-16000

parameters where the net-proton C_1 values vary from -5% to $+5\%$ for the default cut. For each cut condition on DCA and nHitsFit, efficiencies are estimated using embedding data. For the rest variables, efficiencies are modified so the C_1 values become the same as that from the default cut for each cut condition. The efficiency parameters and relative changes from default are summarized in Tabs. D.1 and D.2 in App. D.2.1. Systematic uncertainties σ_{sys} are estimated by following equations with different cuts on 6 variables:

$$\sigma_{\text{sys}} = C_n^{\text{def}} \sqrt{\sum_j R_j^2}, \quad (3.12)$$

$$R_j = \sqrt{\frac{1}{n} \sum_i \left[\frac{C_n^{i,j} - C_n^{\text{def}}}{C_n^{\text{def}}} \right]^2}, \quad (3.13)$$

where C_n^{def} and $C_n^{i,j}$ are n th-order cumulants with default cut, and i th cut condition in j th variable, respectively, and R_j represent the contributions for j th variable. The σ_{sys} are estimated for different acceptance of p_T and rapidity $|y|$ as shown in Tab. 3.13.

Table 3.13: Acceptance for $|\eta|$ and p_T .

Rapidity acceptance	Transverse momentum acceptance
$ y < 0.5$	$0.4 < p_T < 2.0 \text{ GeV}/c$
$ y < 0.4$	
$ y < 0.3$	
$ y < 0.2$	
$ y < 0.1$	
$ y < 0.5$	$0.4 < p_T < 1.7 \text{ GeV}/c$
	$0.4 < p_T < 1.4 \text{ GeV}/c$
	$0.4 < p_T < 1.1 \text{ GeV}/c$
	$0.4 < p_T < 0.8 \text{ GeV}/c$

Figure 3.51 shows an example of the systematic check for C_4/C_2 with the different cuts of 6 variables for averaged value over multiplicity. The results show that four different cuts on efficiency show the largest variations in the variables. The systematic check for other orders and multiplicity dependence of cumulants and their ratios are shown in Figs. D.18-D.25 in App. D.2.2. The results in different DCA cuts show the largest deviations for the lower-orders, while results in different luminosity become dominant for the higher-orders.

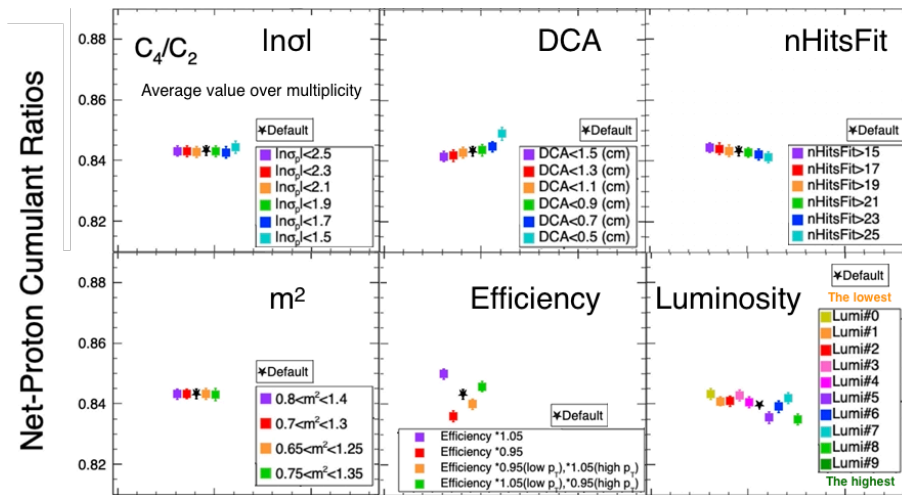


Figure 3.51: The averaged value of C_4/C_2 over multiplicity with each cut condition. Each panels show different variables, $|\ln\sigma_P|$, DCA, nHitsFit, m^2 , Efficiency, and Luminosity from top left to bottom right panel. The squares with different colors are each cut shown in the legends. The black stars show the C_4/C_2 with default cuts.

3.6.1 Barlow check

In order to remove statistical effects from systematic uncertainty, barlow check [49] is performed for each cut. This method uses the distribution of Δ/σ_{sc} to determine whether the distribution follow Gaussian or not. Δ and σ_{sc} are respectively defined as:

$$\Delta = C_n^{default} - C_n^{sys} \quad (3.14)$$

$$\sigma_{sc} = \sqrt{\sigma_{default}^2 - \sigma_{sys}^2}, \quad (3.15)$$

where $C_n^{default}$ and C_n^{sys} are cumulants or their ratios calculated with the default and different cut condition, respectively, and $\sigma_{default}$ and σ_{sys} are statistical uncertainties of $C_n^{default}$ and C_n^{sys} , respectively. Distributions satisfying the three or more conditions in Tab. 3.14 are considered to follow Gaussian, then the corresponding cut condition “passes” the barlow check. For this case, the cut condition is removed from the systematic calculations. The number of entries in the Δ/σ_{sc} distributions are totally 225 in-

Table 3.14: Four criteria of barlow check.

Variables	Criteria
Mean	< 0.2
RMS	< 1.2
Number of entries in $ \Delta/\sigma_{sc} < 1$	55 ~ 68%
Number of entries in $ \Delta/\sigma_{sc} < 2$	80 ~ 95%

cluding 25 multiplicity ($5 \leq m_{ch} < 30$) and 9 acceptance ($5 p_T$ and 4 $|\eta|$). Cuts of $|n\sigma_P|$, DCA, number of the TPC hits, m^2 , efficiency, and luminosity are investigated with cut conditions in Tab. 3.12. An example of the distribution of Δ/σ_{sc} for $|n\sigma_P| < 2.1$ cuts is shown in Fig. 3.52. The distributions for

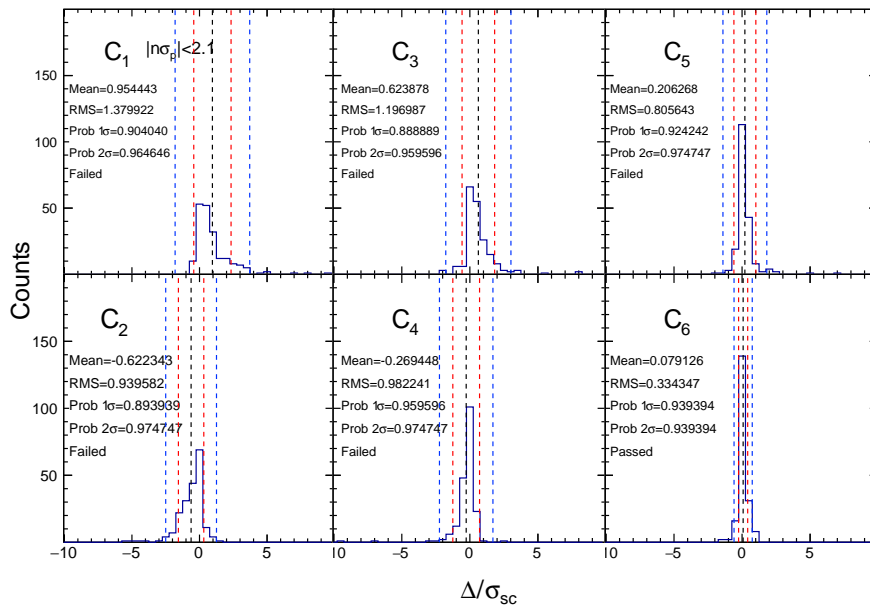


Figure 3.52: Distributions of Δ/σ_{sc} for net-proton cumulants up to sixth-order with $|n\sigma_P| < 2.1$ cuts. Black dotted lines show the mean of the distributions. Red and blue dotted lines show 1σ and 2σ of the distribution, respectively. For each panel, the results of the 4 criteria, Mean(μ), RMS, Prob 1σ , Prob 2σ , and whether they are “Passed” or “Failed” are described, where the Prob $1(2)\sigma$ is the probability of entry within $\mu \pm 1(2)\sigma$.

most orders of the cumulants failed Barlow checks except for C_6 satisfying three criteria, mean, RMS, and probability of entry within 2σ in the $|n\sigma_P| < 2.1$ cuts. The barlow check results for other cuts and

orders are shown in App. D.2.3. Consequently, 12 and 13 cuts out of 35 cuts of cumulant ratios passed Barlow check. Then the results of the systematic uncertainties are estimated using those with the barlow check “failed” cases.

Relative systematic uncertainties and R_j for cumulants and their ratios averaged over multiplicity are summarized in Tab. 3.15. For most orders, the contributions of efficiency and DCA cuts show the largest

Table 3.15: Contributions for systematic uncertainties (R_j) of cumulants and their ratios for six variables at $|y| < 0.5$ and $0.4 < p_T < 2.0$ GeV/ c . The values of cumulants and their ratios are averaged over multiplicity.

Order	$R_j \times 100$ (%)					
	$ n\sigma_p $	DCA	nHitsFit	m^2	Efficiency	The ZDC co. rate
C_1	0.04	2.47	0.23	0.07	2.79	1.81
C_2	0.02	1.23	0.31	0.04	2.46	2.33
C_3	0.18	2.57	0.23	0.07	2.38	1.70
C_4	0.07	1.13	0.20	0.06	2.00	2.10
C_5	2.98	4.63	0.87	0.57	0.56	5.92
C_6	1.09	1.21	0.91	0.37	2.66	6.17
C_2/C_1	0.06	1.22	0.23	0.09	0.33	0.37
C_3/C_2	0.14	1.37	0.36	0.09	0.12	0.66
C_4/C_2	0.04	0.12	0.13	0.02	0.53	0.31
C_5/C_1	2.34	1.53	1.10	0.60	3.48	6.48
C_6/C_2	0.98	1.49	1.47	0.28	4.56	7.10

R_j values in the six variables. The results with different DCA cuts include the effect of the increasing of secondary particles within a large DCA region. On the other hand, the luminosity contributions are dominant for the higher-order results. The results of relative uncertainties with different acceptance are shown in Tab. 3.16. The σ_{sys} of C_5 and C_5/C_1 show the larger uncertainties than the case of other orders

Table 3.16: Relative systematic uncertainties σ_{sys} (%) for cumulants and their ratios for five $|y|$ acceptance and four p_T acceptance. The values of cumulants and their ratios are averaged over multiplicity.

Order	$ y <$					$0.4 < p_T <$			
	0.5	0.4	0.3	0.2	0.1	1.7 GeV/ c	1.4 GeV/ c	1.1 GeV/ c	0.8 GeV/ c
C_1	0.06	0.04	0.08	0.08	0.14	0.04	0.04	0.05	0.04
C_2	1.46	1.16	0.85	0.55	0.25	1.43	1.38	1.27	1.01
C_3	3.20	3.13	3.00	2.32	1.48	3.25	3.32	3.55	3.26
C_4	2.88	2.61	2.14	1.48	0.81	2.93	2.96	2.97	2.67
C_5	20.6	19.7	18.3	12.9	7.69	20.7	20.4	21.2	16.8
C_6	13.1	12.1	9.97	6.49	3.43	13.5	13.8	13.8	11.0
C_2/C_1	1.25	0.97	0.67	0.41	0.64	1.23	1.17	1.03	0.75
C_3/C_2	2.39	2.51	2.60	2.17	1.59	2.46	2.55	2.88	2.97
C_4/C_2	1.56	1.54	1.36	0.98	0.57	1.62	1.70	1.80	1.74
C_5/C_1	19.8	20.5	18.7	13.2	7.94	21.5	21.1	21.7	17.3
C_6/C_2	12.5	11.7	9.66	6.24	3.27	12.9	13.3	13.3	10.6

for the 9 acceptance. For example, the percentage of uncertainties for C_1 is the largest when $|y| < 1$, on the other hand, for C_2 it is largest when $|y| < 0.5$. The acceptance that shows the largest percentage of the uncertainties is different for each order.

Chapter 4

Results

In this chapter, we will discuss the acceptance and multiplicity dependence of cumulants of net-proton number distribution up to sixth-order and their ratios, C_2/C_1 , C_3/C_2 , C_4/C_2 , C_5/C_1 , and C_6/C_2 in $\sqrt{s} = 200$ $p+p$ collisions. Effects of pileup events on the multiplicity dependence of cumulants will be discussed through a toy model. We also tried to require hits in the TOF in addition to the conventional multiplicity definition to remove the effects from pileup events from the multiplicity dependence of cumulants.

4.1 Acceptance dependence of cumulants

Rapidity acceptance dependence

The results of the rapidity ($|y|$) acceptance dependence of cumulants and their ratios are shown in Figs. 4.1 and 4.2, respectively. The plotted values are averaged over multiplicity. The cumulants show increasing trends with increasing of rapidity acceptance. In the higher-order results, the deviations from the Skellam baselines increase at large rapidity acceptance. PYTHIA 8 calculations with 100 million events are also shown for values of each order and Skellam. These PYTHIA 8 calculations are performed using the SoftQCD:all process with the Lund string fragmentation process for hadronization where color strings between partons fragment successively into final state hadrons. Baryon number conservation laws addressed in Sec. 5.2 are followed in PYTHIA 8. For odd-order cumulants, the data show smaller values than PYTHIA 8 calculations except for C_5 and even-order cumulants are larger than PYTHIA 8 calculations. The Skellam and cumulants calculated by PYTHIA 8 show almost identical values in odd-orders, on the other hand, there are deviations between them in even-orders. The deviations are larger at large acceptance compared to the case at small acceptance. The trends with acceptance increasing are qualitatively consistent with experimental data, while the values of PYTHIA 8 can not reproduce the data. The observed results can contain effects that cannot be explained by the options assumed in PYTHIA 8.

For the cumulant ratios, most of the orders show the closest values to the Skellam baselines at $|y| < 0.1$. The deviations become large with increasing of the rapidity acceptance except for C_3/C_2 . The C_5/C_1 and C_6/C_2 show larger decreasing trends compared to those of other orders with increasing of acceptance. The PYTHIA 8 calculations show The rapidity acceptance dependence of the deviations from the Skellam baselines can be caused by the effect of baryon number conservation which will be discussed in Sec. 5.2. In the PYTHIA 8 calculations, they show decreasing with increasing of acceptance except for C_3/C_2 , while they do not reproduce the observed cumulant ratios. In the case of C_4/C_2 , the PYTHIA 8 results almost overlap with the PYTHIA 8 Skellam baselines.

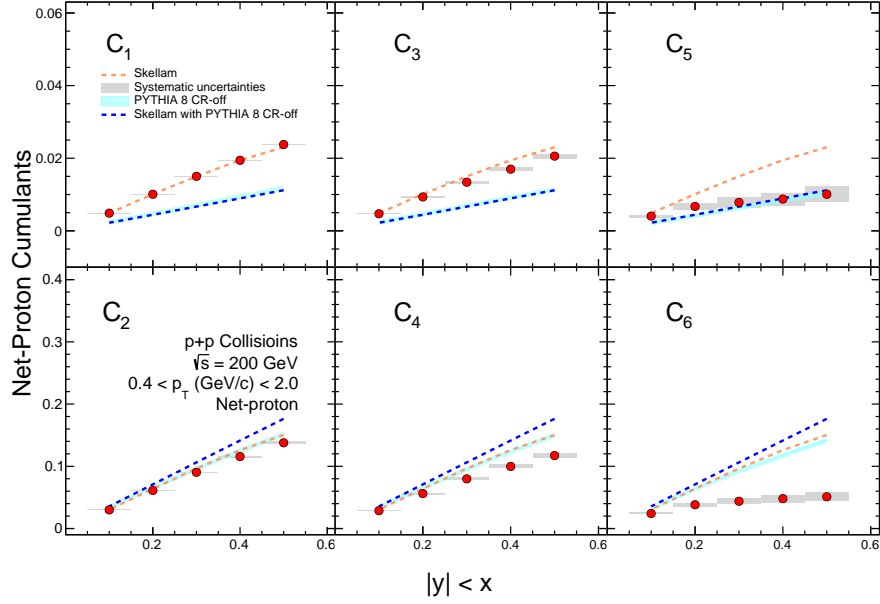


Figure 4.1: Rapidity (y) acceptance dependence of cumulants in $p+p$ collisions at $\sqrt{s} = 200$ GeV for $0.4 < p_T < 2.0$ GeV/ c and $|y| < 0.1 - 0.5$. The red points are averaged values over multiplicity. The dotted lines represent the Skellam baselines. The statistical uncertainties are smaller than the size of the markers. The shaded gray bands show the systematic uncertainties. The light blue bands are PYTHIA 8 calculations. The blue dotted lines represent the Skellam of PYTHIA 8 calculations.

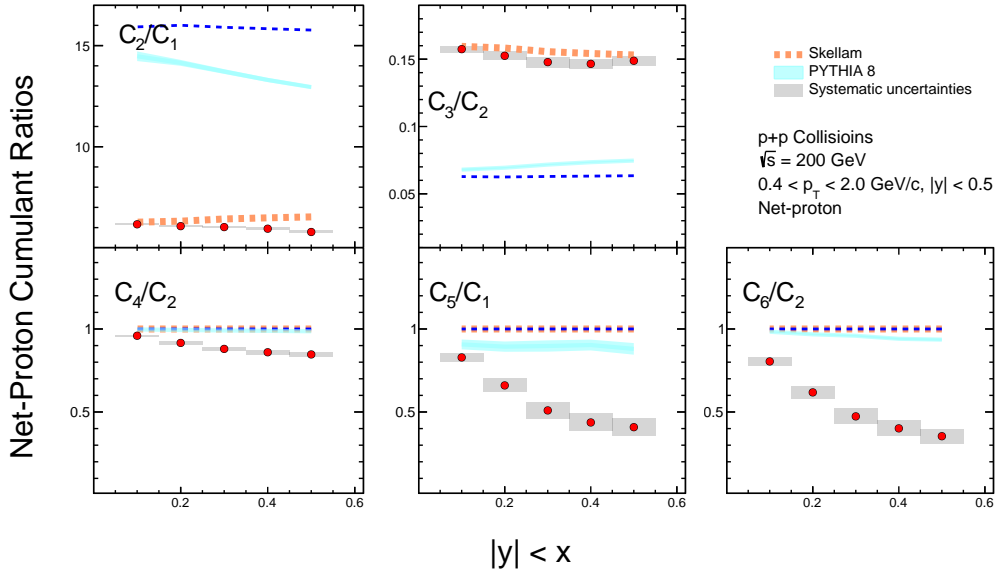


Figure 4.2: Rapidity (y) acceptance dependence of cumulant ratios in $p+p$ collisions at $\sqrt{s} = 200$ GeV for $0.4 < p_T < 2.0$ GeV/ c and $|y| < 0.1 - 0.5$. The red points are averaged values over multiplicity. The dotted lines represent Skellam baselines. The statistical uncertainties are smaller than the size of the markers. The shaded gray bands show the systematic uncertainties. The light blue bands are PYTHIA 8 calculations. The blue dotted lines represent the Skellam of PYTHIA 8 calculations.

Transverse momentum acceptance dependence

The p_T acceptance dependence of cumulants and their ratios are shown in Figs. 4.3 and 4.4. The cumulants show non-linearly increasing trends with increasing of the p_T acceptance. The larger deviations between data and Skellam baselines are found at the higher-order cumulants. The non-linearly increasing trends are also shown in PYTHIA 8 calculations. The PYTHIA 8 calculations reproduce the observed C_5 , while for other orders, they show smaller(larger) values compared to observed p_T acceptance dependence in odd-(even-)order.

The results of the cumulant ratios show non-linearly decreasing trends with increasing of p_T acceptance except for C_3/C_2 . For the higher-order results, the larger deviations between the data and Skellam baselines are observed. These deviations for the limited p_T acceptance can be expected due to the conservation effect. On the other hand, the PYTHIA 8 calculations show the increasing trends with p_T acceptance increasing for C_5/C_1 and C_6/C_2 . For other orders, PYTHIA 8 calculations do not reproduce the acceptance dependence of the data.

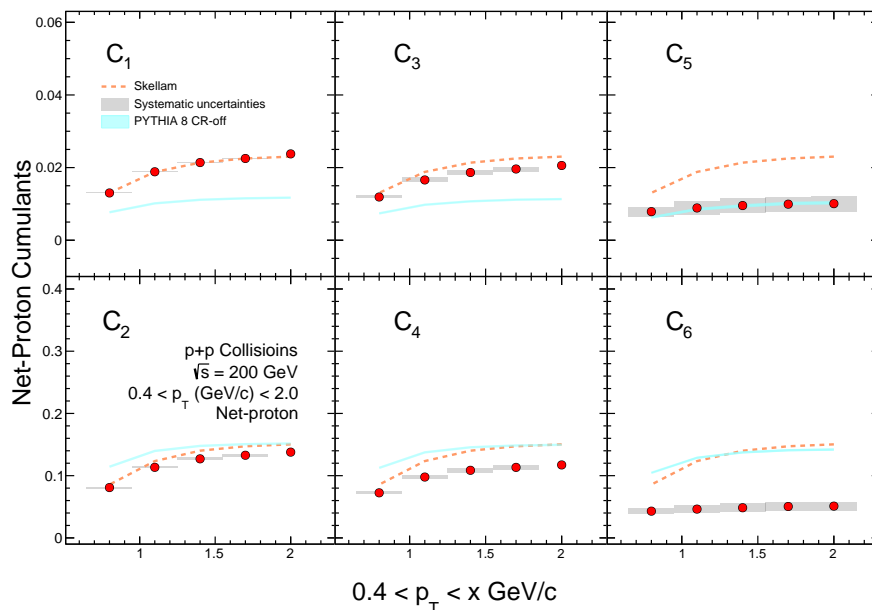


Figure 4.3: p_T acceptance dependence of cumulants at $\sqrt{s} = 200$ GeV $p+p$ collisions in $0.4 < p_T < 2.0$ GeV/ c and $|y| < 0.1 - 0.5$. The red points are averaged values over multiplicity at $3 < m_{ch} < 30$. The dotted lines represent Skellam baselines. The bars indicate the statistical uncertainties. They are smaller than the size of markers. The shaded bands show the systematic uncertainties. The light blue bands are PYTHIA 8 calculations.

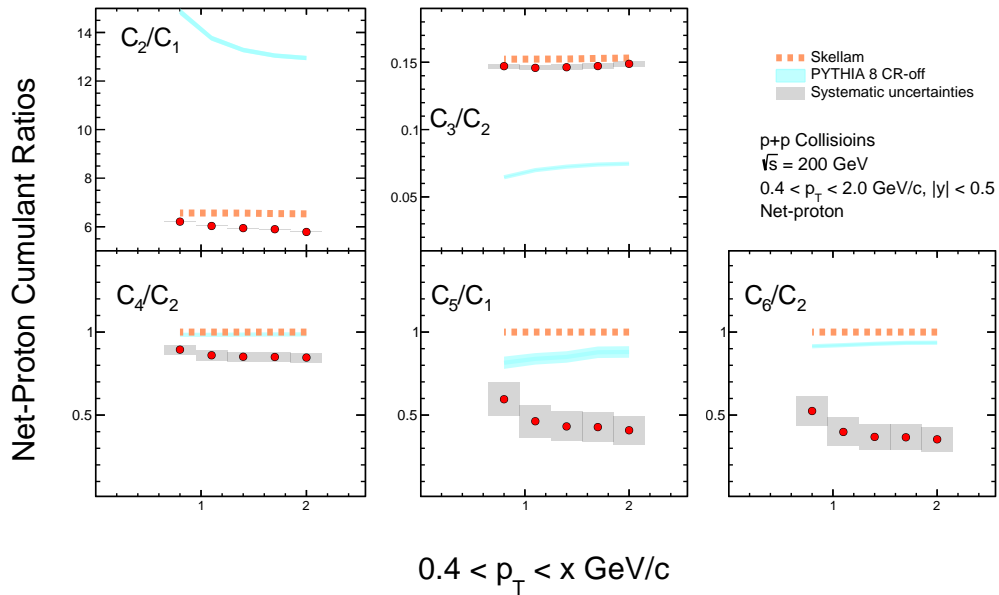


Figure 4.4: p_T acceptance dependence of cumulant ratios at $\sqrt{s} = 200$ GeV $p+p$ collisions in $0.4 < p_T < 2.0$ GeV/ c and $|y| < 0.1 - 0.5$. The red points are averaged values over multiplicity at $3 < m_{ch} < 30$. The dotted lines represent Skellam baselines. The bars indicate the statistical uncertainties. They are smaller than the size of markers. The shaded bands show the systematic uncertainties.

4.2 Multiplicity dependence of net-proton cumulants

Figure 4.5 shows the multiplicity dependence of the cumulants up to sixth-order. The values increase as the multiplicity increases, which is obvious from the trivial volume dependence of cumulants. There are large deviations for higher orders between observed cumulants and the statistical baselines. The results of PYTHIA 8 shown in red bands represent the string fragmentation model, so-called color reconnection (CR). The CR deal with the rearrangement of color fields after initial collisions, where the final step at the partons before hadronization is considered. The motivation to use this configuration is many color strings from multiple parton interactions overlap in physical space, which makes the separate identity of these strings questionable. This CR is implemented to be color connected with the total string length becomes as short as possible [50]. In the small systems, the observed flow-like patterns [32] in LHC can be provided an explanation by this CR mechanism [51]. For the average values of PYTHIA 8, C_2 with CR-off, C_4 with CR-on, and C_5 with CR-on/off reproduce the average value of data. The multiplicity dependence of the PYTHIA 8 show increasing trends, while the data and PYTHIA 8 are not consistent except for C_5 . The PYTHIA 8 calculations do not reproduce the data in both cases even if the effect of CR is included.

The multiplicity dependence of the cumulant ratios is measured as shown in Fig. 4.6. The results

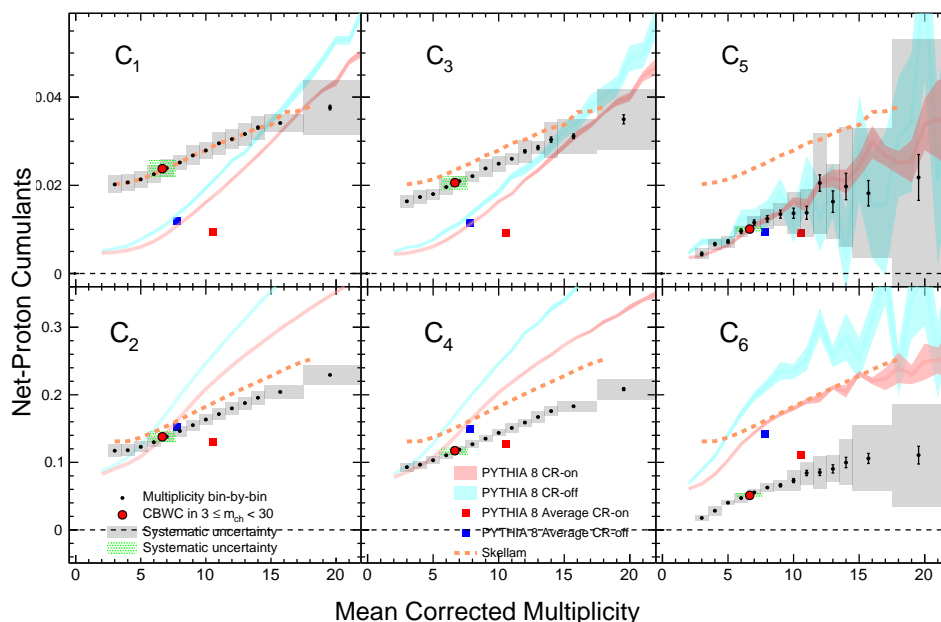


Figure 4.5: Net-proton cumulants up to the sixth-order as a function of multiplicity in $p+p$ collisions at $\sqrt{s} = 200$ GeV for $0.4 < p_T < 2.0$ GeV/c and $|y| < 0.1 - 0.5$. Red points represent the average over the multiplicity region $3 < m_{ch} < 30$. The dotted lines represent Skellam baselines. The bars indicate the statistical uncertainties. The gray and green shaded bands show the systematic uncertainties for multiplicity bin and average values. The values at $17 < m_{ch} < 30$ are calculated in one centrality bin.

of C_3/C_2 are consistent with the statistical baseline, which would be accidentally caused by a similar degree of deviations from the statistical baseline for both the second- and third-order cumulants. On the other hand, for the higher-order results, large deviations are seen from the statistical baselines with the hierarchy of the deviations $C_4/C_2 < C_5/C_1 < C_6/C_2$. These deviations of average results for data and PYTHIA 8 calculations can be considered due to the baryon number conservation effects addressed in Sec. 5.2. The average values of PYTHIA 8 with CR-off are closer to data compared to CR-on cases except for C_4/C_2 , while both CR-on and off can not reproduce the average results of the data. The multiplicity dependent results of the PYTHIA 8 decrease with increasing the multiplicity except for C_3/C_2 , where the C_4/C_2 , C_5/C_1 , and C_6/C_2 have peaks at $m_{ch} \sim 7$. The higher-order results of PYTHIA 8 at high multiplicity $m_{ch} > 15$ are overlapping with the data within uncertainties, while they do not reproduce the trends of the observed cumulant ratios for the entire multiplicity region.

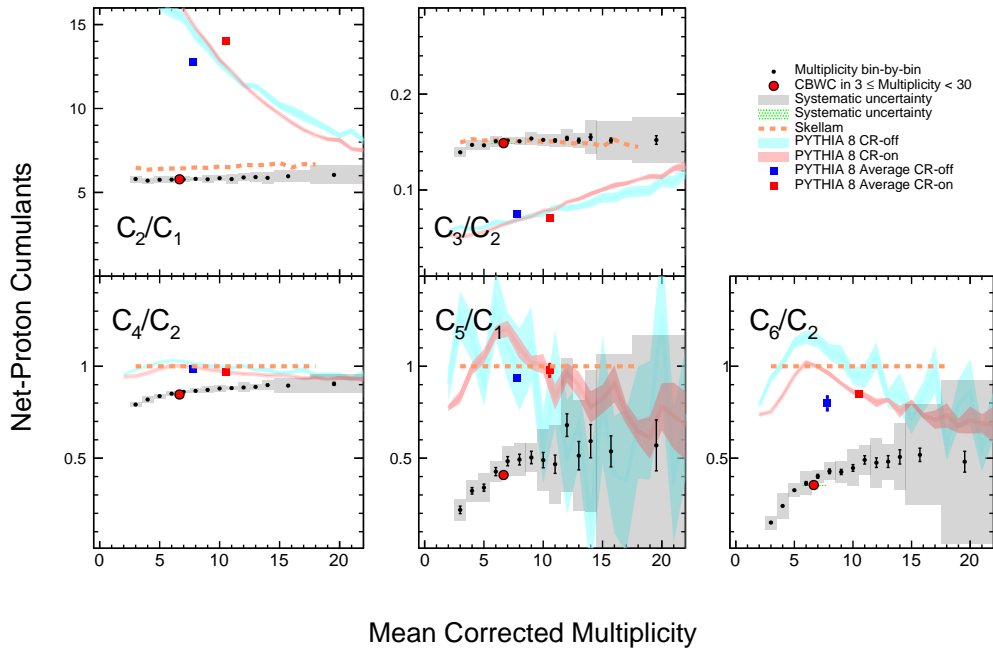


Figure 4.6: Multiplicity dependence of net-proton cumulant ratios in $p+p$ collisions in $p+p$ collisions at $\sqrt{s} = 200$ GeV for $0.4 < p_T < 2.0$ GeV/ c and $|y| < 0.1 - 0.5$. Red points represent the average over the multiplicity region of $3 < m_{ch} < 30$. The dotted lines represent the Skellam baselines. The bars indicate the statistical uncertainties. The gray and green shaded bands show the systematic uncertainties for multiplicity bin and average values. The values at $14 < m_{ch} < 18$ and $17 < m_{ch} < 30$ are calculated as one multiplicity bin.

β

4.3 Luminosity independent multiplicity

As we discussed in Chapter 3, corrections of multiplicity distributions are applied to the conventional particles multiplicity to take care of the effects from pileup backgrounds, then cumulants were measured as a function of the corrected multiplicity. However, it would be best if we can find an observable which does not depend on the luminosity, and use it instead of the conventional multiplicity. The TOF matched multiplicity m_{ch}^{TOF} , is defined by charged particles in $|\eta| < 1.0$ and $p_T > 0.5$ GeV/c excluding protons and antiprotons. The exclusion of proton and antiprotons is done by selecting particles that satisfy $n\sigma_P < -3$ and $m^2 < 0.4$. Figure 4.7 shows the ZDC coincidence dependence of average m_{ch}^{TOF} . The m_{ch}^{TOF} is independent of luminosity by requiring TOF matching, which indicates that the background tracks from pileup events are suppressed by TOF from the conventional multiplicity shown in Fig. 3.23. Therefore, the TOF matched multiplicity distributions are consistent among different luminosity groups as shown in Fig. 4.8.

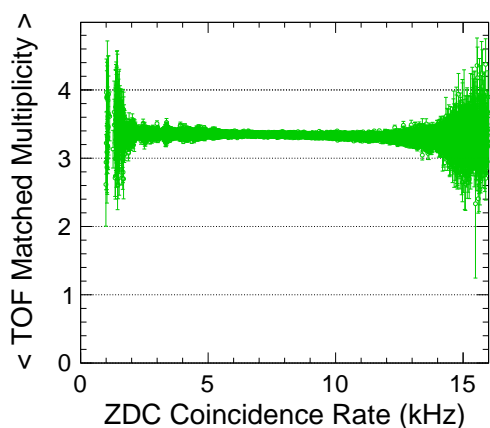


Figure 4.7: The ZDC coincidence rate dependence of the averaged number of TOF matched multiplicity m_{ch}^{TOF} over events.

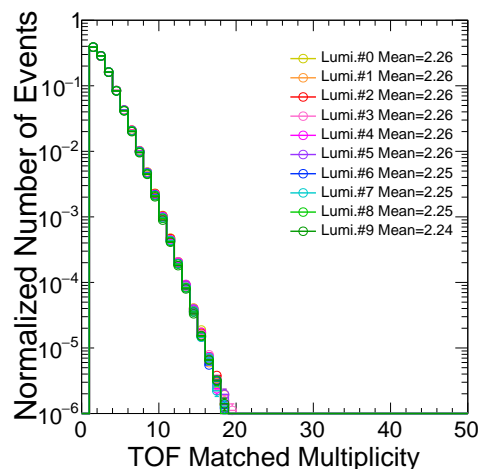


Figure 4.8: Distributions of TOF matched multiplicity m_{ch}^{TOF} measured in different luminosity groups. Mean represents the average value of the TOF matched multiplicity distribution for each luminosity group.

Using this luminosity independent multiplicity, ZDC coincidence rate dependence of net-proton cumulants is calculated as shown in Fig. 4.9. Observed average C_1 over m_{ch}^{TOF} show decreasing trends with increasing of luminosity for both uncorrected and corrected by luminosity dependent efficiencies. The degree of the decreasing for efficiency corrected C_1 are $\sim 10\%$ improved compared to the observed C_1 in Fig. 3.50. The tuning of the efficiencies based on C_1 of (anti)protons is performed as discussed in Sec. 3.5.6. The deviations of the cumulants among different luminosity groups are reduced at higher-order by tuning the efficiencies.

The TOF matched multiplicity dependence of cumulants averaged over luminosity is shown in Fig. 4.10 with Skellam and PYTHIA 8 calculations. The increasing trends of the cumulants are shown in both the observed results and PYTHIA 8. The deviations between the observed cumulants and Skellam are more pronounced in the higher-order results. In the odd-orders, the PYTHIA 8 calculations without CR are closer to the observed cumulants compare to those with CR, while in the even-orders, PYTHIA 8 with CR are closer to the observed cumulants. For the ratios, observed C_2/C_1 are increasing, while the results for other orders are decreasing at $m_{ch}^{\text{TOF}} \leq 3$ as shown in Fig. 4.11. The values of C_2/C_1 and C_3/C_2 are not consistent with PYTHIA 8 calculations for both with and without CR. On the other hand, the decreasing trend with the peak at $m_{ch}^{\text{TOF}} \sim 3$ in higher-order ratios are qualitatively consistent with the PYTHIA 8 calculations. These cumulant results using TOF matched multiplicity are employed for the final results and comparison with Au+Au collisions discussed in Sec. 5.4.

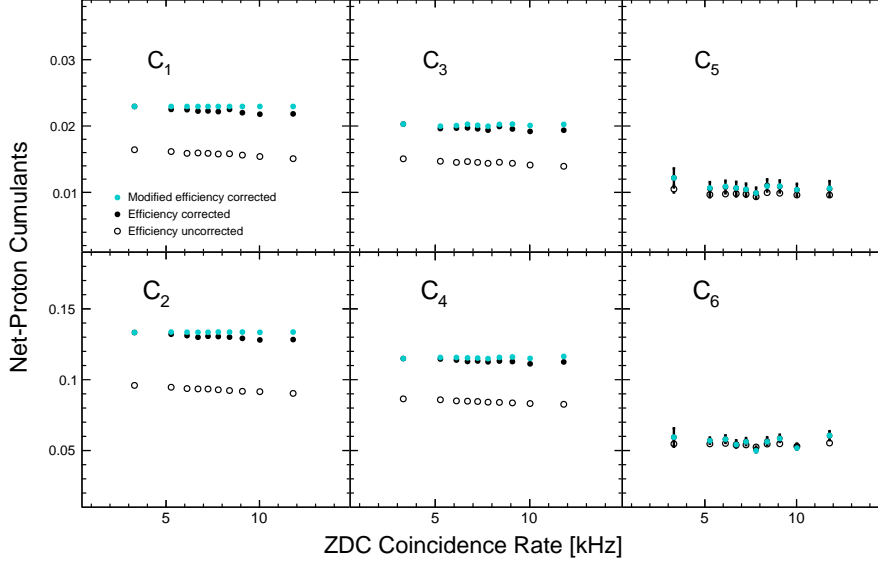


Figure 4.9: ZDC coincidence rate dependence of efficiency corrected cumulants up to the sixth-order. The values are averaged over TOF matched multiplicity.

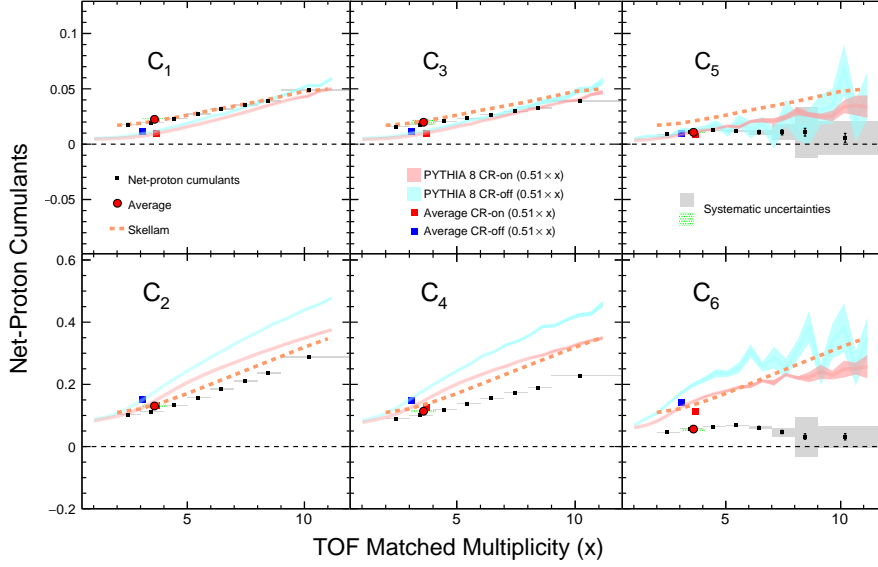


Figure 4.10: TOF matched multiplicity dependence of efficiency corrected cumulants up to the sixth-order. The red and blue bands and squares show bin-by-bin and average PYTHIA 8 calculations, respectively. The most right points represents $9 \leq m_{ch}^{\text{TOF}} < 20$.

The relative systematic uncertainties and R_j of average cumulants over multiplicity are summarized in Tab. 4.1. The σ_{sys} of C_5 are 2.25% smaller than the results using mean corrected multiplicity as shown in Tab. 3.15. Systematic uncertainties for each multiplicity are summarized in Tabs. D.3 and D.4 in App. D.2.3.

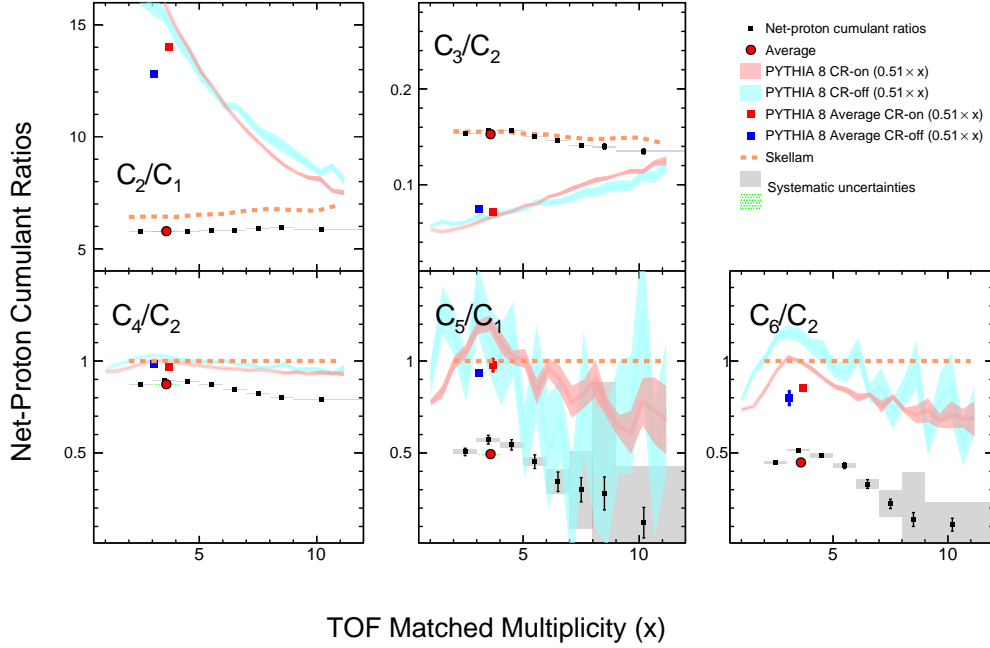


Figure 4.11: TOF matched multiplicity dependence of efficiency corrected cumulant ratios in different luminosity groups. The red and blue bands and squares show bin-by-bin and average PYTHIA 8 calculations, respectively. The most right points represents $9 \leq m_{ch}^{\text{TOF}} < 20$.

Table 4.1: Relative systematic uncertainty and R_j of average cumulants up to sixth-order.

Order	σ_{sys} (%)	$ n\sigma_p $	DCA	nHitsFit	$R_j \times 100$ (%)		
					m^2	Efficiency	ZDC co. rate
C_1	2.00	3.48	11.84	2.93	3.12	5.45	0.32
C_2	0.99	2.58	7.59	2.49	2.58	4.64	0.07
C_3	1.61	3.31	10.56	2.67	2.74	4.87	0.61
C_4	0.72	2.24	6.54	2.12	2.11	3.94	0.41
C_5	0.73	4.53	3.87	0.90	0.58	0.93	5.95
C_6	0.55	2.50	2.11	1.22	1.66	1.63	6.10
C_2/C_1	0.15	1.09	3.62	0.24	0.27	0.46	0.82
C_3/C_2	0.11	1.46	2.81	0.37	0.17	0.21	0.91
C_4/C_2	0.02	0.40	0.82	0.38	0.45	0.61	0.31
C_5/C_1	1.51	4.52	7.48	2.93	2.67	3.85	6.62
C_6/C_2	1.36	3.86	6.55	3.39	4.18	4.59	5.35

Chapter 5

Discussions

5.1 Effects of pions from Λ decay on multiplicity

In this subsection, we discuss the self-correlation effects of daughter (anti)protons from Λ decays on the higher-order fluctuations of the net-proton. To simulate this, the effects of Λ decays are studied by the STAR collaboration [19] with PYTHIA 8 having 20 million CR-off events. Figure 5.1 shows the multiplicity distributions for the two cases: The label of “refmult3A” is the default multiplicity used in data and “refmult3B” is multiplicity removed correlation from Λ decay. In the refmult3B, if a Λ and $\bar{\Lambda}$ decays pion and proton, and the proton is selected in the analysis acceptance, the daughter pion from the same decay is excluded from the multiplicity definition. To observe net-proton cumulants, those secondary proton needs to be removed. As discussed in Sec. 3.1.2, $DCA < 1$ cm cut works to suppress the secondary particle to some extent. The residual secondary particles are acceptable in terms of proxy as net-baryons. The distributions of refmult3A and refmult3B are consistent. The cumulants calculated up to the fourth-order with the two multiplicity distributions are shown in Fig. 5.2. It is found that their values of refmult3A and refmult3B show agreement within the uncertainties. Therefore, the effect of protons due to Λ decay is negligible.

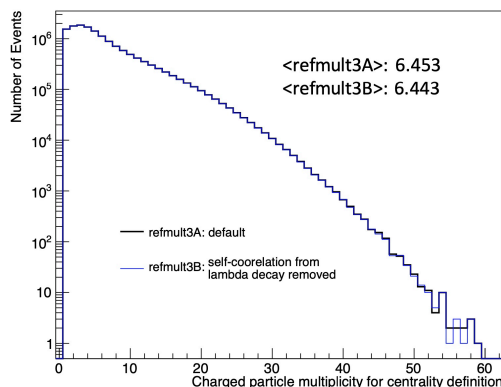


Figure 5.1: Multiplicity distribution of charged particles calculated by PYTHIA 8 [19]. The black line shows the default multiplicity as used in data. The blue line shows the multiplicity with correlation from Λ decay.

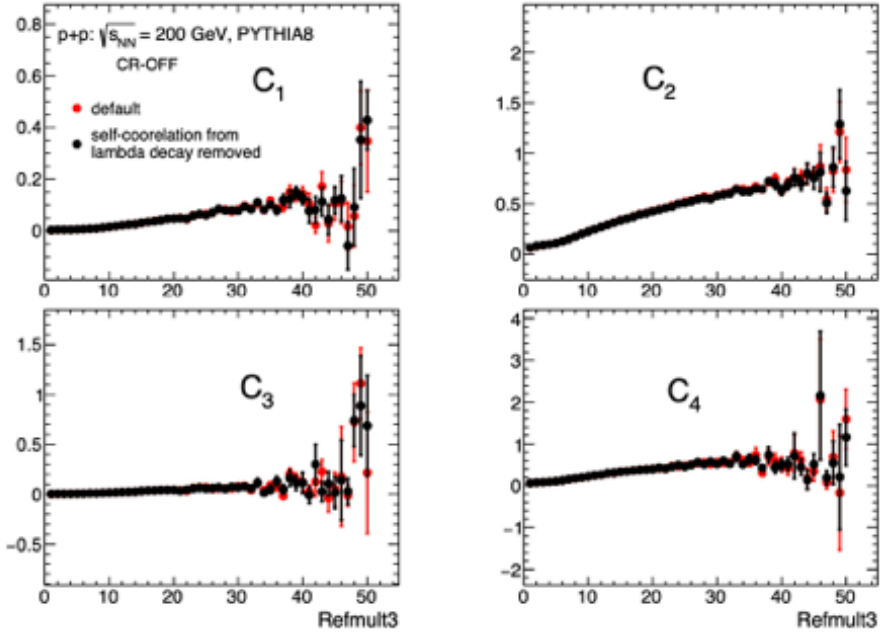


Figure 5.2: The net-proton cumulant ratios with the refmult3A and the case of correlation from λ decay removed from centrality definition.

5.2 Baryon number conservation

To understand the observed acceptance dependence of cumulant ratios, we consider the effects of baryon number conservation [52]. To impose baryon number conservation on a system of (anti)baryon following a Poisson distribution, the finite acceptance is modeled by the binomial distribution [53]. Let us suppose that $N_B^{4\pi}$ baryons are generated in 4π acceptance, and N_B baryons come into the experimental acceptance for fluctuation measurements. In the case of the absence of baryon number conservation, the net-baryon number distribution follows the Skellam distribution. In this model, the baryon number conservation is imposed on both observed and unobserved particles. In the absence of correlations between measured particles and unobserved particles, the distribution of the particles follows a binomial distribution, where the probability p to observe a baryon is given by the fraction of the average observed baryon number $\langle N_B \rangle$ to the average baryon number in the full phase space $\langle N_B^{4\pi} \rangle$. To calculate for net-protons, the acceptance factor p is given by:

$$p = \frac{\langle N_B \rangle}{\langle N_B^{4\pi} \rangle} \rightarrow \frac{\langle N_p \rangle}{\langle N_B^{4\pi} \rangle}, \quad (5.1)$$

where $\langle N_p \rangle$ is the average number of observed protons. For simplicity, the same acceptance factor is assumed for anti-baryons. Based on above assumptions, measured even-order cumulants are written as:

$$C_2 = p(1-p)\langle N \rangle_C, \quad (5.2)$$

$$C_4 = C_2 + 3(p^2q^2B^2 - c_2^2) + 6pq(2(\langle N_B \rangle \langle N_{\bar{B}} \rangle)p(1-p) - C_2), \quad (5.3)$$

$$C_6 = C_4 + 4(C_4 - C_2) - 10(2p(1-p) + C_2)(C_4 - C_2) - 30pq(p^2q^2B^2 + \kappa_2^2), \quad (5.4)$$

where $q = 1 - p$, and $B(= \langle N_{\bar{B}} \rangle - \langle N_B \rangle)$ is an average net-baryon number, and $\langle N \rangle_C = \langle N_B \rangle_C + \langle N_{\bar{B}} \rangle_C$. In the limit $p \rightarrow 0$, where the distribution become close to Skellam, the cumulants are approximated $C_2 \approx C_4 \approx C_6 \approx p\langle N \rangle_C$ in $p \rightarrow 0$. In absence of baryon number conservation, since net-proton number distribution follow the Skellam distribution, cumulants are written as $C_6^S = C_4^S = C_2^S = p\langle N \rangle$. The fraction of C_2 to the Skellam therefore can be obtained by:

$$\frac{C_2}{\text{Skellam}} = 1 - p, \quad (5.5)$$

where the assumption of global baryon number conservation induces correlations between protons and antiprotons. Based on the Eq. 5.5, the observed deviations of C_2 shown in Figs. 4.1 and 4.3 can be discussed with the effect from the baryon number conservation.

The ALICE experiment at LHC has reported the pseudorapidity dependence of the normalized second-order net-proton cumulant [54]. The results for small pseudorapidity ranges of $\Delta\eta < 0.8$ show agreement with Skellam baseline within uncertainties, which is expected the case of limit $p \rightarrow 0$ as discussed above. The values for $\Delta\eta > 0.8$ deviate from Skellam and they show agreement with the prediction assuming global baryon number conservation with $1 - p$. This can be understood that the observed deviations for each acceptance are explained by the assumption of the baryon number conservation effect within the full phase space.

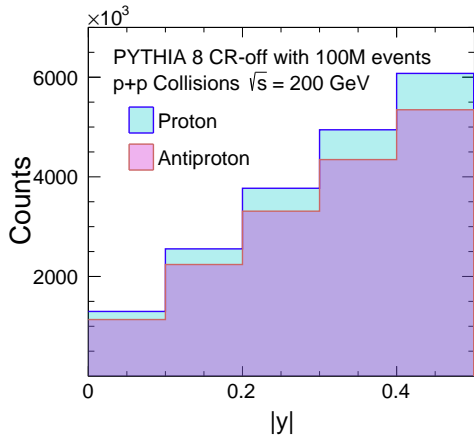


Figure 5.3: $|y|$ distributions of (anti)protons by PYTHIA 8 in $p+p$ collisions at $\sqrt{s} = 200$ GeV with 100 million events in the CR-off configurations.

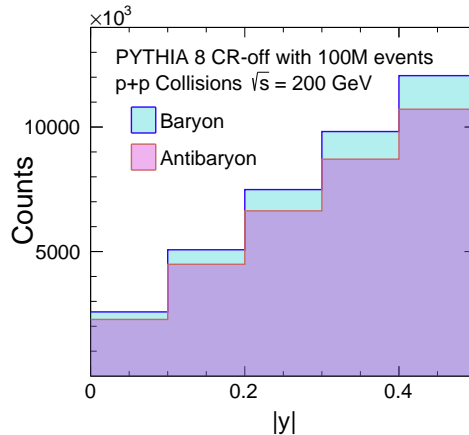


Figure 5.4: $|y|$ distributions of (anti)baryons by PYTHIA 8 in $p+p$ collisions at $\sqrt{s} = 200$ GeV with 100 million events in the CR-off configurations.

Table 5.1: Values of $C_2/\text{Skellam}$, $\langle N_p \rangle$, $\langle N_B^{4\pi} \rangle$, p for each rapidity acceptance calculated by PYTHIA 8 in $p+p$ collisions at $\sqrt{s} = 200$ GeV with 100 million events in the CR-off configurations.

Acceptance	$C_2/\text{Skellam}$	$\langle N_p \rangle$	$\langle N_B^{4\pi} \rangle$	p
$ y < 0.5$	0.86	0.093	1.53	0.061
$ y < 0.4$	0.88	0.075		0.048
$ y < 0.3$	0.90	0.056		0.036
$ y < 0.2$	0.92	0.037		0.024
$ y < 0.1$	0.95	0.018		0.012

In this study, to evaluate the rapidity dependence of net-proton $C_2/\text{Skellam}$, the value of p needs to be obtained by model expectation. PYTHIA 8 calculations having 100 million events with CR-off configuration are used to calculate variables $\langle N_B \rangle$ and $\langle N_B^{4\pi} \rangle$. Figures 5.3 and 5.4 show the $|y|$ distributions for (anti)proton and (anti)baryon, respectively. The number of protons and neutrons are contained in the number of baryons for each rapidity acceptance about half each. For each acceptance, calculated $C_2/\text{Skellam}$, $\langle N_p \rangle$, $\langle N_B^{4\pi} \rangle$, and p for each y acceptance calculated by PYTHIA 8 are shown in Tab. 5.1. The observed $C_2/\text{Skellam}$ as a function of the y acceptance with PYTHIA 8 $C_2/\text{Skellam}$ and $1 - p$ are shown in Fig. 5.5. The value of $C_2/\text{Skellam}$ is below unity and the deviations are increasing with increasing acceptance. The values are fitted by linear and quadratic functions with intercepting 1.0. PYTHIA 8 results show the linearly decreasing with increasing acceptance and they do not reproduce the observed results. The value of $1 - p$ at $|y| < 0.1$ reproduces the observed $C_2/\text{Skellam}$, while they are above data at larger acceptance. The linear fitting function for the data with intercept 1.0 shows a steeper slope than $1 - p$. The quadratic fitting function with 4.8 times better χ^2/NDF compared to the linear fitting is below the line of $1 - p$. This deviation between the data and $1 - p$ can provide an

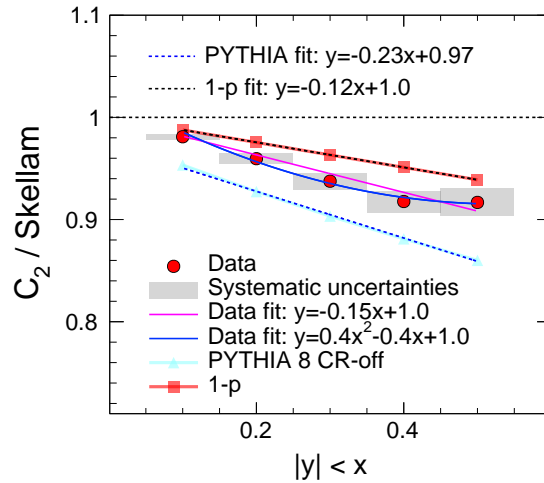


Figure 5.5: Data and PYTHIA 8 calculation of y dependence of $C_2/\text{Skellam}$ in $p+p$ collisions at $\sqrt{s} = 200$ GeV for $0.4 < p_T < 2.0$ GeV/ c and $|y| < 0.1 - 0.5$. The red points are observed average values over multiplicity. The solid magenta and blue lines are fitting of the data with linear and quadratic functions, respectively. The red and light blue bands show $C_2/\text{Skellam}$ and $1 - p$ calculated by PYTHIA 8. The blue and black solid lines are fitting for $C_2/\text{Skellam}$ and $1 - p$ calculated by PYTHIA 8, respectively. The statistical uncertainties are smaller than the size of the markers and bands. The shaded gray bands show the systematic uncertainties.

explanation that the observed fluctuations can contain the effects that are not explained only the baryon number conservation effects.

5.3 Pileup model

The pileup events are included in the cumulant calculations. In this subsection, we tried to understand the effect of pileup events by modeling a “pileup-filter” based on the data. In this model, two(three) events are randomly picked up from each sub-group with the probability $\alpha(\beta)$, and they are superimposed in terms of the (anti)protons and multiplicity. The probability distribution function to find N particles is given by:

$$P(N) = (1 - \alpha)P^t(N) + \alpha P^{\text{pu}2}(N) + \beta P^{\text{pu}3}(N), \quad (5.6)$$

where the $P^t(N)$ and $P^{\text{pu}n}(N)$ are the probabilities for the observed multiplicity distribution in the lowest luminosity group (true) and the superposition of n single-collisions events, respectively. To describe the multiplicity distributions for the highest luminosity using the lowest one, the latter event samples are divided into two sub-groups named “ $P_{\#0}^t(N)$ ” and “ $P_{\#9}^t(N)$ ” having 10 million events, where subscripts $\#n$ indicate luminosity group numbers. By varying the parameters α and β , we can determine the “pileup filter” which describes the multiplicity distributions in higher luminosity groups. Figure 5.6 shows the distributions for $P_{\#0}^t(N)$ and $P_{\#9}^t(N)$, and results of $\alpha P_{\#0}^{\text{pu}2}(N) + \beta P_{\#0}^{\text{pu}3}(N)$ with $\alpha=0.89$ and $\beta=0.11$.

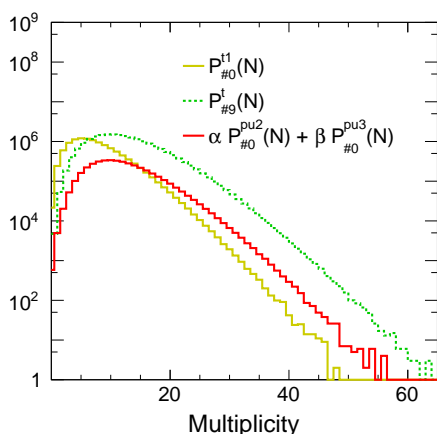


Figure 5.6: Multiplicity distributions for experimental data and demonstration of pileup filter. The yellow and green data show the distribution measured in luminosity groups $\#0$ and $\#9$, respectively. The red data is reproduced distribution from the yellow data.

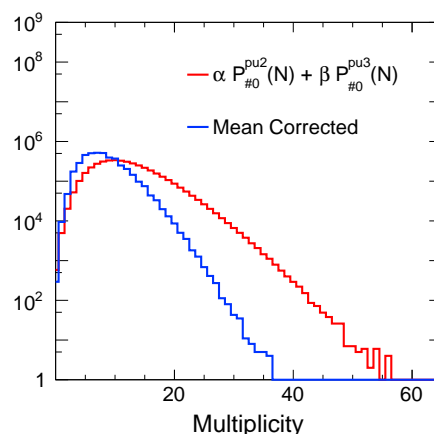


Figure 5.7: Multiplicity distributions for experimental data and demonstration of pileup filter. The red and blue data correspond to pileup filtered distribution $\alpha P_{\#0}^{\text{pu}2}(N) + \beta P_{\#0}^{\text{pu}3}(N)$ and mean corrected distribution, respectively.

To evaluate the pileup effects on fluctuations, the cumulants are calculated with distributions $P_{\#0}^t(N)$ and $\alpha P_{\#0}^{\text{pu}2}(N) + \beta P_{\#0}^{\text{pu}3}(N)$. Note that the filter is not applied to the number of (anti)protons. Once the pileup filter is applied to the number of p/pbar as performed for the multiplicity, the value of C_1 is doubled by the construction, but such a significant difference is not observed in the data as shown in Fig. 5.8. Therefore, the number of protons and antiprotons are randomly picked up from $P_{\#0}^t(N)$ and $P_{\#0}^t(N)$ with 50% probability for each. The results of cumulants in $\alpha P_{\#0}^{\text{pu}2}(N) + \beta P_{\#0}^{\text{pu}3}(N)$ are shown in Fig. 5.9. It is found that the C_1 values of $\alpha P_{\#0}^{\text{pu}2}(N) + \beta P_{\#0}^{\text{pu}3}(N)$ are consistent with that of $P_{\#0}^t(N)$ within $\sim 1\sigma$ uncertainties. On the other hand, the C_2 of $\alpha P_{\#0}^{\text{pu}2}(N) + \beta P_{\#0}^{\text{pu}3}(N)$ become smaller than that of $P_{\#0}^t(N)$ shown at $m_{ch} < 10$. Furthermore, larger deviations between the lowest and highest luminosity are seen at C_2 than the other orders. These characteristic multiplicity dependencies are qualitatively consistent with the results measured in real high luminosity data as shown in Fig. 5.8. For the higher-order results, C_4 and C_6 show a similar trend with C_2 within large uncertainties. As discussed in Sec. 3.5.4, the mean correction of multiplicity distribution is performed as shown in Fig. 5.7. As a results of mean correction, cumulants for $\alpha P_{\#0}^{\text{pu}2}(N) + \beta P_{\#0}^{\text{pu}3}(N)$ show agreement with that for $P_{\#0}^t(N)$ within the uncertainties as

shown in Fig. 5.10. The agreement of cumulants by mean correction is consistent with the experimental results as shown in Fig. 5.11. Therefore, the pileup effect on cumulants can be demonstrated by this simulation up to C_2 through the pileup filter.

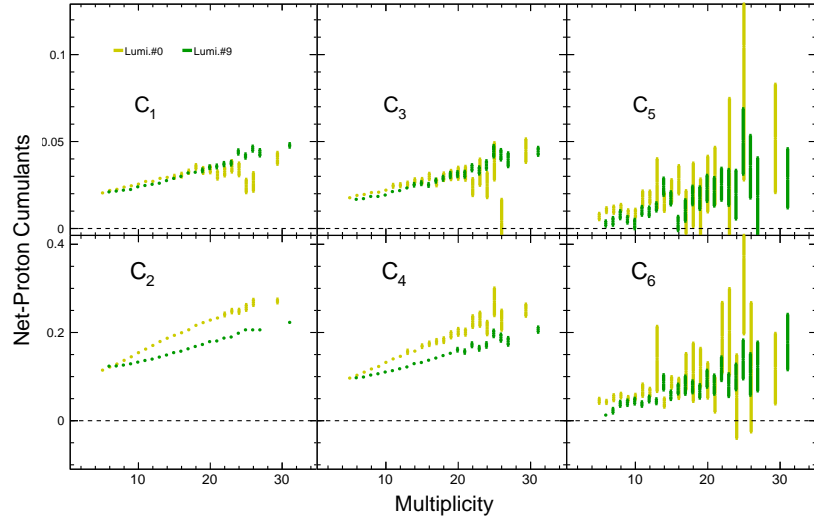


Figure 5.8: Multiplicity dependence of cumulants up to the sixth-order measured in the lowest and highest luminosity groups.

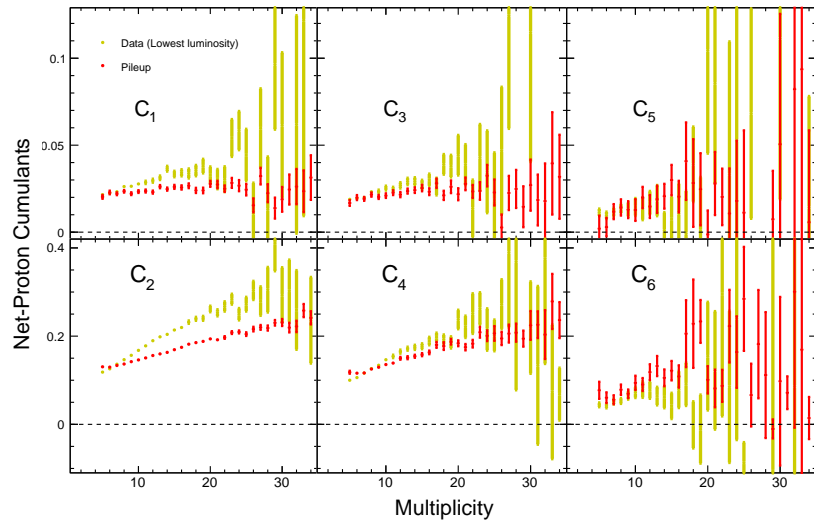


Figure 5.9: Multiplicity dependence of cumulants measured in lowest luminosity and calculated through the pileup filter.

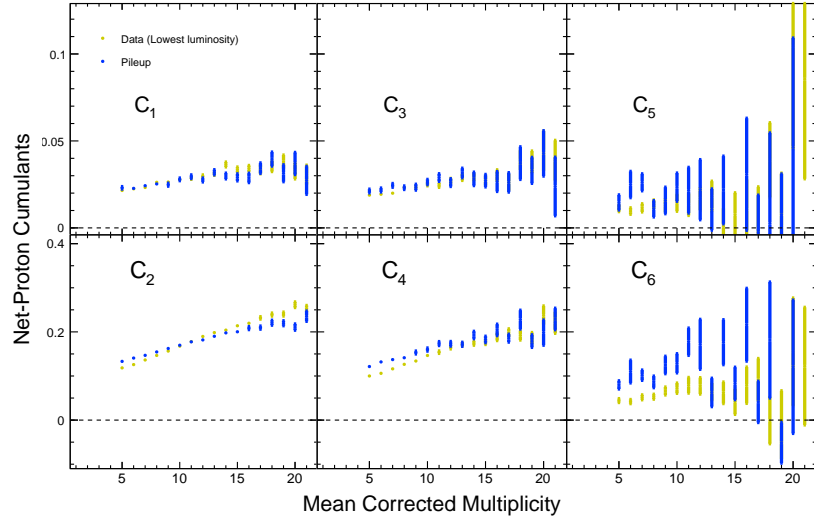


Figure 5.10: Mean corrected multiplicity dependence of cumulants measured in the lowest luminosity and calculated through the pileup filter.

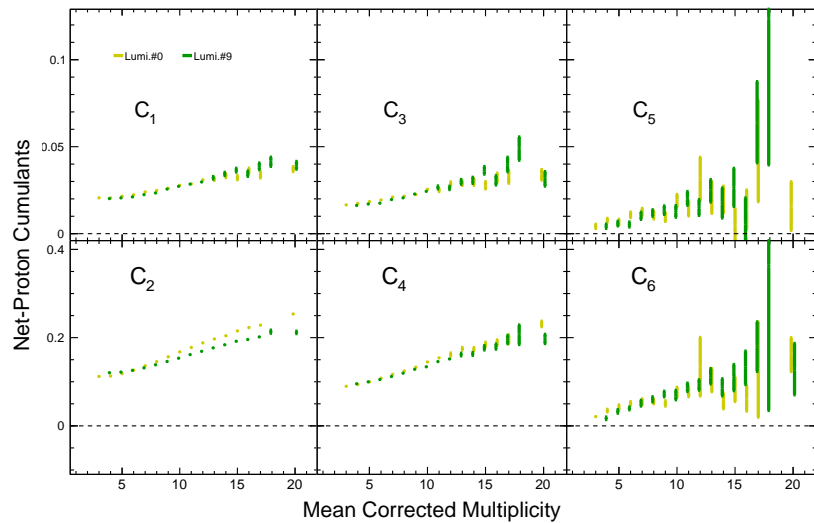


Figure 5.11: Mean corrected multiplicity dependence of cumulants up to the sixth-order measured in the lowest and highest luminosity groups.

5.4 Comparison with Au+Au collision

Figure 5.12 shows the multiplicity dependence for cumulant ratios C_4/C_2 , C_5/C_1 , and C_6/C_2 , where the results from Au+Au collisions at $\sqrt{s_{NN}} = 200$ GeV are overlaid on top of the results from $p+p$ collisions. The values of multiplicity for $p+p$ collisions are converted from the TOF matched multiplicity in Fig. 4.11 to the TPC multiplicity using Fig. 5.13. Results from the hadron resonance gas model (HRG) [55], PYTHIA 8 [19], Lattice QCD [31], and the Skellam expectations are also shown. The HRG model can describe the observed particle generated in heavy-ion collisions based on non-interacting hadron and the resonance for the degree of freedom. The HRG results provide a baseline for net-baryon number fluctuations. The details are described in App. C.1. The light blue ticks represent the multiplicity ranges corresponding to the centrality classes in Au+Au collisions. The average values show the following relation: $C_4/C_2 > C_5/C_1 > C_6/C_2$, which is qualitatively consistent with the hierarchy observed in Lattice QCD calculations [6, 31]. The PYTHIA 8 expectations of average values are closer to the values of $p+p$ than the results of Au+Au central collisions. Positive signs of C_5/C_1 and C_6/C_2 are observed for $p+p$ collisions at low multiplicity region, while they decrease and show small value at high multiplicity. It seems that the multiplicity dependence in $p+p$ collisions and the multiplicity dependence of Au+Au shown in the triangular marker are connected. On the other hand, Au+Au results show negative signs at central collisions. The observed negative sign is qualitatively consistent with Lattice QCD calculations. The Lattice calculations imply chiral phase transition in the thermalized QCD matter.

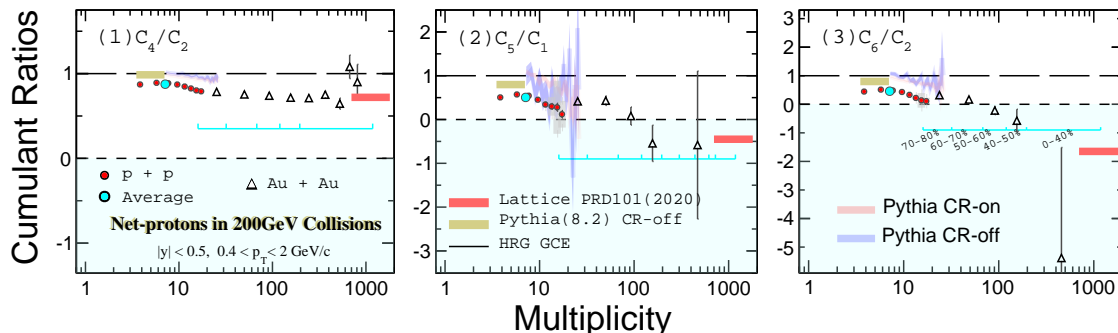


Figure 5.12: Charged multiplicity dependence of the net-proton cumulant ratios, C_4/C_2 , C_5/C_1 and C_6/C_2 , from $\sqrt{s} = 200$ GeV $p+p$ and Au+Au collisions are shown as circles and triangles, respectively. The multiplicity ranges corresponding to the centrality classes in Au+Au collisions are also indicated in the plots. In $p+p$ collisions, the bars and bands are statistical and systematic uncertainties. The red, gold bands, and long-dashed lines indicate the calculations of Lattice QCD, PYTHIA 8, and Hadron Resonance Gas (HRG) models. In the PYTHIA 8, the option of color reconnection is off.

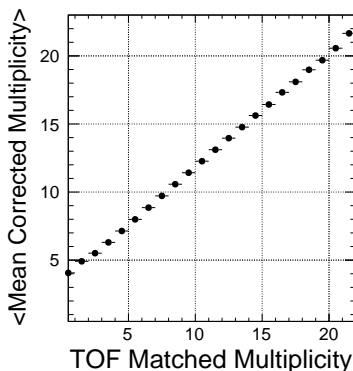


Figure 5.13: The relationship between TOF matched multiplicity and average values of mean corrected multiplicity.

We conclude that our measurements could indicate that the scenario applies to Au+Au central col-

lisions at $\sqrt{s_{\text{NN}}} = 200$ GeV, while not to $p+p$ collisions at low multiplicity and average results over multiplicity. However, results in $p+p$ collisions show decreasing trends and significantly small values at high multiplicity.

Chapter 6

Summary

Understanding the phase structure of the QCD matter and the nature of the phase transitions is one of the ultimate goals of high-energy physics. Higher-order cumulants of conserved charges are powerful tools to study the QCD phase structure. Several hints on the crossover transition and the QCD critical point have been obtained through the measurements for Au+Au collisions in the BES program at RHIC-STAR. In this study, higher-order cumulants of net-proton multiplicity distributions have been measured for $p+p$ 200 GeV collisions to determine the precise baselines to be compared to the results from Au+Au collisions. Through this measurement, we can also test the possibility that the QGP could be formed in high-multiplicity events in $p+p$ collisions.

The most difficult issue in $p+p$ collisions was significant fractions of backgrounds from pileup events, which is generally negligible in Au+Au collisions. To understand the effects of pileup events on higher-order cumulants, several variables on particle multiplicity and detector efficiencies were studied as a function of the luminosity. Luminosity dependent corrections on those variables were then newly developed to handle the effects on higher-order cumulants.

The multiplicity dependence of cumulants has been measured in two ways. We first apply corrections to the conventional particles multiplicity to take care of the effects from pileup backgrounds, then cumulants were measured as a function of the corrected multiplicity. The other way is that we defined a new luminosity-independent quantity. Most orders of cumulant ratios in the former way show increasing with multiplicity increasing, while C_4/C_2 , C_5/C_1 , and C_6/C_2 in the latter way show decreasing with increasing of the particle multiplicity, which is qualitatively consistent with the PYTHIA 8 calculations. Given the consistent shape of the particle multiplicity distributions and cumulant values among different levels of pileup fractions, we finally employed the latter way to measure the multiplicity dependence of cumulants.

The rapidity and transverse momentum acceptance dependence of net-proton cumulants has been also measured with proper weights for each particle multiplicity bin. It is found that the deviations from statistical baselines increase with increasing the rapidity and transverse momentum acceptance. To understand the deviations with the assumption of baryon number conservation within full phase space, the y acceptance dependence of observed C_2 /Skellam and PYTHIA 8 C_2 /Skellam are studied. The observed C_2 /Skellam are below unity and the deviations are increasing with increasing y acceptance. PYTHIA 8 results show the linearly decreasing with increasing acceptance and they do not reproduce the observed results. The value of $1 - p$ at $|y| < 0.1$ overlap with the observed C_2 /Skellam, which is expected by the limit $p \rightarrow 0$, where the observed net-proton distribution become close to Skellam, while they are above data at larger acceptance. Furthermore, the quadratic function performs better fitting the observed results compared to the linear fitting. These results can explain that the observed fluctuations can contain effects that are not explained only by the baryon number conservation effects.

The results of sixth-order cumulant were found to stay positive in multiplicity less than 8, while the values decrease and show the possibility of the negative sign at higher multiplicity region within systematic uncertainties. PYTHIA 8 calculations show decreasing trends and results of C_5/C_1 with CR-off show the possibility of negative value at high multiplicity within uncertainties. The results thus do not reflect the sign of phase transition at low multiplicity, while they can indicate the possibility of phase transition at high multiplicity in $p+p$ collisions. Furthermore, the results from $p+p$ collisions fit into the centrality dependence of Au+Au collisions at the same energy. The measurements provide precise

baselines of net-proton higher-order cumulants for the hadronic matter to be compared to the results from the Au+Au collisions. For Au+Au central collisions, observed results show $C_5/C_1 < 0$ and $C_6/C_2 < 0$, which is understood by Lattice calculations implying chiral phase transition in the thermalized QCD matter. This is not the case in $\sqrt{s} = 200$ GeV $p+p$ collisions for low multiplicity events, while the values show decreasing trends and small values at high multiplicity.

Appendix A

Event and track selection

A.1 Run-by-run QA

Some variables have step-like structures, e.g., Run Index is 100 for $\langle \text{RefMult} \rangle$, due to the change of the trigger, detector, or beam conditions.

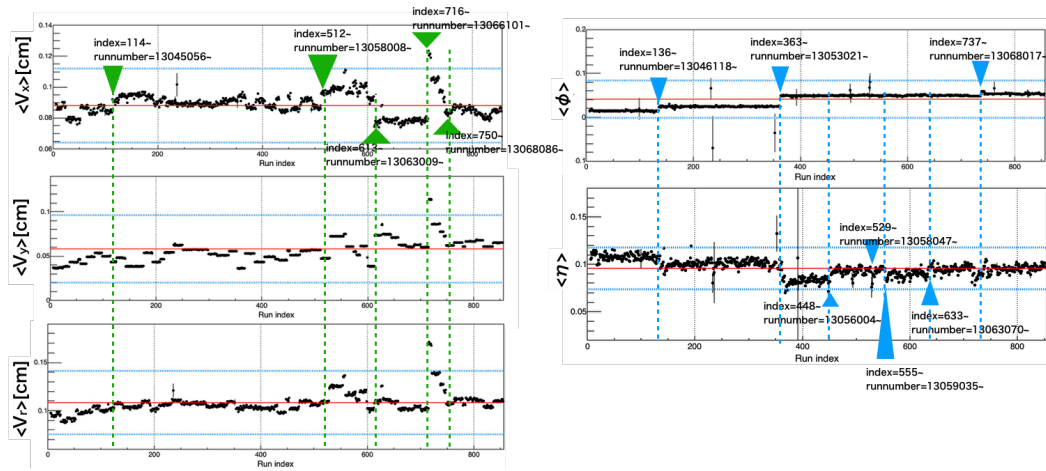


Figure A.1: Run division based on the vertex and phase information.

The criteria of division is based on following run information.

Table A.1: The definition of period for run-by-run QA of event variables (top) and track variables (bottom).

	Run number	Condition
$\langle V_z \rangle$	13045056	TOF and HVIOC issue
	13058008	BEMC and EEMC issue
	13063009	BEMC issue
	13066101	FMS, QT1, QT2, QT3, QT4 issue
	Run number	Condition
$\langle \phi \rangle$	13046118	High FMS trigger, High threshold
	13053021	Orbit correction, High luminosity
	13068017	Removing of FMS trigger
	Run number	Condition
$\langle \eta \rangle$	13056004	beam issue, very high background
	13058047	High TPX rate
	13059035	TOF buch ID errors
	13063070	TPC back on, End of FMS run

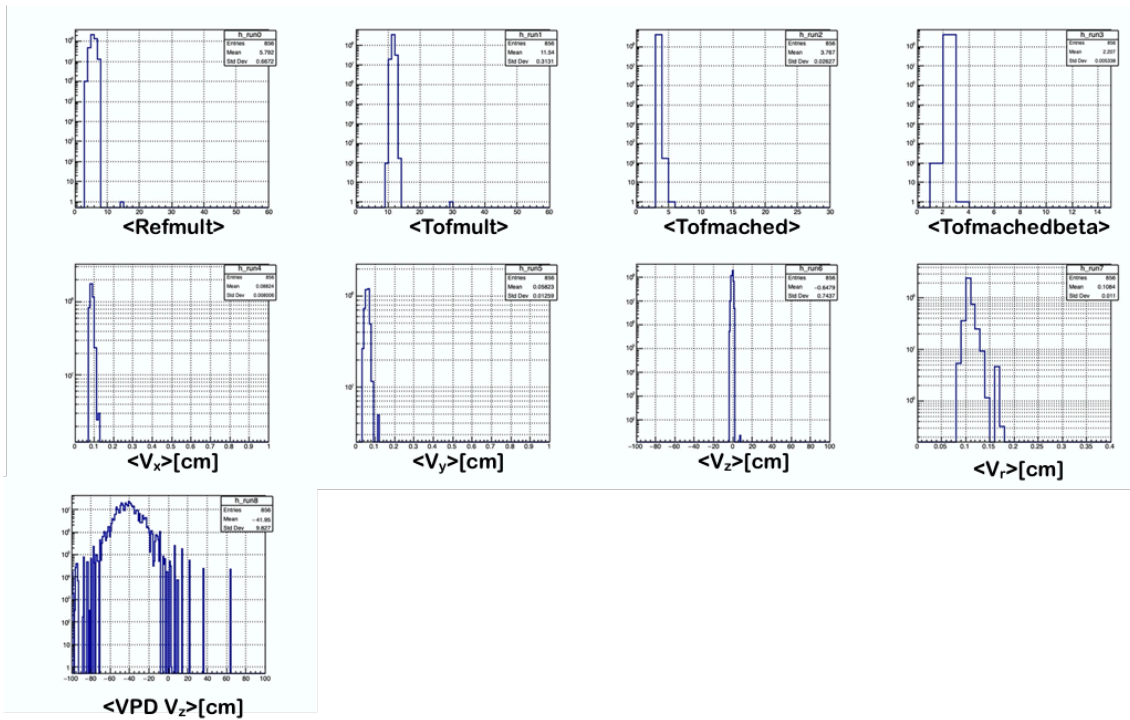


Figure A.2: Histograms for event of the entries defined by the number of run with number of event weight for determination of mean and 3σ range in run-by-run QA.

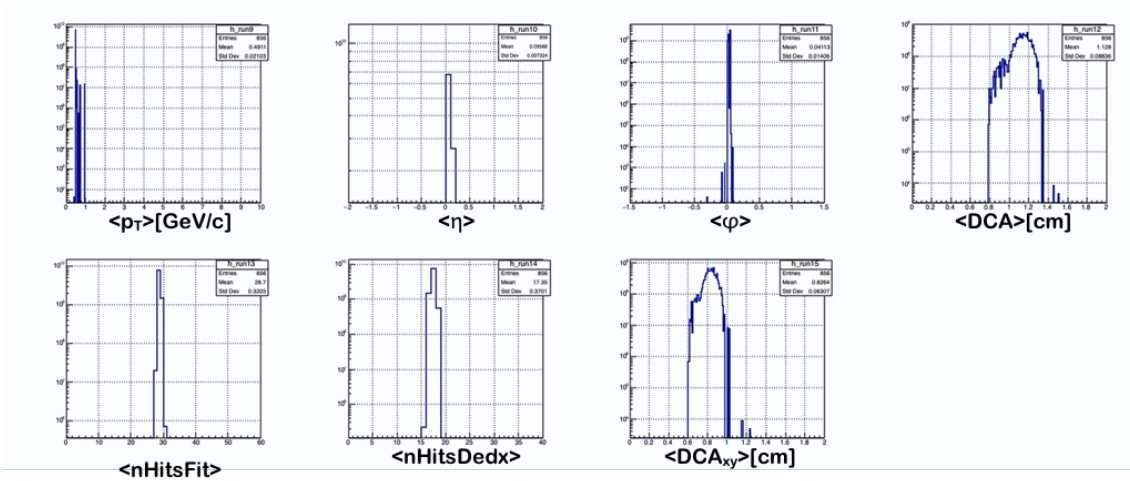


Figure A.3: Histograms for track of the entries which is the number of run with number of event weight for determination of mean and 3σ range in run-by-run QA.

The QA is performed based on the mean value (μ) $\pm 3\sigma$ of averaged variables as a function of run index. Mean and 3σ lines were obtained by the distribution of each variables with event weight.

Table A.2: Definition of badrun in different condition and statistics.

	Total run		
	Number of variables	Number of run	Number of events
	16	856	223234814
Beyond 3σ	Number of variables	Number of badrun	Badrun(%)
	≥ 1 (the tightest)	133	7%
	≥ 2	51	1%
	≥ 3	26	0.1%
	≥ 4	22	0.1%
	≥ 5	18	0.07%
	≥ 6	16	0.001%
	≥ 7	13	0.001%
≥ 8 (the loosest)	13	0.001%	223M
Beyond 2σ	Number of variables	Number of badrun	Badrun(%)
	≥ 1 (the tightest)	353	29%
	≥ 2	203	12%
	≥ 3	131	7%
	≥ 4	94	5%
	≥ 5	69	3.3%
	≥ 6	55	2.5%
	≥ 7	43	1.4%
≥ 8 (the loosest)	32	0.9%	221M

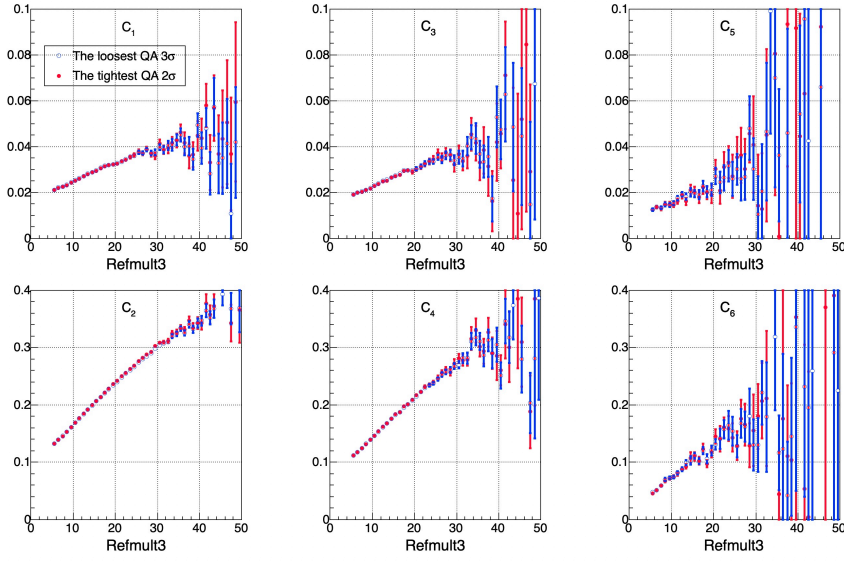


Figure A.4: Comparison of the C_n in the tightest (open red markers) and the loosest (solid blue markers) QA.

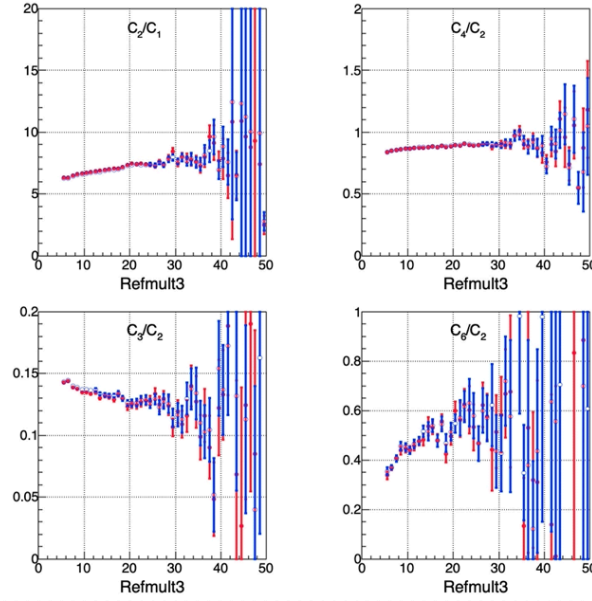


Figure A.5: Comparison of the cumulant ratios in the tightest (open red markers) and the loosest (solid blue markers) QA.

Since the C_n in different 2 level QA are consistent within the statistical uncertainty, the loosest condition of QA can be applied. Totally 13 bad runs were removed.

A.2 Luminosity dependence of event and track variables

Figure A.6 shows the several events and track observables measured in three luminosity region—high, middle, and low. Each distribution is normalized based on the distribution of middle luminosity region. The grouping is defined by Fig. 3.24 in Sec. 3.5.1.

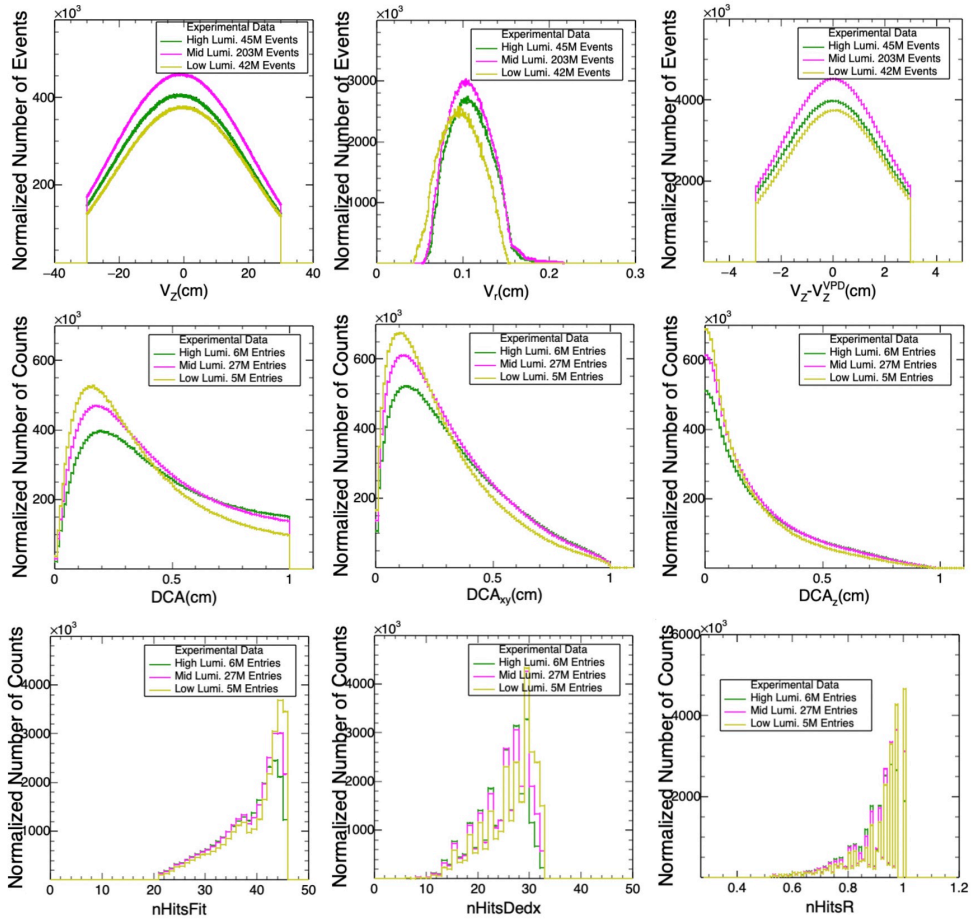


Figure A.6: Luminosity dependence of event and track quality observables— V_z , V_r , $V_z - V_z^{\text{VPD}}$, $|DCA|$, DCA_{xy} , DCA_z , nHitsFit, nHitsDedx, nHitsR— from top left to right bottom panels, where the nHitsR represent the fraction of nHitsFit to number of possible hits on track.

Appendix B

Efficiency

B.1 Mixed cumulants in efficiency correction

$\langle q_{(r,s)} q_{(t,u)} \rangle_c$ are mixed cumulants, which are defined by:

$$\langle m_1^{n_1} m_2^{n_2} \rangle_c = \frac{\partial^{n_1}}{\partial \theta_1^{n_1}} \frac{\partial^{n_2}}{\partial \theta_2^{n_2}} K(\theta_1, \theta_2) \Big|_{\theta_1=\theta_2=0}, \quad (\text{B.1})$$

where $K(\theta_1, \theta_2)$ is cumulant generating function. The calculation of mixed cumulants are written as:

$$\langle m_1 m_2 \rangle_c = \frac{\partial}{\partial \theta_1} \frac{\partial}{\partial \theta_2} \ln G(\theta_1, \theta_2) \Big|_{\theta_1=\theta_2=0} \quad (\text{B.2})$$

$$= \frac{\partial}{\partial \theta_1} \frac{1}{G(\theta_1, \theta_2)} \frac{\partial G(\theta_1, \theta_2)}{\partial \theta_2} \Big|_{\theta_1=\theta_2=0} \quad (\text{B.3})$$

$$= -\frac{1}{G^2(\theta_1, \theta_2)} \frac{\partial G(\theta_1, \theta_2)}{\partial \theta_1} \frac{\partial G(\theta_1, \theta_2)}{\partial \theta_2} + \frac{1}{G^2(\theta_1, \theta_2)} \frac{\partial^2 G(\theta_1, \theta_2)}{\partial \theta_1 \partial \theta_2} \Big|_{\theta_1=\theta_2=0} \quad (\text{B.4})$$

$$= -\langle m_1 \rangle \langle m_2 \rangle + \langle m_1 m_2 \rangle \quad (\text{B.5})$$

$$\langle m_1^2 m_2 \rangle_c = 2\langle m_1 \rangle^2 \langle m_2 \rangle - \langle m_1^2 \rangle \langle m_2 \rangle - 2\langle m_1 \rangle \langle m_1 m_2 \rangle + \langle m_1^2 m_2 \rangle \quad (\text{B.6})$$

$$\langle m_1 m_2^2 \rangle_c = 2\langle m_1 \rangle \langle m_2 \rangle^2 - 2\langle m_2 \rangle \langle m_1 m_2 \rangle - \langle m_1 \rangle \langle m_2^2 \rangle + \langle m_1 m_2^2 \rangle \quad (\text{B.7})$$

$$\langle m_1 m_2 m_3 \rangle_c = \frac{\partial}{\partial \theta_1} \frac{\partial}{\partial \theta_2} \frac{\partial}{\partial \theta_3} \ln G(\theta_1, \theta_2, \theta_3) \Big|_{\theta_1=\theta_2=\theta_3=0} \quad (\text{B.8})$$

$$= \frac{\partial}{\partial \theta_1} \frac{\partial}{\partial \theta_2} \frac{1}{G(\theta_1, \theta_2, \theta_3)} \frac{\partial G(\theta_1, \theta_2, \theta_3)}{\partial \theta_3} \Big|_{\theta_1=\theta_2=\theta_3=0} \quad (\text{B.9})$$

$$= \frac{\partial}{\partial \theta_1} - \frac{1}{G^2} \frac{\partial G}{\partial \theta_2} \frac{\partial G}{\partial \theta_3} + \frac{1}{G^2} \frac{\partial^2 G}{\partial \theta_2 \partial \theta_3} \Big|_{\theta_1=\theta_2=\theta_3=0} \quad (\text{B.10})$$

$$= 2\langle m_1 \rangle \langle m_2 \rangle \langle m_3 \rangle - \langle m_1 m_2 \rangle \langle m_3 \rangle - \langle m_2 \rangle \langle m_1 m_2 \rangle - \langle m_1 \rangle \langle m_2 m_3 \rangle + \langle m_1 m_2 m_3 \rangle \quad (\text{B.11})$$

$$\langle m_1^2 m_2 m_3 \rangle_c = \frac{\partial^2}{\partial \theta_1^2} \frac{\partial}{\partial \theta_2} \frac{\partial}{\partial \theta_3} \ln G(\theta_1, \theta_2, \theta_3) \Big|_{\theta_1=\theta_2=\theta_3=0} \quad (\text{B.12})$$

$$= -6\langle m_1 \rangle^2 \langle m_2 \rangle \langle m_3 \rangle + 2\langle m_1^2 m_2 \rangle \langle m_3 \rangle + 4\langle m_1 \rangle \langle m_1 m_2 \rangle \langle m_3 \rangle + 4\langle m_1 \rangle \langle m_2 \rangle \langle m_1 m_3 \rangle \quad (\text{B.13})$$

$$- \langle m_1^2 m_2 \rangle \langle m_3 \rangle - 2\langle m_1 m_2 \rangle \langle m_1 m_3 \rangle - \langle m_2 \rangle \langle m_1^2 m_3 \rangle \quad (\text{B.14})$$

$$+ 2\langle m_1 \rangle^2 \langle m_2 m_3 \rangle - \langle m_1^2 \rangle \langle m_2 m_3 \rangle - 2\langle m_1 \rangle \langle m_1 m_2 m_3 \rangle + \langle m_1^2 m_2 m_3 \rangle \quad (\text{B.15})$$

B.2 Multiplicity dependence of TOF matching efficiencies

Figure B.1 shows the p_T dependence of efficiencies of the TPC, TOF with the EMC, and combination of them for protons at the entire multiplicity region. It is found that the TOF matching efficiencies with the EMC are 80% and combined show around 70% which is 20% higher than in Fig. 3.17 and 3.18. Multiplicity dependence of the p_T integrated efficiencies are shown in Fig. B.2.

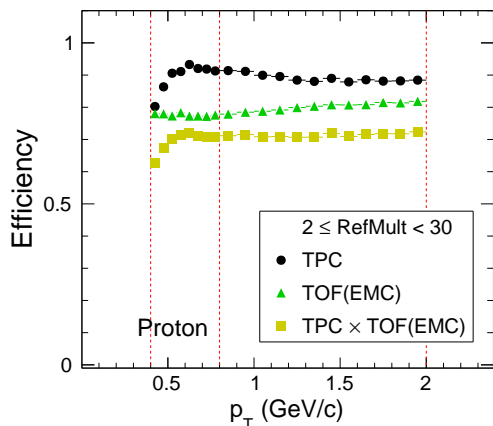


Figure B.1: Transverse momentum p_T dependence of efficiencies of the TPC, TOF with the EMC, and combination of them for protons at merged multiplicity over 2 to 30. Black dots show the TPC tracking efficiency. Green triangles show the TOF matching efficiency with the EMC hit requirement. Yellow squares show combined efficiencies of them. Red dotted lines represent $p_T = 0.4, 0.8, 2.0$ GeV/ c .

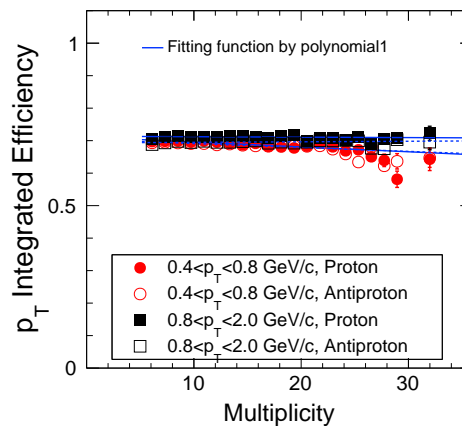


Figure B.2: Multiplicity dependence of p_T integrated efficiencies for the combination of the TPC and TOF with the EMC for protons and antiprotons. Black dots and red squares are shown region $0.4 < p_T < 0.8$ GeV/ c and $0.8 < p_T < 2.0$ GeV/ c , respectively. Solid (open) markers are protons (antiprotons). Blue solid (dotted) lines represent the linear function of fitting for protons (antiprotons).

B.3 Multiplicity and luminosity dependence of efficiencies

Table B.1: TOF matching efficiencies in different luminosity groups for proton and anti-proton.

Lumi.No.	proton		antiproton	
	$0.4 < p_T < 0.8$ GeV/ c	$0.8 < p_T < 2.0$ GeV/ c	$0.4 < p_T < 0.8$ GeV/ c	$0.8 < p_T < 2.0$ GeV/ c
0	0.815	0.795	0.811	0.800
1	0.809	0.792	0.807	0.796
2	0.801	0.792	0.808	0.796
3	0.805	0.790	0.805	0.796
4	0.804	0.791	0.805	0.793
5	0.803	0.790	0.804	0.794
6	0.799	0.788	0.803	0.793
7	0.804	0.786	0.801	0.792
8	0.797	0.787	0.801	0.791
9	0.795	0.785	0.800	0.789

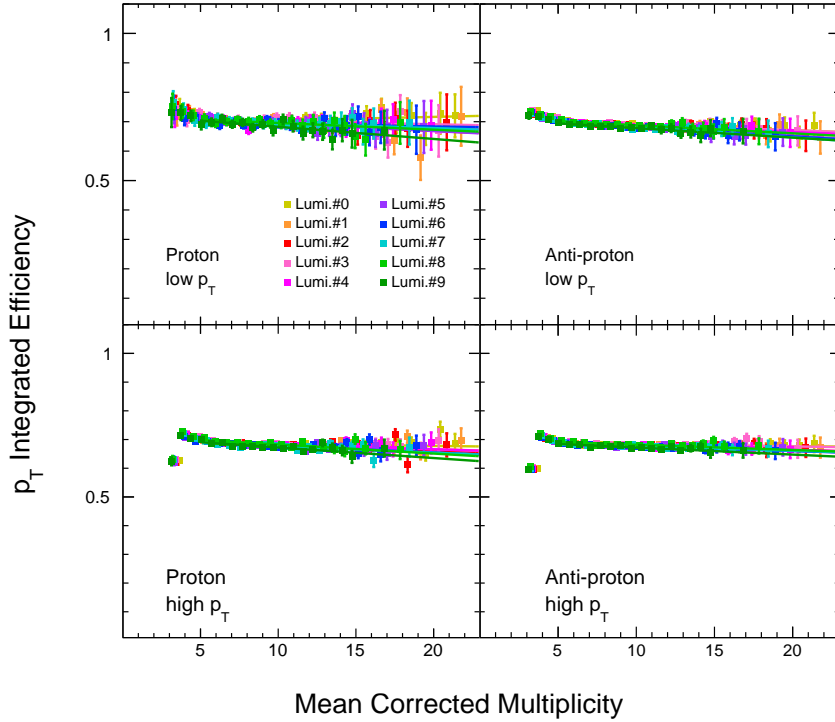


Figure B.3: Mean corrected multiplicity dependence of efficiencies measured in different luminosity groups for proton and antiproton at low and high p_T in $\sqrt{s} = 200$ GeV $p+p$ collisions. The solid lines are fitting by linear function.

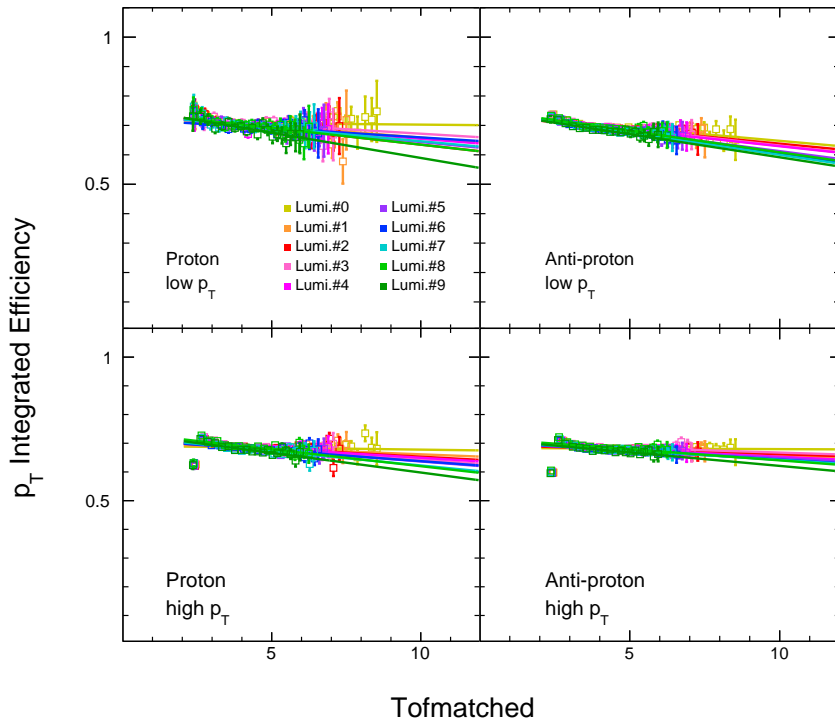


Figure B.4: Tofmatched dependence of efficiencies in different luminosity groups for proton and antiproton at low and high p_T in $\sqrt{s} = 200$ GeV $p+p$ collisions. The solid lines are fitting by linear function.

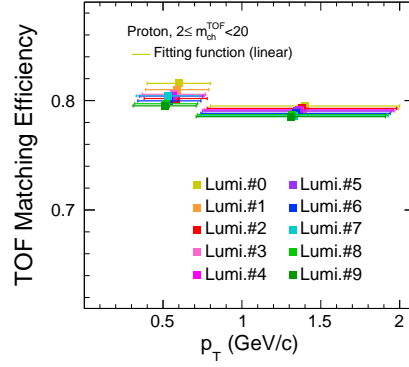


Figure B.5: TOF matching efficiencies as a function of p_T in different luminosity groups for proton. The TOF matched multiplicity range $2 \leq m_{ch}^{TOF} < 20$ are shown.

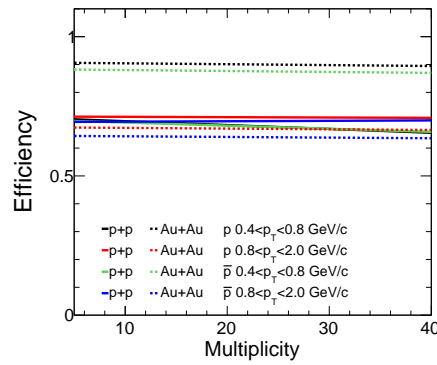


Figure B.6: Multiplicity dependence of efficiencies for $p+p$ and Au+Au collisions.

Appendix C

Theoretical model

C.1 Hadron resonance gas (HRG) model

The baryon number susceptibility with Boltzmann approximation are written by:

$$\chi_{2n}^B = \frac{\partial^{2n}(P/T^4)}{\partial \hat{\mu}_B^{2n-1}} = \sum_{iB} (g_i \frac{m_i}{T})^2 K_2 \frac{m_i}{T} \times \cosh(\hat{\mu}_B + Q_i \hat{\mu}_Q + S_i \hat{\mu}_S) \quad (\text{C.1})$$

, where m_i is hadron mass, g_i is the degeneracy factor for m_i , $\hat{\mu}_B$ is μ_B/T with q= B, Q, S representing baryon, electric charge and strangeness, respectively. This leads the ratios of the baryon number susceptibility as:

$$\frac{\chi_{\text{even}}^B}{\chi_{\text{even}}^B} = 1 \quad (\text{C.2})$$

$$\frac{\chi_{\text{odd}}^B}{\chi_{\text{odd}}^B} = 1 \quad (\text{C.3})$$

$$\frac{\chi_{\text{odd}}^B}{\chi_{\text{even}}^B} = \tanh(\mu_B/T)|_{\mu_Q+\mu_S=0} \quad (\text{C.4})$$

$$\quad (\text{C.5})$$

, where the μ_B is the baryon chemical potential and T is temperature. From Eq. C.5, the relationship between M , σ , and κ are written as:

$$\frac{M_B}{\sigma_B^2} = S_q \sigma_q = \tanh(\mu_B/T)|_{\mu_Q+\mu_S=0} \quad (\text{C.6})$$

$$\kappa_B \sigma_B^2 \quad (\text{C.7})$$

C.2 Multiplicity distribution of PYTHIA 8

For comparison between the measured multiplicity dependence of cumulants in Fig. 4.6 and PYTHIA 8 calculations, the mean of the multiplicity distributions of PYTHIA 8 are tuned. Figure C.1 shows the multiplicity distributions for measured in the luminosity group #0 and PYTHIA 8.

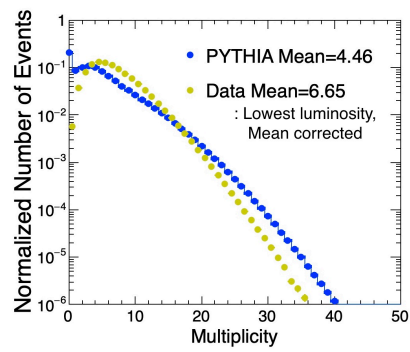


Figure C.1: Multiplicity distributions of experimental data and PYTHIA 8. The blue data shows the PYTHIA 8 with color reconnection. The yellow data represents the measured data of luminosity groups #0 with mean correction.

Appendix D

Analysis

D.1 Number of bins in net-proton distributions

The number of bins in net-proton distributions are investigated for each TOF matched multiplicity and each luminosity groups as shown in Figs. D.1-D.10.

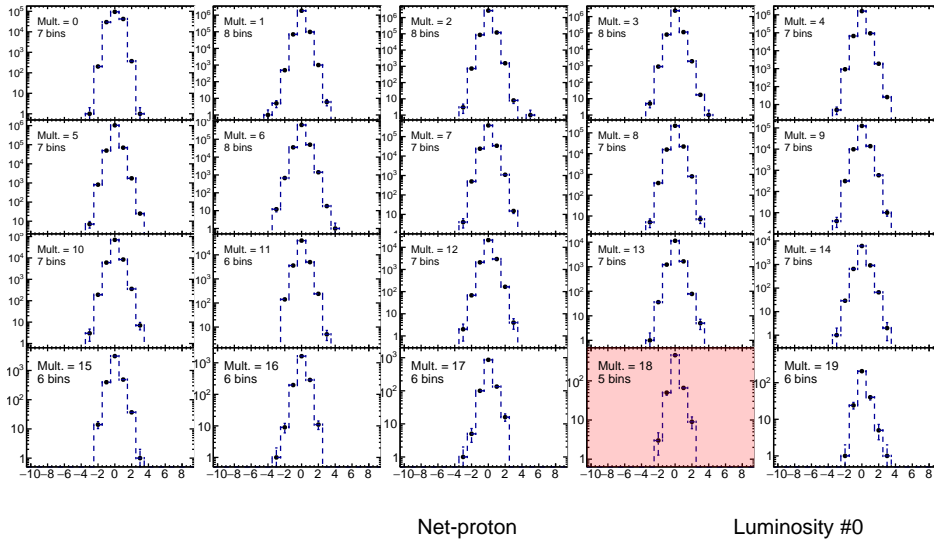


Figure D.1: Net-proton distributions for each Tofmatched in luminosity group #0.

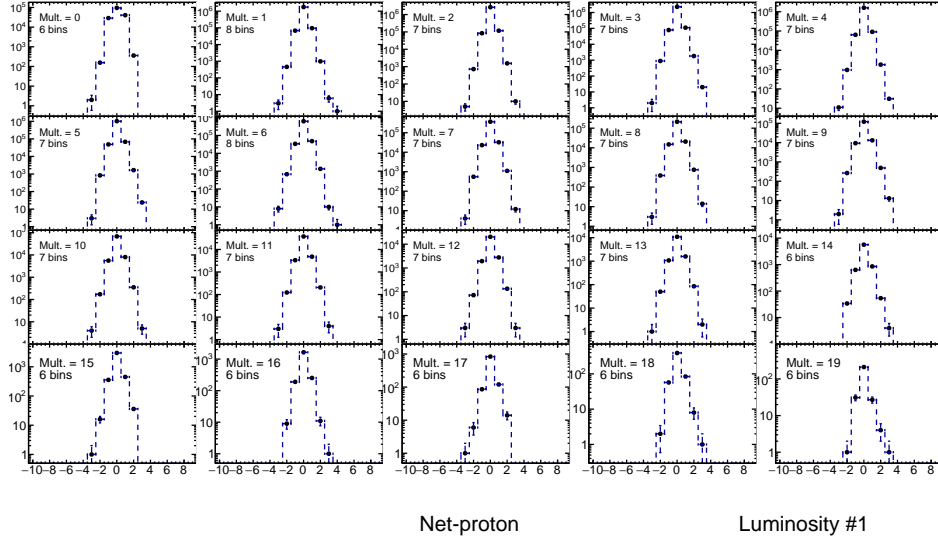


Figure D.2: Net-proton distributions for each Tofmatched in luminosity group #1.

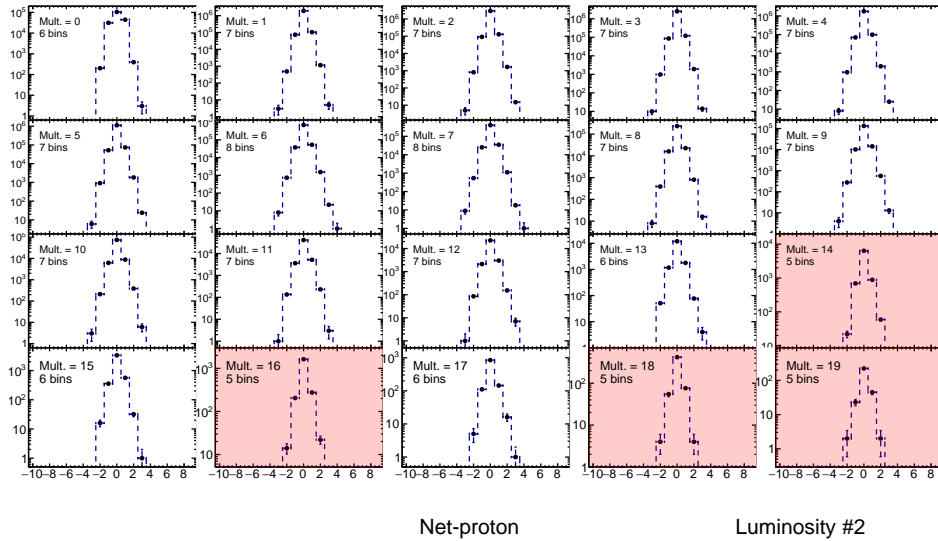


Figure D.3: Net-proton distributions for each Tofmatched in luminosity group #2.

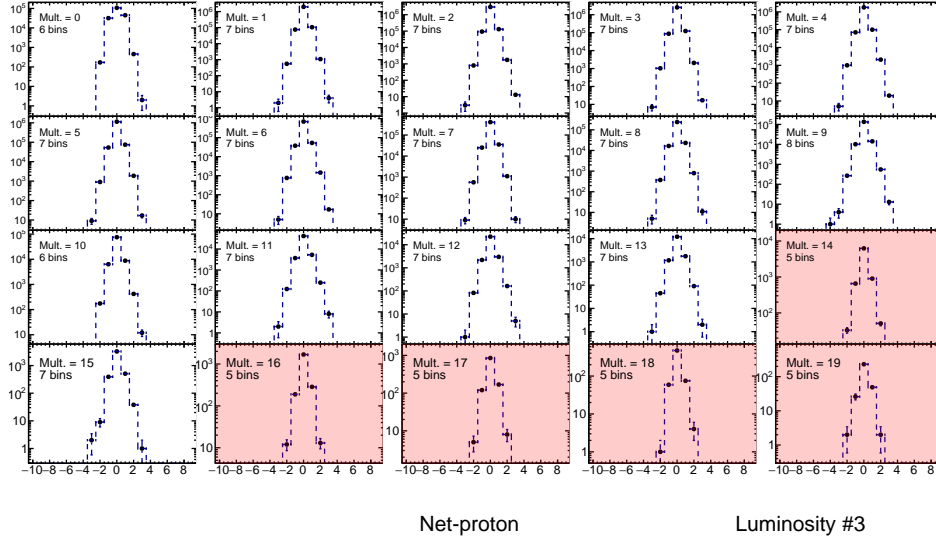


Figure D.4: Net-proton distributions for each Tofmatched in luminosity group #3.

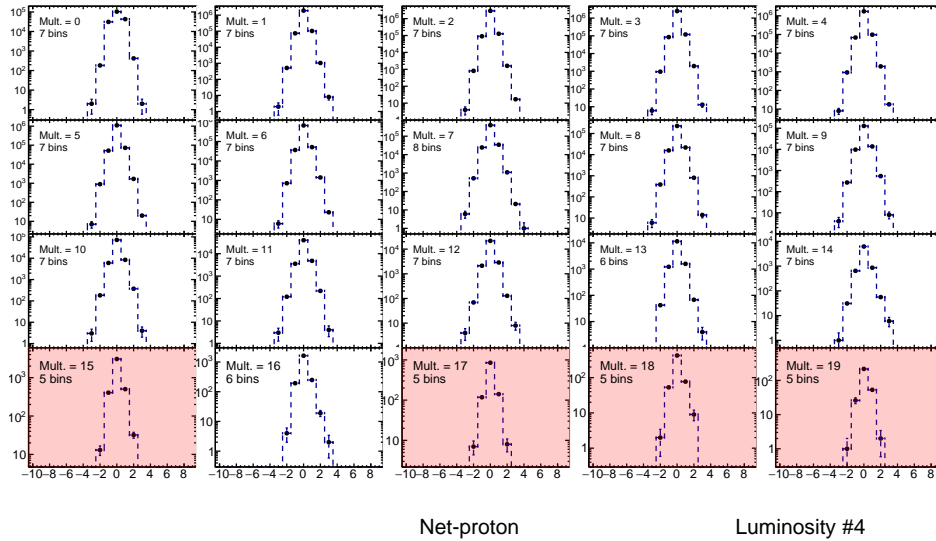


Figure D.5: Net-proton distributions for each Tofmatched in luminosity group #4.

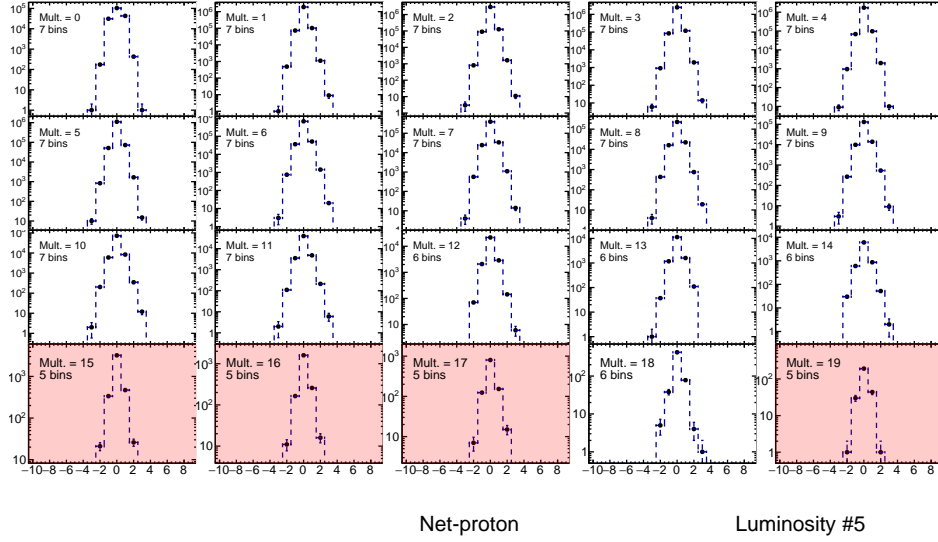


Figure D.6: Net-proton distributions for each Tofmatched in luminosity group #5.

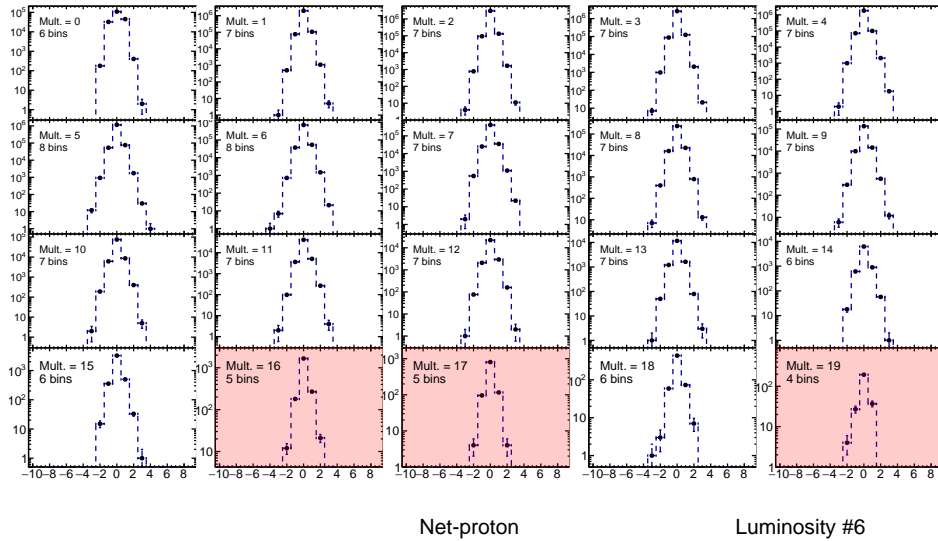


Figure D.7: Net-proton distributions for each Tofmatched in luminosity group #6.

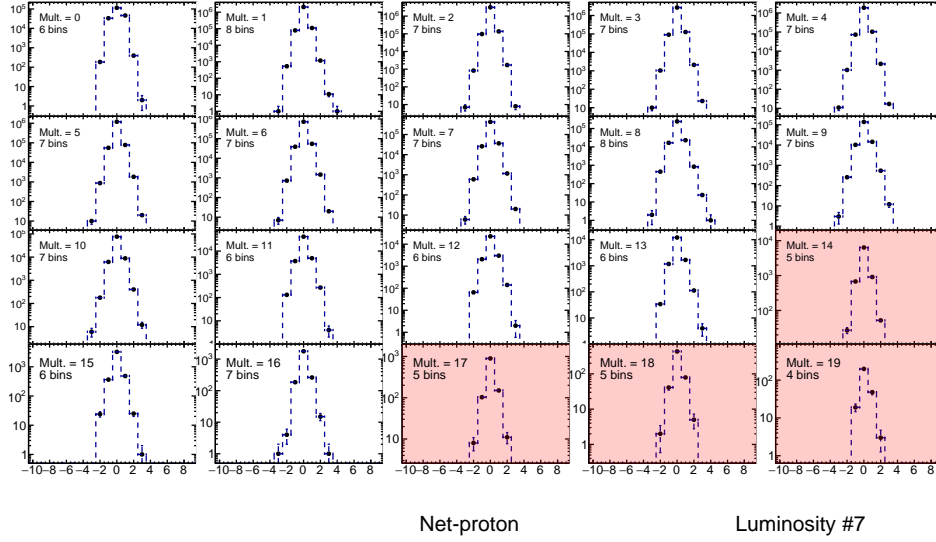


Figure D.8: Net-proton distributions for each Tofmatched in luminosity group #7.

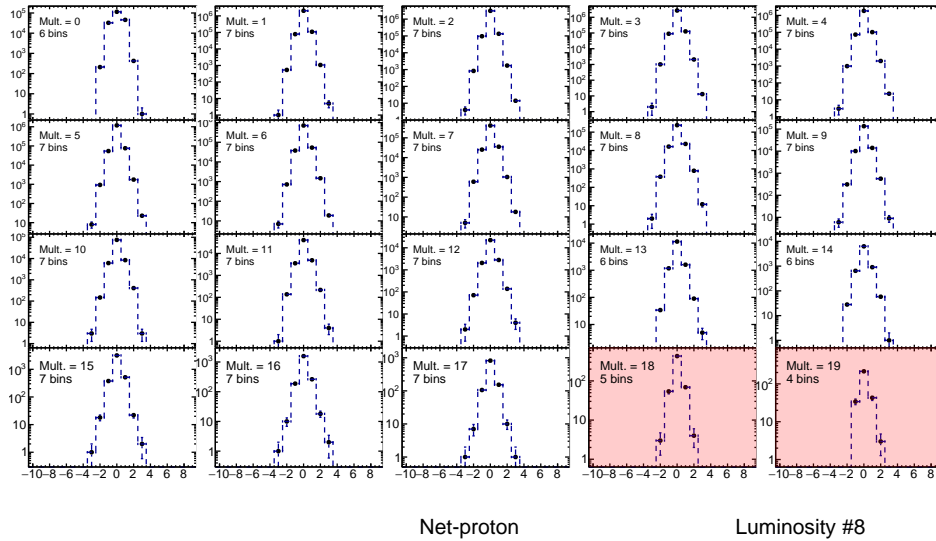


Figure D.9: Net-proton distributions for each Tofmatched in luminosity group #8.

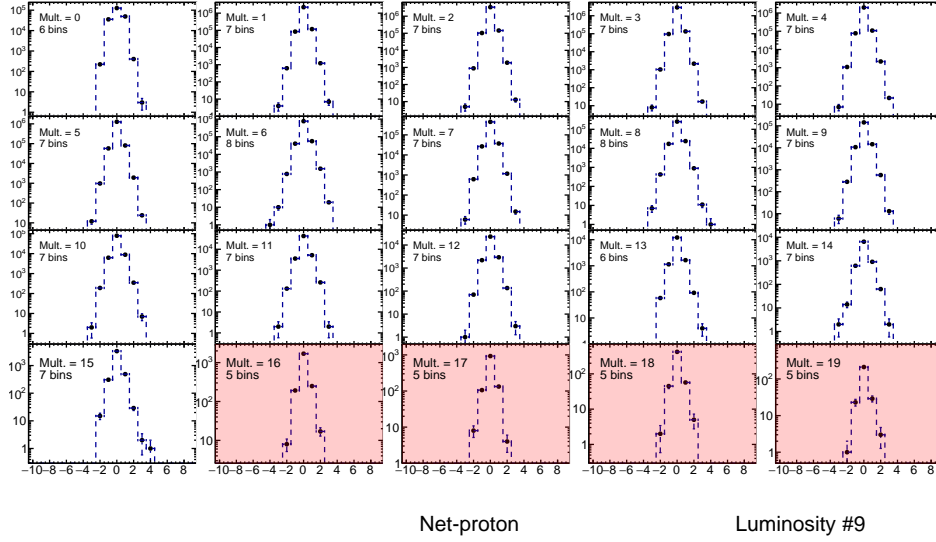


Figure D.10: Net-proton distributions for each Tofmatched in luminosity group #9.

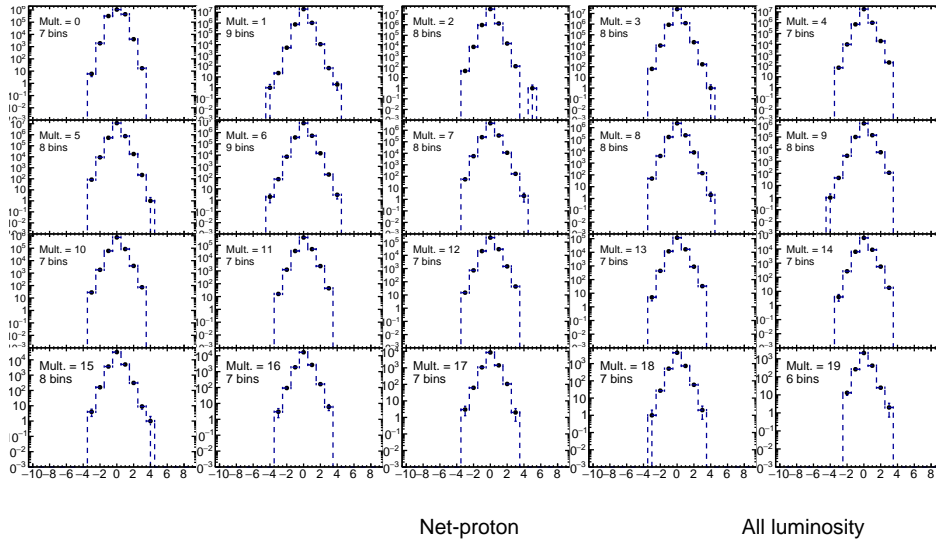


Figure D.11: Net-proton distributions for each Tofmatched in all luminosity group.

D.1.1 Multiplicity and luminosity dependence of cumulants

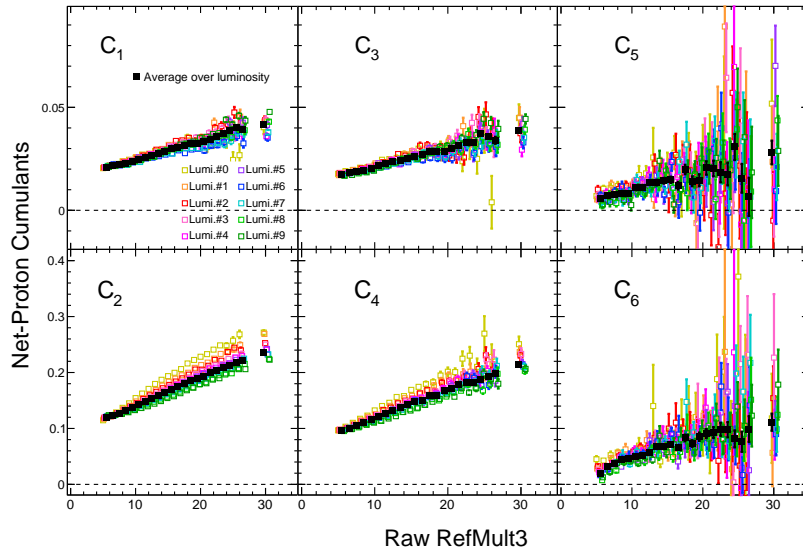


Figure D.12: Multiplicity dependence of cumulants in different luminosity groups. The black square show average over luminosity. Multiplicity $27 \leq m_{ch} < 50$ are merged.

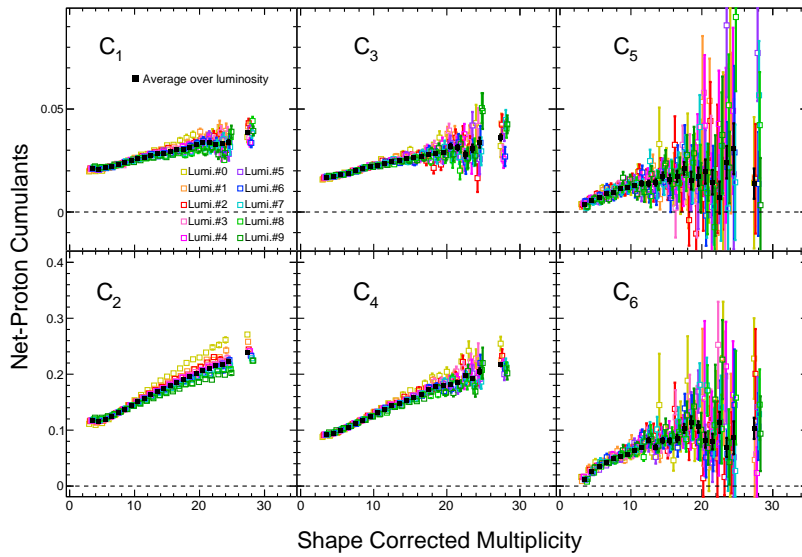


Figure D.13: Shape corrected multiplicity dependence of cumulants in different luminosity groups. The black square show average over luminosity. Shape corrected multiplicity $25 \leq m_{ch} < 40$ are merged.

D.2 Systematic study

D.2.1 Efficiency for DCA and nHitsFit

Cumulants are corrected by efficiency estimated in each cut for DCA, number of the TPC hits by embedding data. Since the embedding simulation cannot give precise information of $|n\sigma_p|$ and m^2 , they are corrected by original efficiencies as shown in Fig. 3.48 and efficiency modifications are applied.

Fig. D.14 and D.15 show p_T integrated efficiencies for proton at $0.4 < p_T < 0.8$ GeV/c in the lowest luminosity group as a function of multiplicity by combined the TPC and TOF with EMC in different cuts of DCA and number of the TPC, respectively.

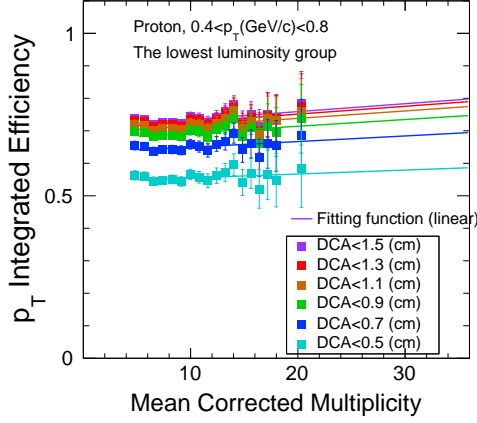


Figure D.14: Mean corrected multiplicity dependence of p_T integrated efficiencies for proton at $0.4 < p_T < 0.8$ GeV/c in the lowest luminosity group as a function of multiplicity by combined the TPC and TOF with EMC in different cuts of DCA .

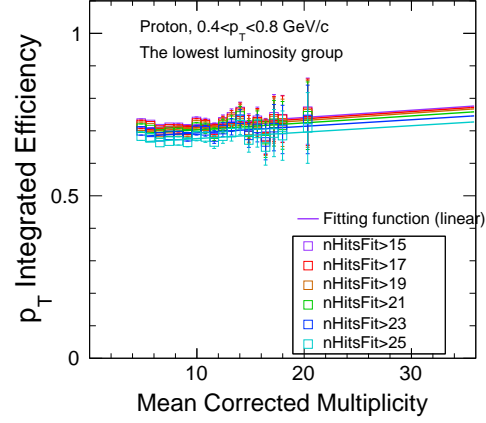


Figure D.15: Mean corrected multiplicity dependence of p_T integrated efficiencies for proton at $0.4 < p_T < 0.8$ GeV/c in the lowest luminosity group as a function of multiplicity by combined the TPC and TOF with EMC in different cuts of number of the TPC.

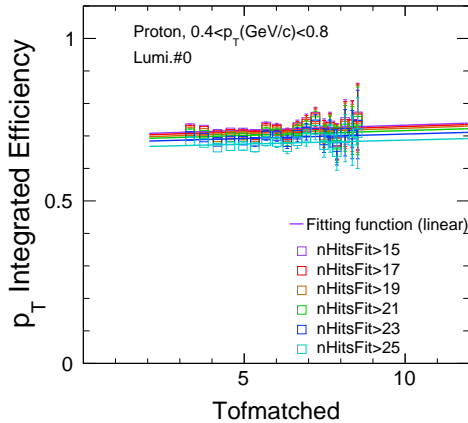


Figure D.16: Tofmatched dependence of p_T integrated efficiencies for proton at $0.4 < p_T < 0.8$ GeV/c in the lowest luminosity group as a function of multiplicity by combined the TPC and TOF with EMC in different cuts of DCA .

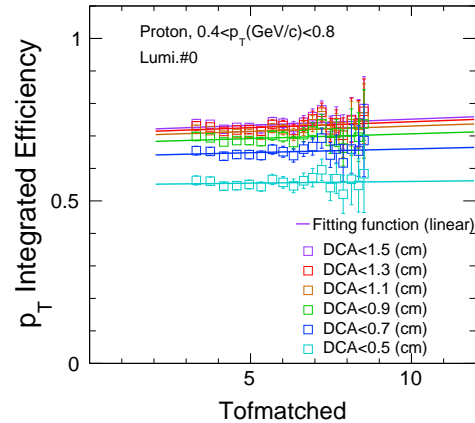


Figure D.17: Tofmatched dependence of p_T integrated efficiencies for proton at $0.4 < p_T < 0.8$ GeV/c in the lowest luminosity group as a function of multiplicity by combined the TPC and TOF with EMC in different cuts of number of the TPC.

It is found that the variation of DCA with different cuts show larger than that of number of the TPC hits (nHitsFit).

Averaged efficiency values and relative changes of efficiency respect to the default cut for proton at low p_T , antiproton at low p_T , proton at high p_T , antiproton at high p_T are shown in Tab. D.1 for DCA and number of the TPC hits.

Table D.1: Efficiency value and relative change of efficiency respect to the default cut for proton at low p_T , antiproton at low p_T , proton at high p_T , antiproton at high p_T for different cuts of DCA and number of the TPC hits. Efficiency values are averaged over multiplicity.

Cut	Efficiency value	Relative change of efficiency
DCA < 1.5cm	0.72, 0.72, 0.69, 0.69	-3.89, -4.15, -1.91, -1.99
DCA < 1.3cm	0.71, 0.71, 0.69, 0.69	-2.83, -3.08, -1.34, -1.37
DCA < 1.1cm	0.70, 0.70, 0.68, 0.68	-1.22, -1.37, -0.53, -0.53
DCA < 0.9cm	0.68, 0.68, 0.67, 0.67	+1.81, +1.80, +0.63, +0.60
DCA < 0.7cm	0.64, 0.64, 0.66, 0.66	+7.88, +8.02, +2.54, +2.36
DCA < 0.5cm	0.54, 0.54, 0.64, 0.64	+21.1, +21.2, +6.17, +5.77
Number of the TPC hits > 15	0.70, 0.70, 0.69, 0.69	-1.75, -1.81, -1.36, -1.48
the Number of the TPC hits > 17	0.70, 0.70, 0.69, 0.68	-1.13, -1.21, -0.86, -0.93
the Number of the TPC hits > 19	0.69, 0.69, 0.68, 0.68	-0.32, -0.43, -0.28, -0.28
the Number of the TPC hits > 21	0.69, 0.69, 0.68, 0.67	+0.48, +0.45, +0.31, +0.32
the Number of the TPC hits > 23	0.68, 0.68, 0.67, 0.67	+1.76, +1.87, +1.17, +1.19
the Number of the TPC hits > 25	0.66, 0.66, 0.66, 0.66	+4.24, +4.34, +2.45, +2.38

The value of C_1 and modification factor of them for (anti-)protons and net-protons for $|y| < 0.5$ and $0.4 < p_T$ (GeV/c) < 2.0 are summarized in Tab. D.2.

Table D.2: Averaged C_1 and modification factor(%) for protons at low p_T , antiprotons at low p_T , protons at high p_T , antiprotons at high p_T , net-proton at low p_T respect to the default cut.

Variable	Changed cuts	Modification [%]	
		p, \bar{p} (low p_T), p, \bar{p} (high p_T)	net-p(%)
$ n\sigma_p $	< 2.5	+3.46, +3.70, +3.12, +3.21	+2.86
	< 2.3	+2.56, +2.73, +2.29, +2.37	+2.10
	< 2.1	+1.06, +1.11, +0.95, +0.97	+0.87
	< 1.9	-1.28, -1.34, -1.16, -1.16	-1.09
	< 1.7	-4.79, -5.03, -4.32, -4.38	-4.16
	< 1.5	-9.71, -10.1, -8.82, -8.98	-8.47
DCA(cm)	< 1.5	+5.47, +3.72, +2.45, +2.19	+7.23
	< 1.3	+3.75, +2.58, +1.74, +1.58	+4.87
	< 1.1	+1.41, +0.96, +0.71, +0.66	+1.85
	< 0.9	-1.53, -1.22, -0.92, -0.86	-1.90
	< 0.7	-5.61, -4.25, -3.57, -3.45	-7.02
	< 0.5	-11.1, -8.34, -8.66, -8.26	-14.8
Number of the TPC hit	< 15	-0.60, -0.69, -0.00, -0.09	-0.03
	< 17	-0.32, -0.44, +0.03, -0.02	+0.04
	< 19	-0.05, -0.17, -0.04, -0.04	+0.10
	< 21	+0.14, +0.12, +0.00, +0.00	+0.11
	< 23	+0.34, +0.48, -0.19, -0.22	-0.05
	< 25	+0.65, +0.74, -0.82, -0.79	-0.16
m^2	$0.8 < m^2 < 1.4$	-1.27, -1.32, -6.50, -7.20	-2.61
	$0.7 < m^2 < 1.3$	-0.14, -0.12, -0.52, -0.58	-0.27
	$0.65 < m^2 < 1.25$	-0.04, -0.03, -0.13, -0.14	-0.06
	$0.75 < m^2 < 1.35$	-0.34, -0.30, -1.79, -2.00	-0.76
Efficiency	+5%	-4.76, -4.76, -4.77, -4.77	-4.75
	-5%	+5.26, +5.26, +5.25, +5.25	+5.24
	-5%(low p_T)+5%(high p_T)	+5.26, +5.25, -4.78, -4.76	+1.06
	+5%(low p_T)-5%(high p_T)	-4.75, -4.76, +5.24, +5.25	-0.52
ZDC coincidence rate(Hz)	$0 \sim 4530$	+0.09, +0.15, +0.14, +0.26	-0.03
	$4531 \sim 5782$	+0.08, +0.16, +0.13, +0.24	-0.00
	$5783 \sim 6439$	+0.08, +0.14, +0.16, +0.24	+0.05
	$6440 \sim 6984$	+0.09, +0.15, +0.16, +0.26	-0.08
	$6985 \sim 7496$	+0.09, +0.14, +0.13, +0.25	+0.05
	$7497 \sim 8094$	+0.08, +0.18, +0.15, +0.27	+0.03
	$8095 \sim 8726$	+0.08, +0.16, +0.14, +0.22	-0.03
	$8727 \sim 9484$	+0.10, +0.13, +0.14, +0.21	-0.03
	$9485 \sim 10656$	+0.07, +0.17, +0.15, +0.25	-0.06
	$10657 \sim 16000$	+0.09, +0.16, +0.15, +0.26	+0.03

D.2.2 Cumulants with different cut conditions

Figures D.18 and D.19 show mean corrected multiplicity dependence of n th-order cumulants with different cuts for systematic study. The variables, $|n\sigma_p|$, DCA, number of the TPC hits ("nHitsFit"), m^2 , efficiency, luminosity are checked at $|y| < 0.5$, $0.4 < p_T$ (GeV/c) < 2.0 . For each cuts, luminosity dependent values are calculated and the average over luminosity are employed to calculate the deviation from default cut. The DCA cuts show the largest deviations for the lower-order cumulants, while the luminosity become dominant for the higher-order. Since the number of events are divided into 10 groups, the cumulants in different luminosity show the largest statistical uncertainties. Figures D.20 and D.21 show the results of cumulant ratios. The value of C_2/C_1 with different DCA cuts show significantly large deviations. For the higher-order ratios, results in different luminosity show the largest deviations. Figures D.22-D.25 show the average cumulants and ratios over multiplicity. The results for cumulants and the ratios with different DCA cuts show the largest deviations for most orders.

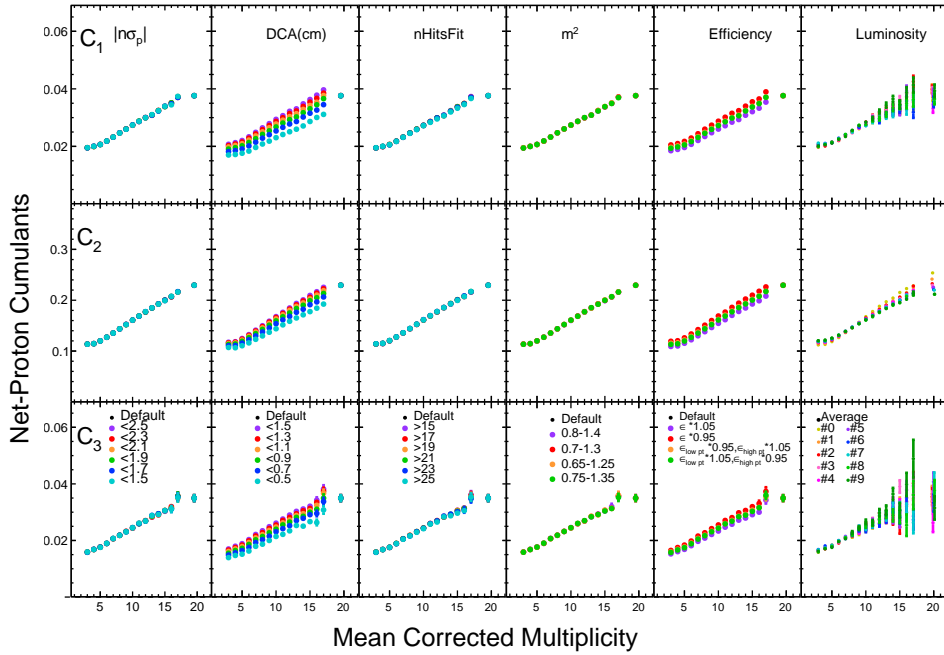


Figure D.18: Multiplicity dependence of net-proton cumulants with different cut.

D.2.3 Barlow check in systematic study

Δ/σ_{sc} distributions of cumulants and their ratios are studied for different cuts with variables: $n\sigma$, DCA, nHitsFit, m^2 , efficiency, luminosity. To create the distributions, the Δ/σ_{sc} calculated in 9 multiplicity bins for 9 acceptance are used. The results of Δ/σ_{sc} for cumulants and their ratios using TOF matched multiplicity are shown in Figs. D.26-D.35 and Figs. D.36-D.45, respectively. For each orders and cuts, the mean(μ), RMS, probabilities of entry within $\mu \pm 1\sigma$ ("Prob 1σ ") and $\mu \pm 2\sigma$ ("Prob 2σ "), and the results of barlow check of the distributions are shown. As a results, cumulants failed the barlow check except for the C_5 with DCA < 7 cm and C_2/C_1 with nHitsFit > 21 cm. Relative systematic uncertainties of C_1 for each TOF matched multiplicity are summarized in the Tabs. D.3 and D.4.

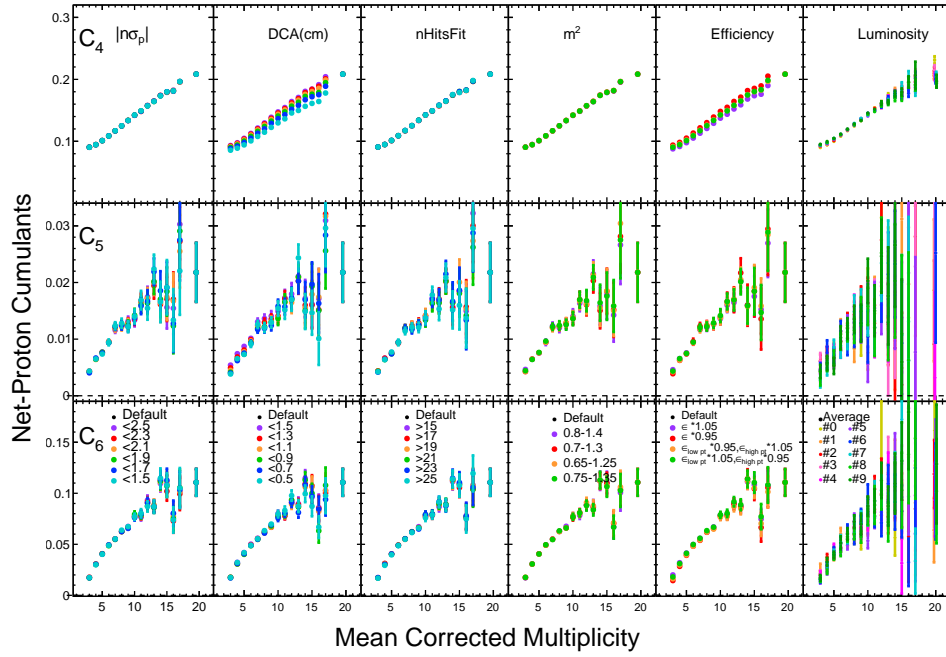


Figure D.19: Multiplicity dependence of net-proton cumulants with different cut.

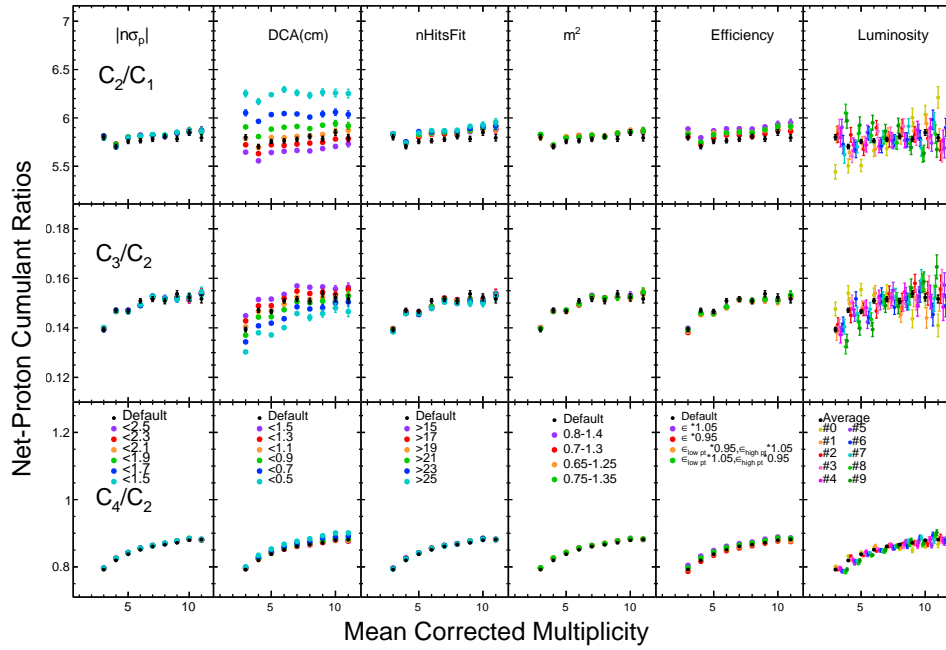


Figure D.20: Multiplicity dependence of net-proton cumulant ratios with different cut.

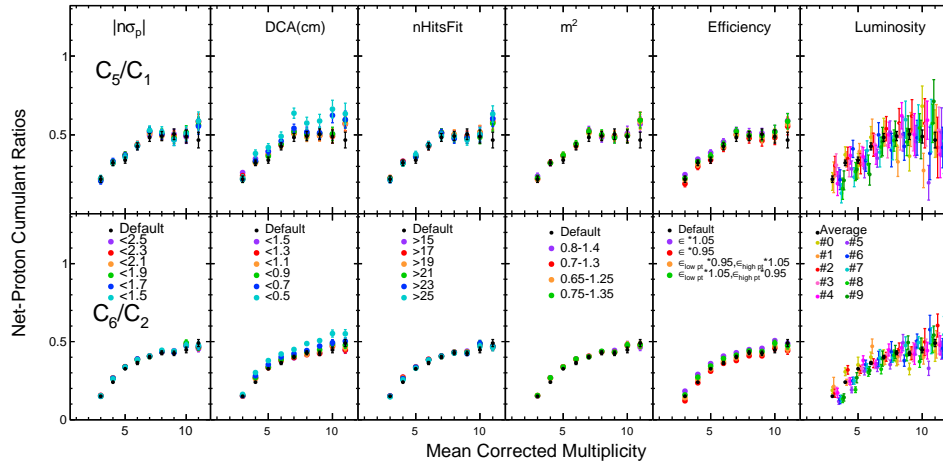


Figure D.21: Multiplicity dependence of net-proton cumulant ratios with different cut.

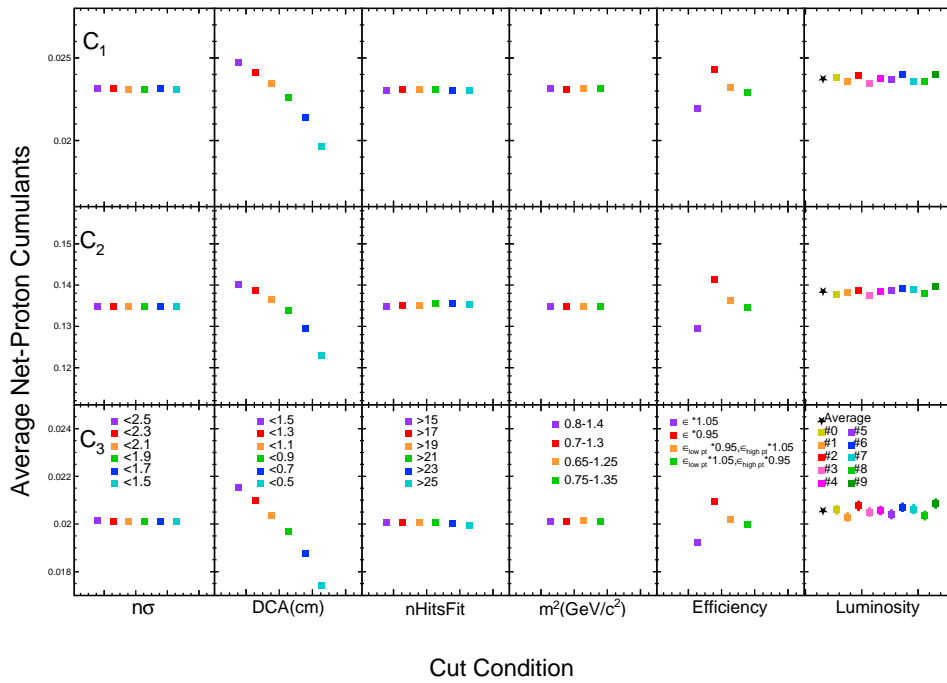


Figure D.22: Average cumulants with different luminosity.

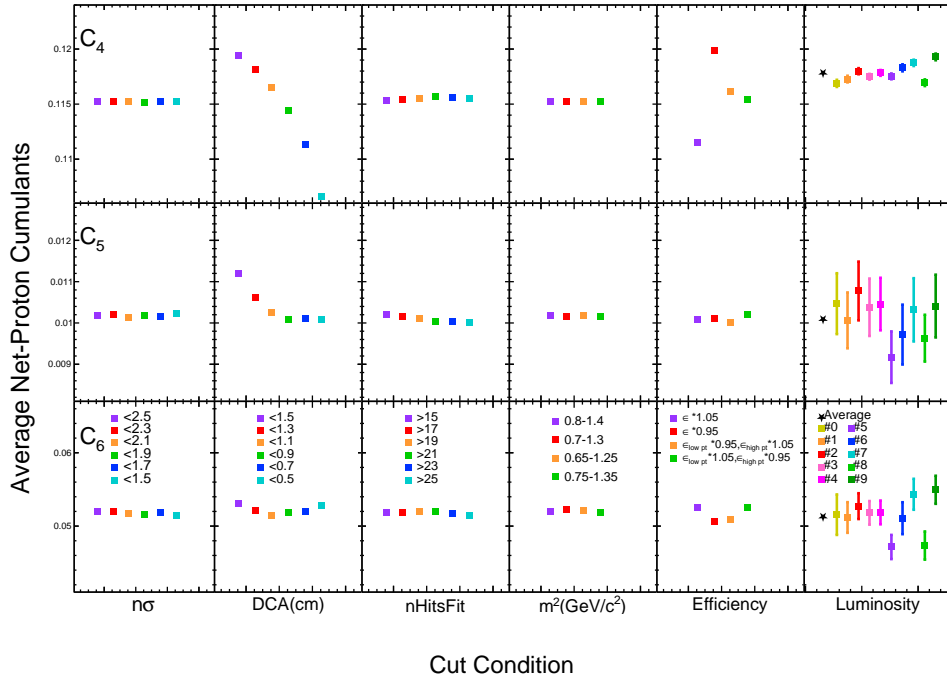


Figure D.23: Average cumulants with different luminosity.

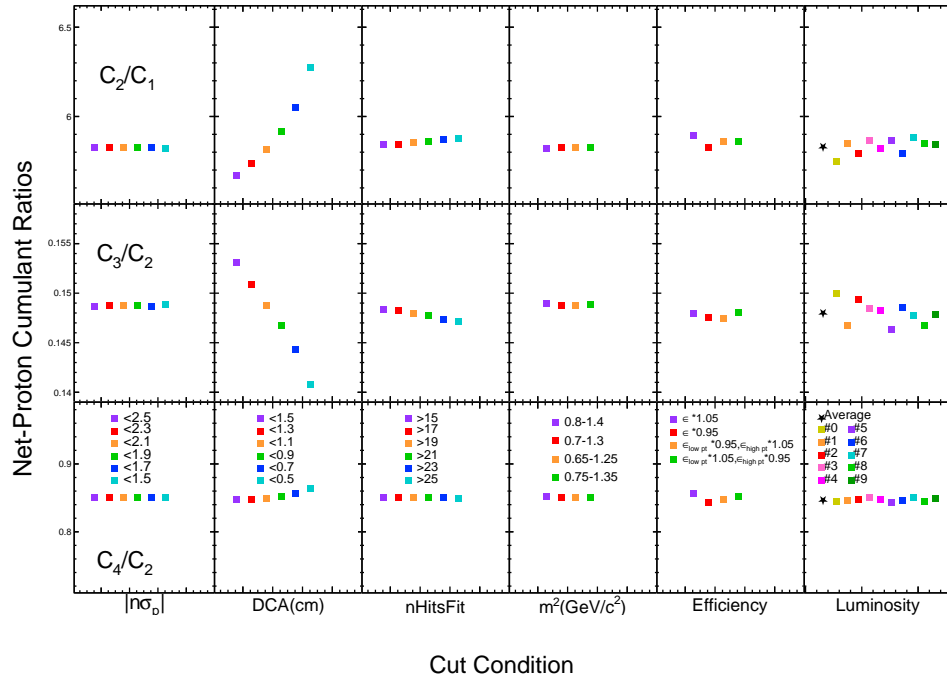


Figure D.24: Average cumulant ratios with different luminosity.

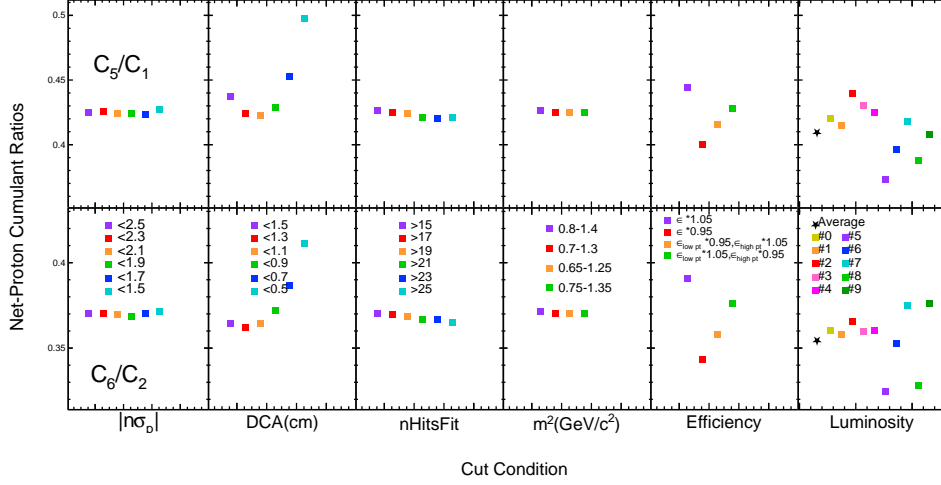


Figure D.25: Average cumulant ratios with different luminosity.

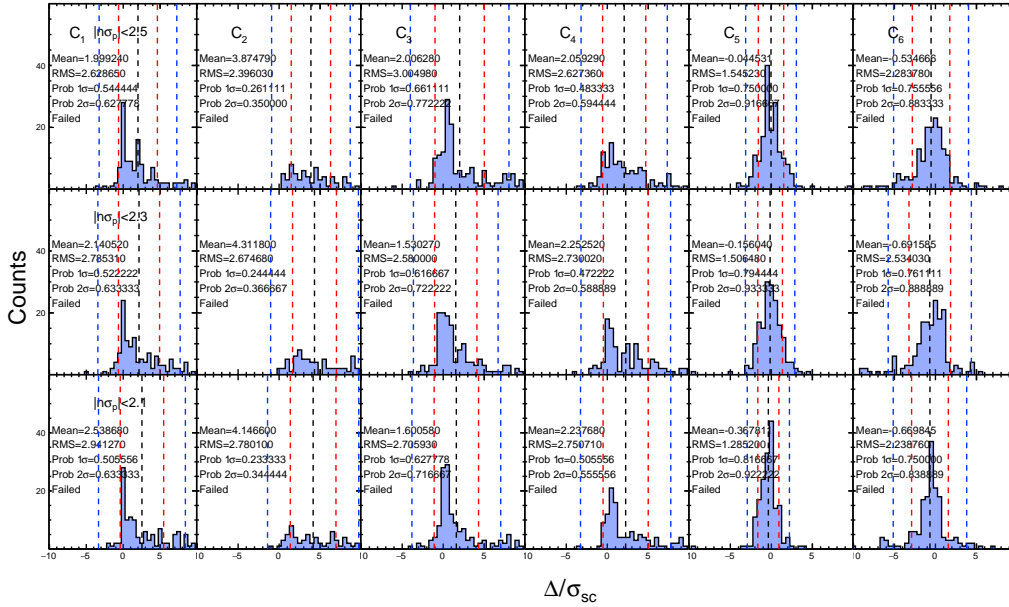


Figure D.26: Δ/σ_{sc} distributions of cumulants up to sixth-order for different $n\sigma$ cuts. The black lines show mean values of the distributions. The red and blue dotted lines show $\mu \pm 1\sigma$ and $\mu \pm 2\sigma$, respectively.

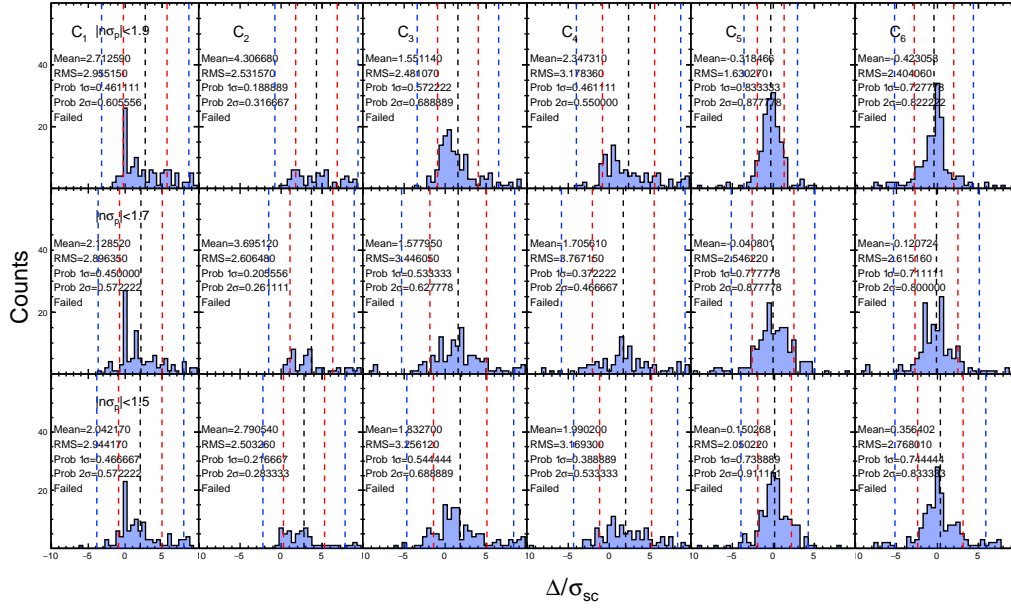


Figure D.27: Δ/σ_{sc} distributions of cumulants up to sixth-order for different $n\sigma$ cuts. The black lines show mean values of the distributions. The red and blue dotted lines show $\mu \pm 1\sigma$ and $\mu \pm 2\sigma$, respectively.

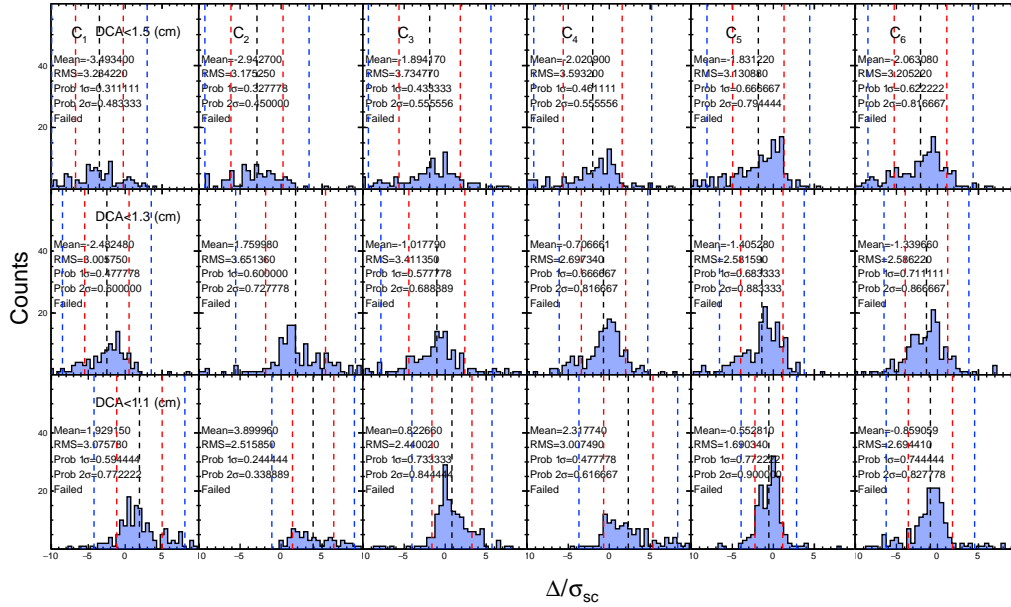


Figure D.28: Δ/σ_{sc} distributions of cumulants up to sixth-order for different DCA cuts. The black lines show mean values of the distributions. The red and blue dotted lines show $\mu \pm 1\sigma$ and $\mu \pm 2\sigma$, respectively.

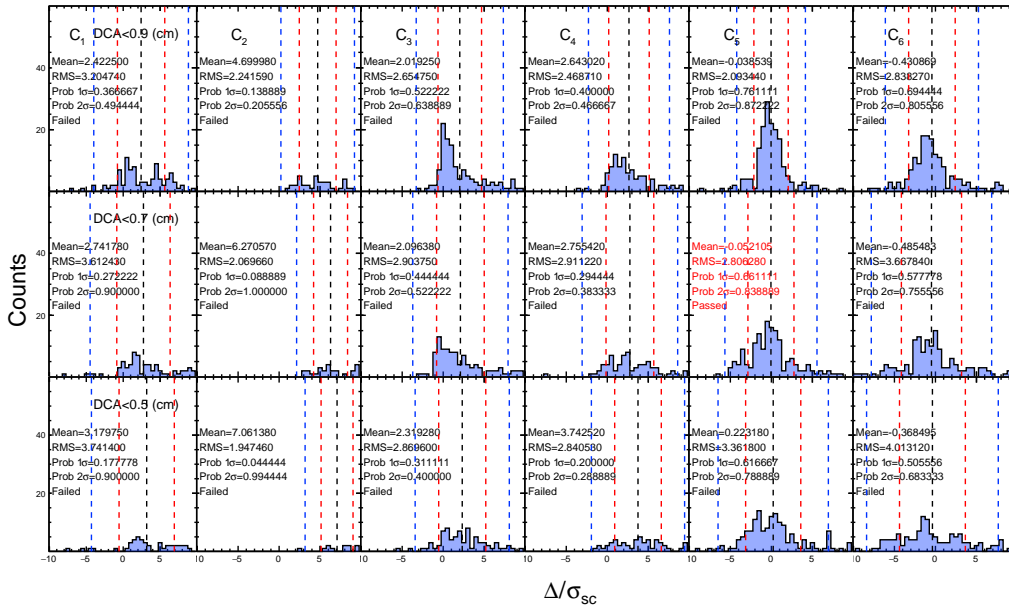


Figure D.29: Δ/σ_{sc} distributions of cumulants up to sixth-order for different DCA cuts. The black lines show mean values of the distributions. The red and blue dotted lines show $\mu \pm 1\sigma$ and $\mu \pm 2\sigma$, respectively.

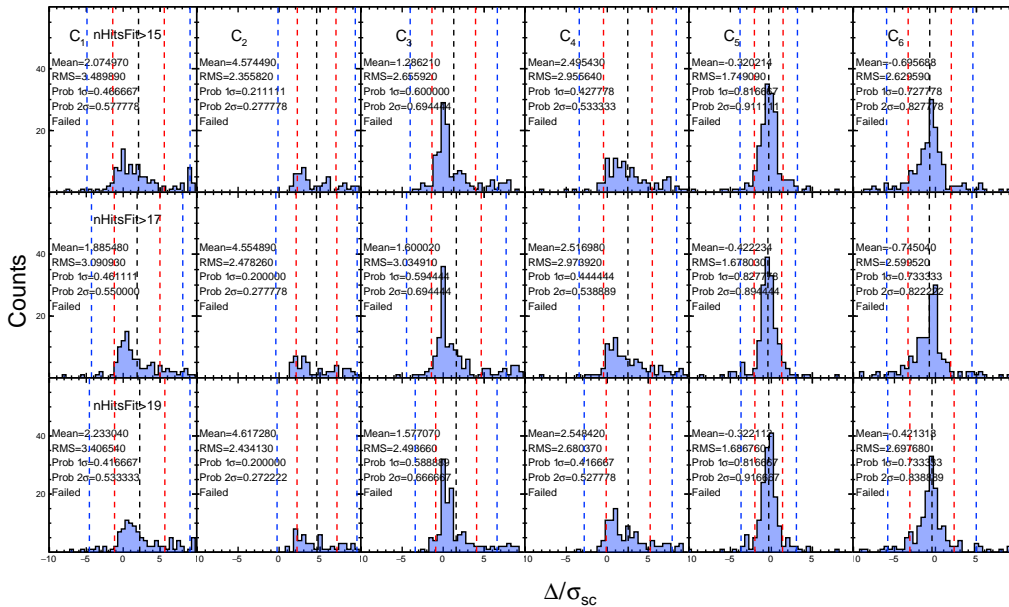


Figure D.30: Δ/σ_{sc} distributions of cumulants up to sixth-order for different nHitsFit cuts. The black lines show mean values of the distributions. The red and blue dotted lines show $\mu \pm 1\sigma$ and $\mu \pm 2\sigma$, respectively.

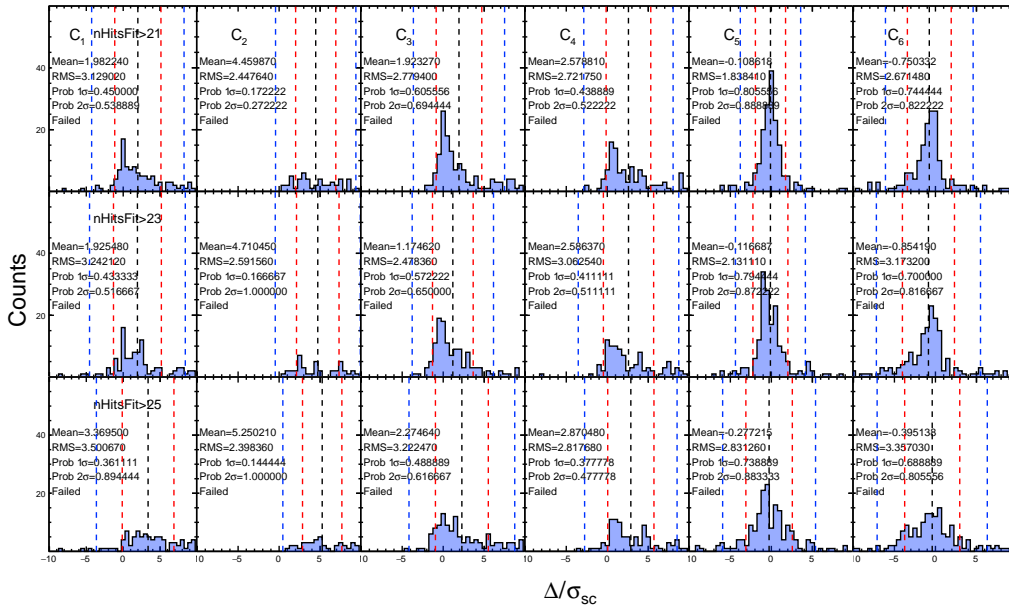


Figure D.31: Δ/σ_{sc} distributions of cumulants up to sixth-order for different nHitsFit cuts. The black lines show mean values of the distributions. The red and blue dotted lines show $\mu \pm 1\sigma$ and $\mu \pm 2\sigma$, respectively.

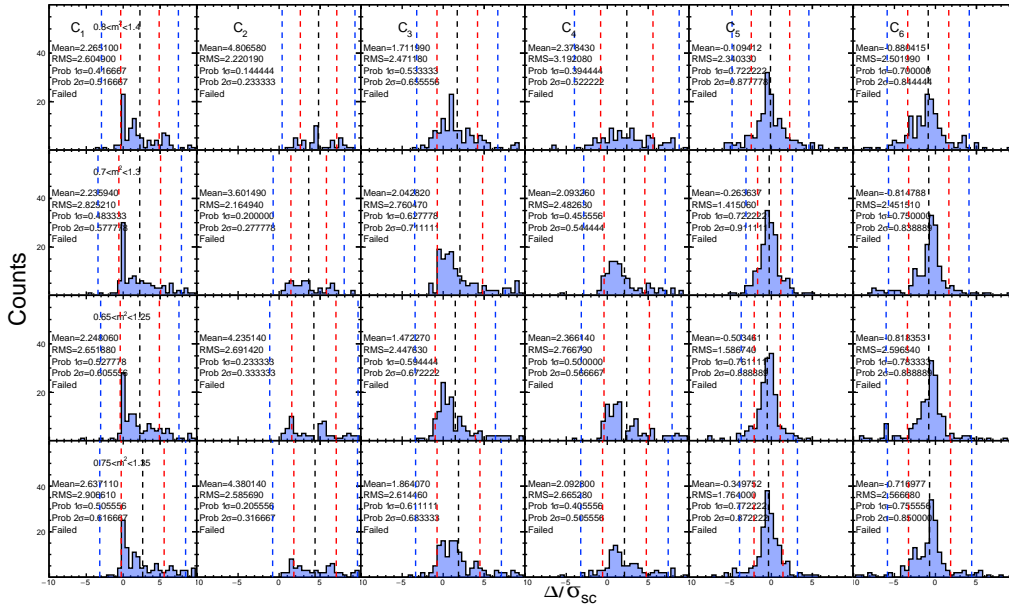


Figure D.32: Δ/σ_{sc} distributions of cumulants up to sixth-order for different m^2 cuts. The black lines show mean values of the distributions. The red and blue dotted lines show $\mu \pm 1\sigma$ and $\mu \pm 2\sigma$, respectively.

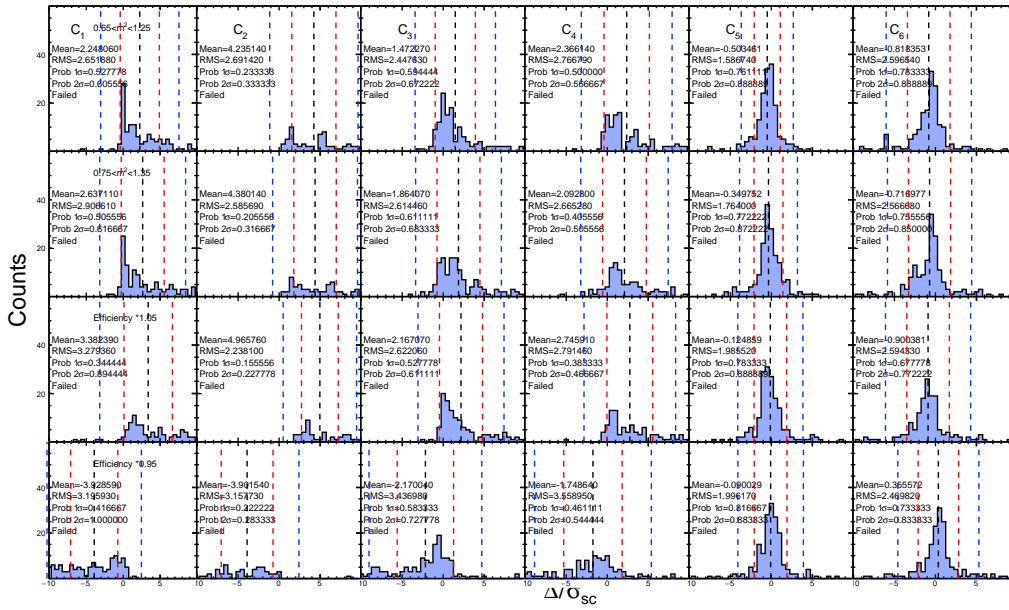


Figure D.33: Δ/σ_{sc} distributions of cumulants up to sixth-order for different efficiencies. The black lines show mean values of the distributions. The red and blue dotted lines show $\mu \pm 1\sigma$ and $\mu \pm 2\sigma$, respectively.

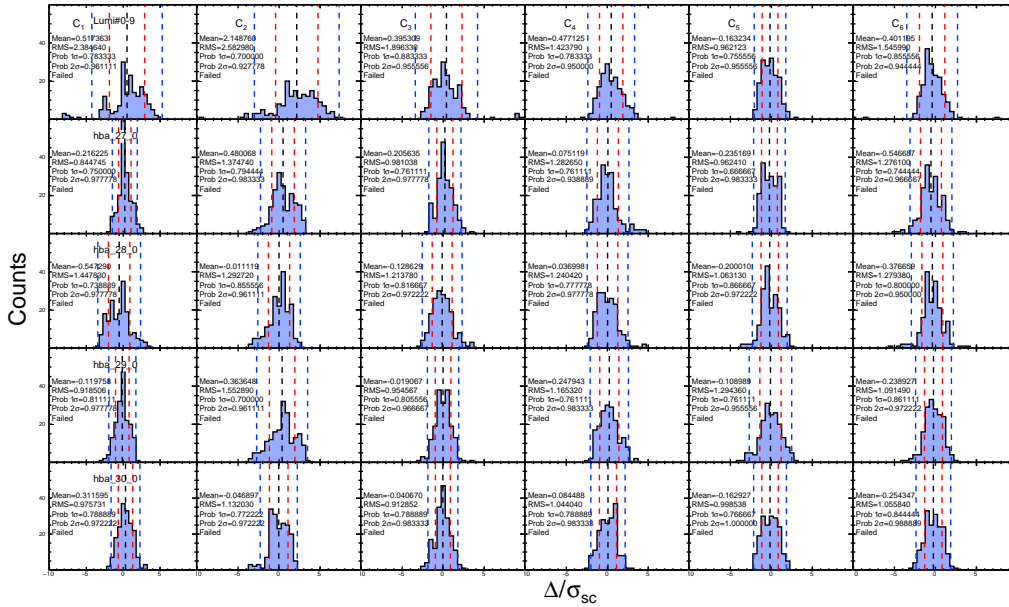


Figure D.34: Δ/σ_{sc} distributions of cumulants up to sixth-order for different luminosity groups. The black lines show mean values of the distributions. The red and blue dotted lines show $\mu \pm 1\sigma$ and $\mu \pm 2\sigma$, respectively.

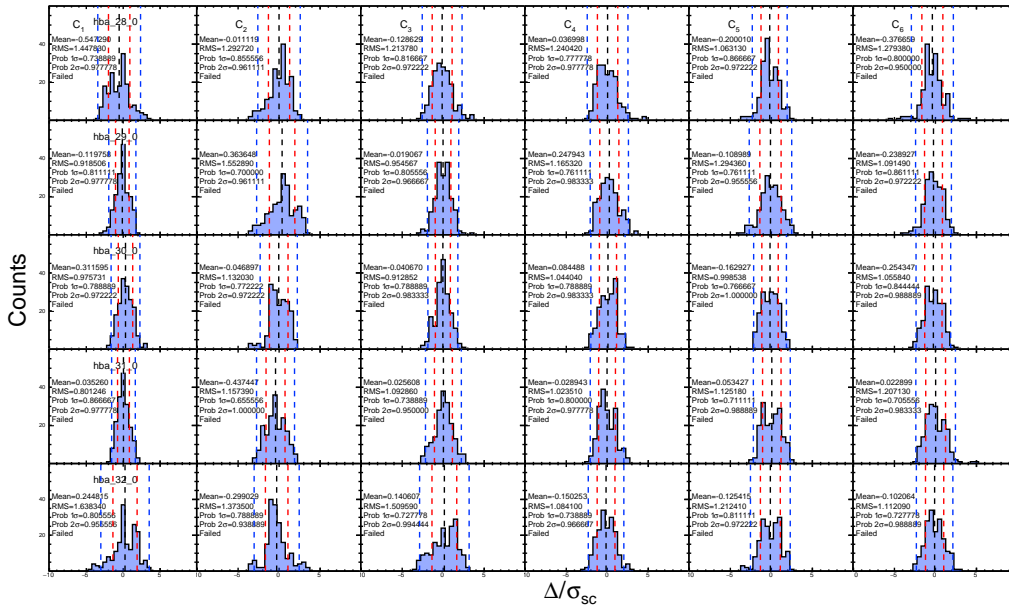


Figure D.35: Δ/σ_{sc} distributions of cumulants up to sixth-order for different luminosity groups. The black lines show mean values of the distributions. The red and blue dotted lines show $\mu \pm 1\sigma$ and $\mu \pm 2\sigma$, respectively.

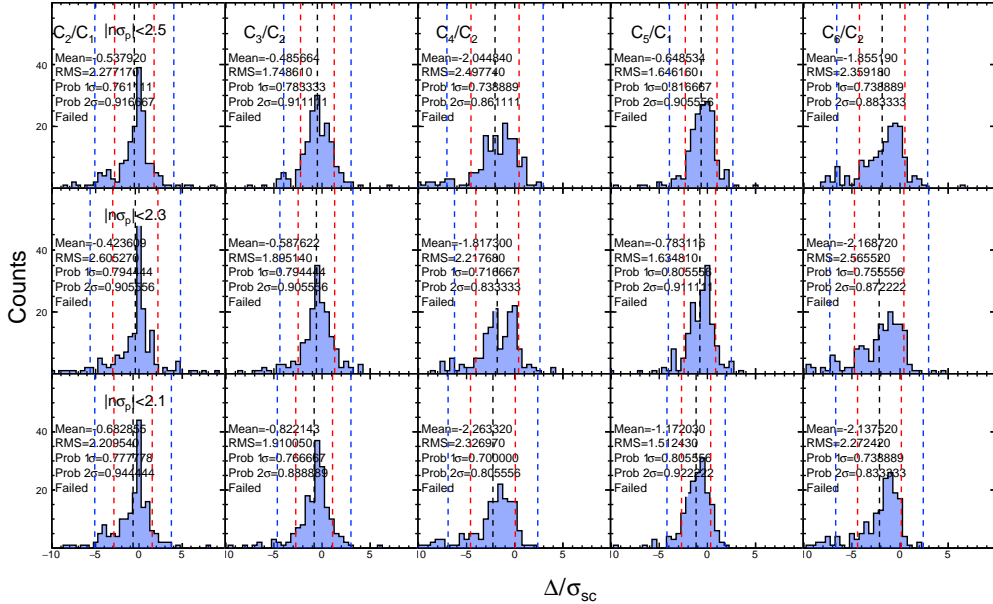


Figure D.36: Δ/σ_{sc} distributions of cumulant ratios for different $n\sigma$ cuts. The black lines show mean values of the distributions. The red and blue dotted lines show $\mu \pm 1\sigma$ and $\mu \pm 2\sigma$, respectively.

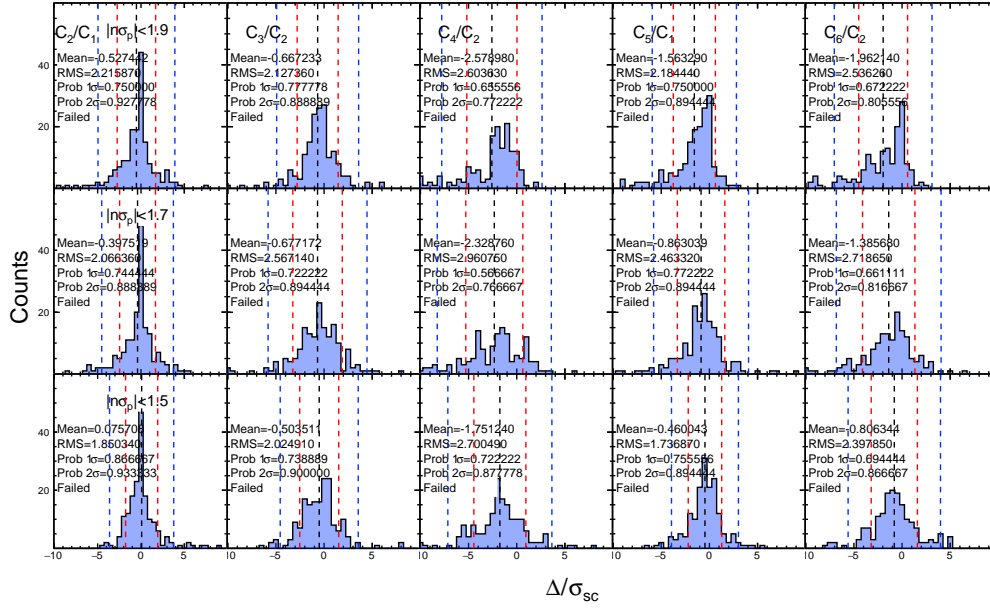


Figure D.37: Δ/σ_{sc} distributions of cumulant ratios for different $n\sigma$ cuts. The black lines show mean values of the distributions. The red and blue dotted lines show $\mu \pm 1\sigma$ and $\mu \pm 2\sigma$, respectively.

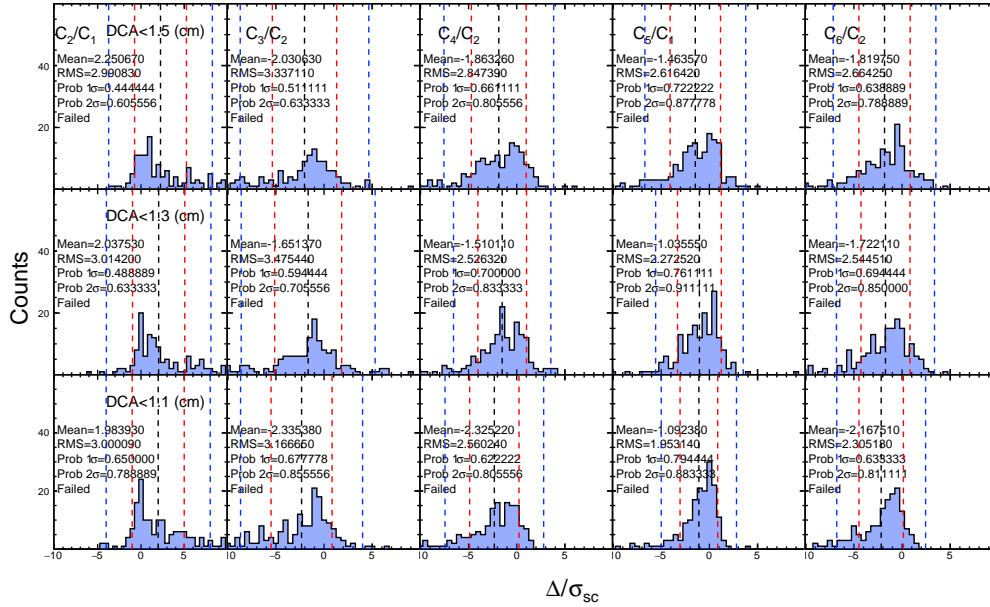


Figure D.38: Δ/σ_{sc} distributions of cumulant ratios for different DCA cuts. The black lines show mean values of the distributions. The red and blue dotted lines show $\mu \pm 1\sigma$ and $\mu \pm 2\sigma$, respectively.

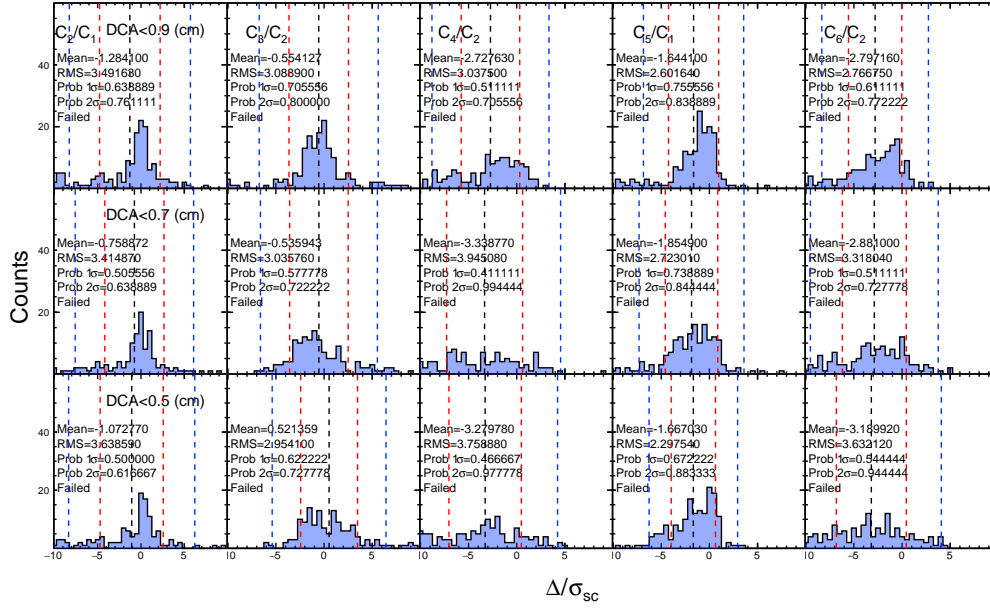


Figure D.39: Δ/σ_{sc} distributions of cumulant ratios for different DCA cuts. The black lines show mean values of the distributions. The red and blue dotted lines show $\mu \pm 1\sigma$ and $\mu \pm 2\sigma$, respectively.

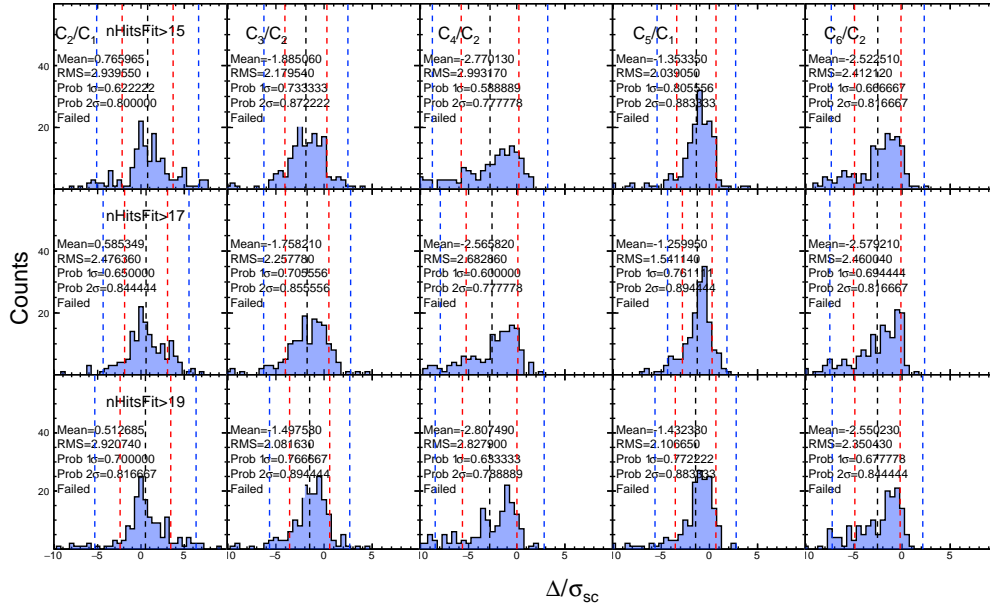


Figure D.40: Δ/σ_{sc} distributions of cumulant ratios for different nHitsFit cuts. The black lines show mean values of the distributions. The red and blue dotted lines show $\mu \pm 1\sigma$ and $\mu \pm 2\sigma$, respectively.

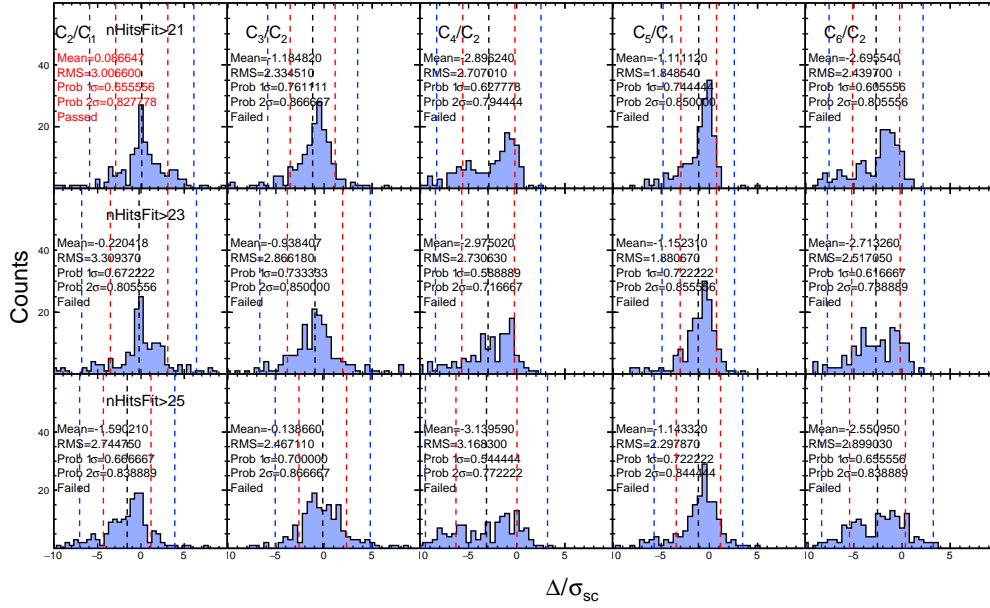


Figure D.41: Δ/σ_{sc} distributions of cumulant ratios for different $n\text{HitsFit}$ cuts. The black lines show mean values of the distributions. The red and blue dotted lines show $\mu \pm 1\sigma$ and $\mu \pm 2\sigma$, respectively.

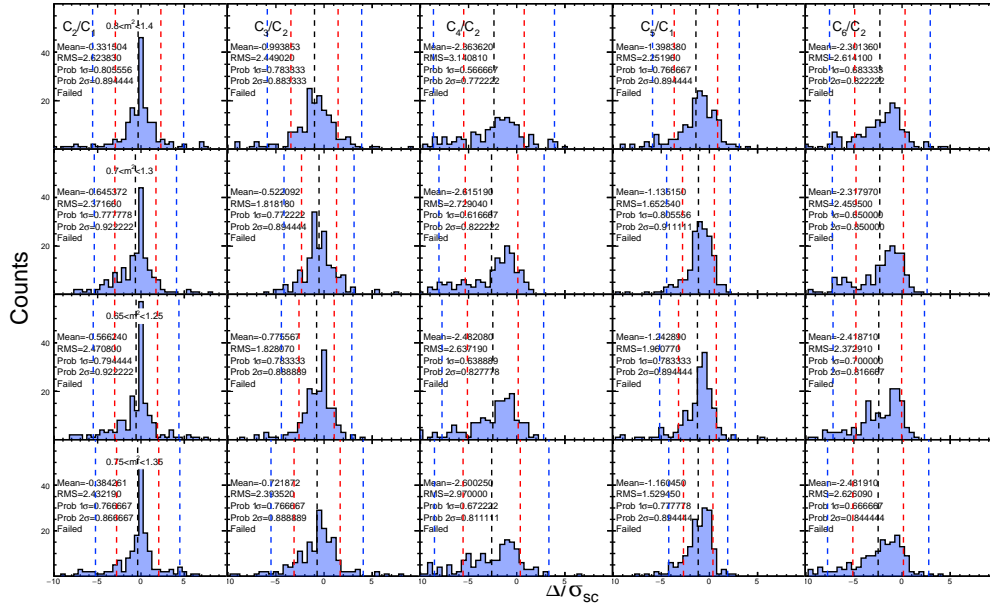


Figure D.42: Δ/σ_{sc} distributions of cumulant ratios for different m^2 cuts. The black lines show mean values of the distributions. The red and blue dotted lines show $\mu \pm 1\sigma$ and $\mu \pm 2\sigma$, respectively.

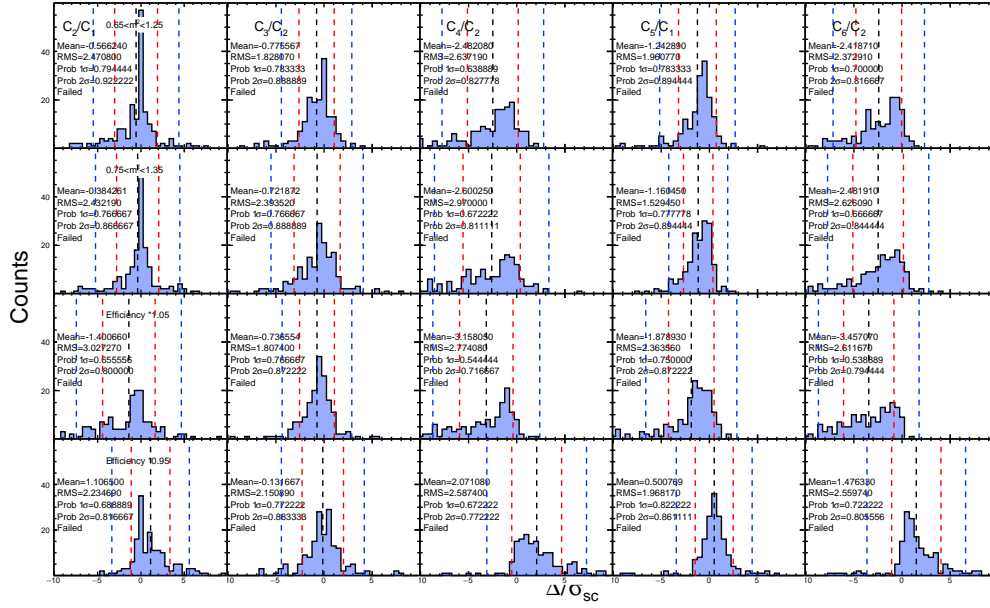


Figure D.43: Δ/σ_{sc} distributions of cumulant ratios for different efficiencies. The black lines show mean values of the distributions. The red and blue dotted lines show $\mu \pm 1\sigma$ and $\mu \pm 2\sigma$, respectively.

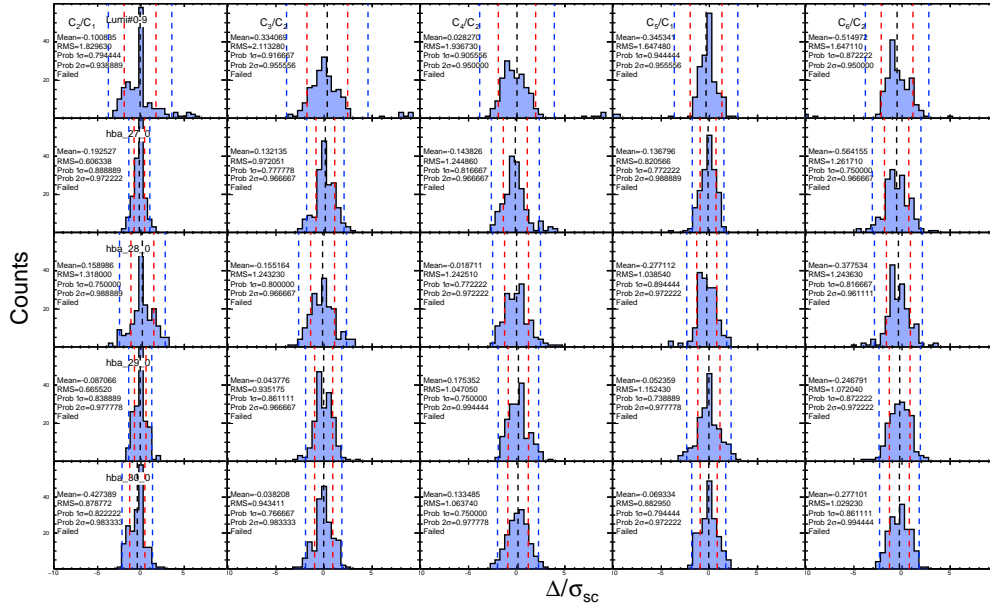


Figure D.44: Δ/σ_{sc} distributions of cumulant ratios for different luminosity groups. The black lines show mean values of the distributions. The red and blue dotted lines show $\mu \pm 1\sigma$ and $\mu \pm 2\sigma$, respectively.

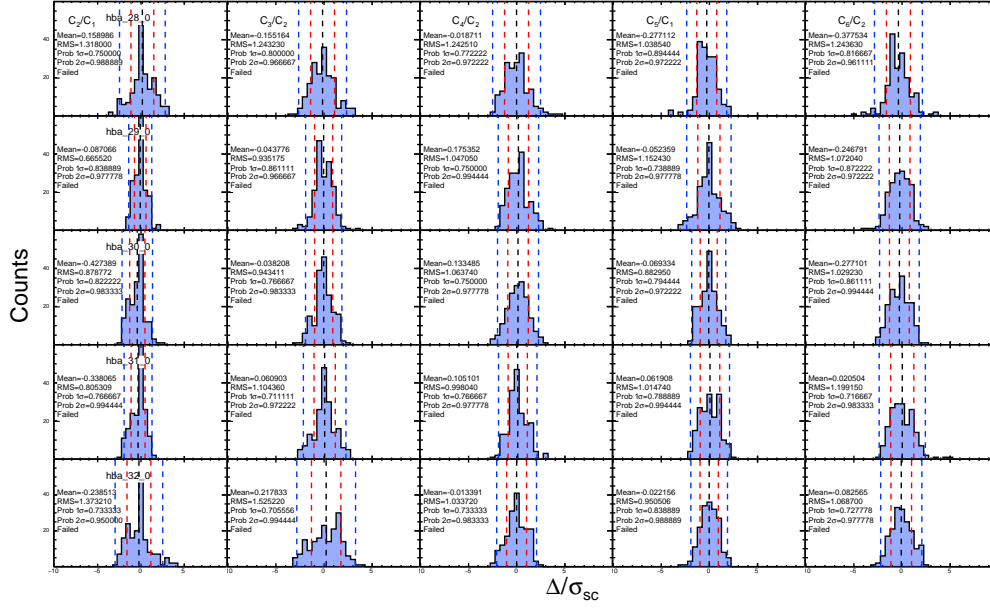


Figure D.45: Δ/σ_{sc} distributions of cumulant ratios for different luminosity groups. The black lines show mean values of the distributions. The red and blue dotted lines show $\mu \pm 1\sigma$ and $\mu \pm 2\sigma$, respectively.

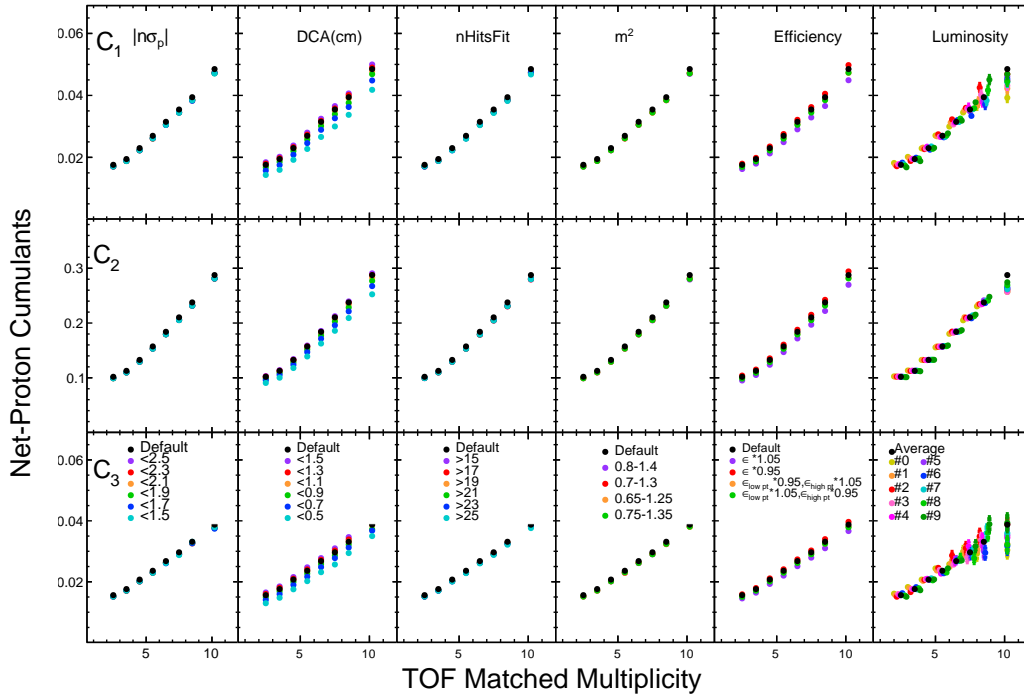


Figure D.46: Systematic study for C_1 , C_2 , and C_3 as a function of TOF matched multiplicity.

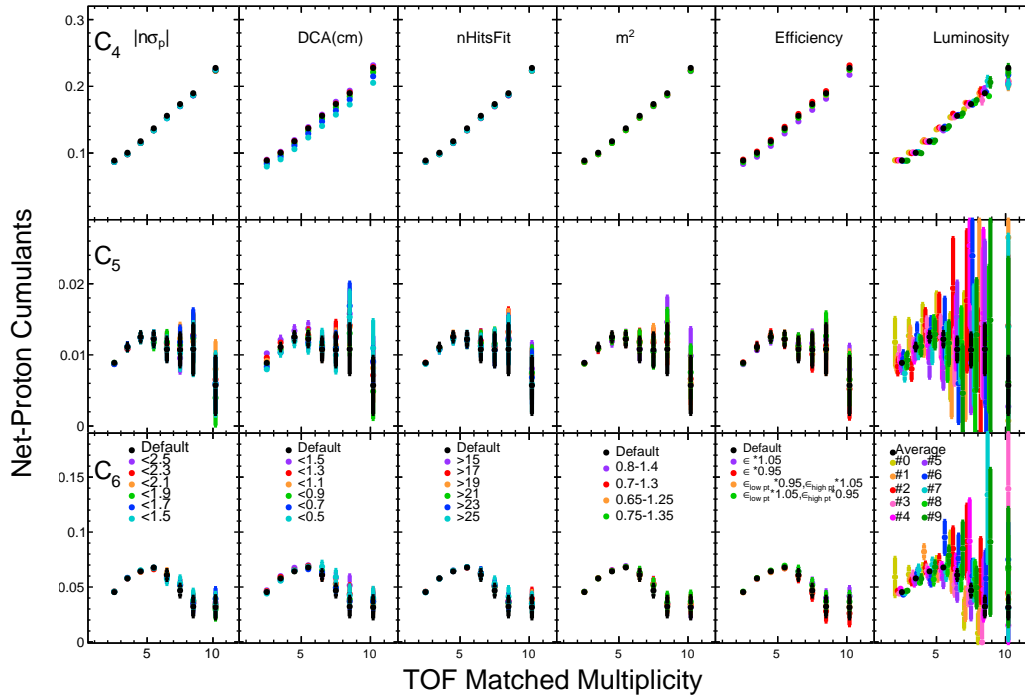


Figure D.47: Systematic study for C_4 , C_5 , and C_6 as a function of TOF matched multiplicity.

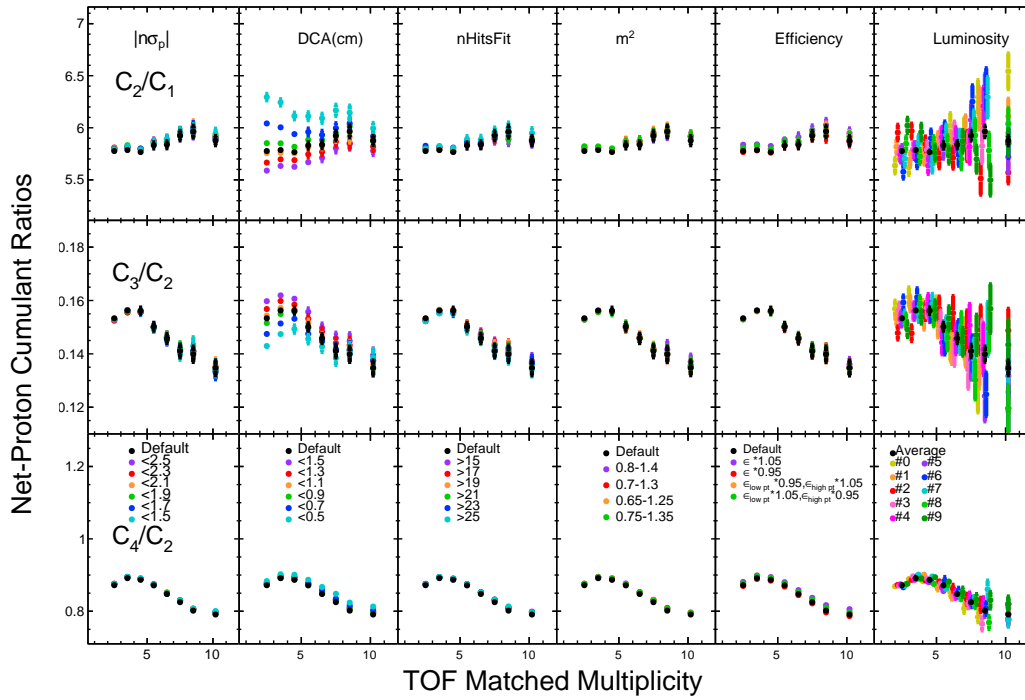


Figure D.48: Systematic study for C_2/C_1 , C_3/C_2 , and C_4/C_2 as a function of TOF matched multiplicity.

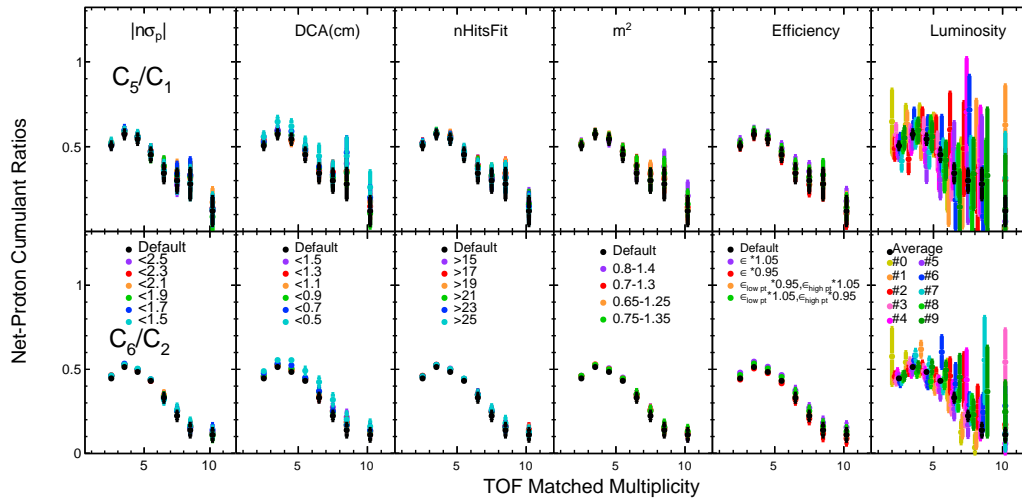


Figure D.49: Systematic study for C_5/C_2 , and C_6/C_2 as a function of TOF matched multiplicity.

Table D.3: Relative systematic uncertainty and R_j of cumulants up to sixth-order.

Order	m_{ch}^{TOF}	σ_{sys} (%)	$R_j \times 100$ (%)					
			$ n\sigma_p $	DCA	nHitsFit	m^2	Efficiency	ZDC co. rate
C_1	2	2.42	3.56	13.17	2.98	3.23	5.55	2.47
	3	2.22	3.56	12.50	2.89	3.12	5.49	2.12
	4	1.89	3.43	11.34	2.89	3.06	5.35	1.41
	5	1.80	3.50	10.79	3.11	3.16	5.46	1.43
	6	1.75	3.32	10.49	3.02	3.04	5.47	2.33
	7	1.66	3.06	10.36	2.65	2.71	5.08	3.09
	8	1.87	2.82	9.84	2.46	2.48	5.10	6.61
	9 - 20	1.78	2.97	9.21	2.79	2.93	5.28	6.31
C_2	2	0.95	2.63	7.30	2.33	2.62	4.77	0.44
	3	0.97	2.68	7.39	2.48	2.55	4.76	0.33
	4	0.98	2.59	7.52	2.51	2.51	4.75	0.17
	5	1.01	2.57	7.72	2.62	2.51	4.63	0.59
	6	1.04	2.54	7.82	2.74	2.60	4.65	1.00
	7	1.02	2.39	7.81	2.64	2.45	4.50	1.36
	8	1.12	2.55	8.06	2.91	2.65	4.60	2.06
	9 - 20	1.07	2.27	8.18	2.67	2.46	4.34	1.66
C_3	2	2.03	3.69	11.96	2.84	2.86	4.93	2.37
	3	1.84	3.43	11.30	2.71	2.78	4.74	2.64
	4	1.60	3.29	10.44	2.70	2.79	4.87	1.06
	5	1.52	3.24	9.82	2.71	2.65	4.75	2.79
	6	1.30	2.68	9.11	2.22	2.27	4.33	3.34
	7	1.31	2.83	8.78	2.01	2.06	4.16	4.46
	8	1.70	2.28	7.21	1.82	2.06	4.49	9.21
	9 - 20	1.30	3.19	6.41	1.73	1.62	3.94	7.60
C_4	2	0.77	2.43	6.60	2.16	2.37	4.12	0.37
	3	0.77	2.36	6.56	2.21	2.24	4.21	0.70
	4	0.76	2.28	6.60	2.18	2.18	4.11	0.90
	5	0.75	2.26	6.61	2.18	2.04	3.91	1.36
	6	0.70	2.24	6.40	2.14	2.01	3.75	1.33
	7	0.62	1.91	6.06	1.76	1.65	3.44	2.08
	8	0.73	1.78	5.75	1.51	1.60	3.00	4.81
	9 - 20	0.66	1.72	6.36	1.80	1.82	3.12	2.47
C_5	2	2.68	5.52	8.22	0.89	0.97	1.42	12.88
	3	2.07	3.72	5.61	2.27	2.52	2.63	11.95
	4	2.11	2.72	3.39	1.51	2.88	2.20	13.29
	5	4.71	4.80	4.94	0.87	1.08	0.51	20.54
	6	17.37	6.63	6.10	7.60	7.49	5.54	38.88
	7	66.32	10.35	10.22	5.24	7.19	6.44	79.37
	8	211.56	17.70	27.23	13.88	17.14	11.00	139.62
	9 - 20	265.64	26.67	35.99	21.09	25.42	20.14	151.86
C_6	2	1.09	1.62	1.83	0.48	0.55	0.69	10.10
	3	0.50	1.49	2.58	0.26	0.25	0.85	6.35
	4	1.44	2.14	1.40	0.78	1.07	1.11	11.60
	5	2.37	1.66	1.72	0.39	1.10	1.72	15.06
	6	6.28	3.50	6.59	2.38	2.54	4.29	23.27
	7	29.96	13.16	13.78	9.13	10.74	9.63	48.39
	8	199.13	19.40	21.61	13.71	7.58	16.16	136.25
	9 - 20	107.09	12.47	17.76	14.59	9.12	20.28	97.63

Table D.4: Relative systematic uncertainty and R_j of cumulant ratios.

Order	m_{ch}^{TOF}	σ_{sys} (%)	$R_j \times 100$ (%)					
			$ n\sigma_p $	DCA	nHitsFit	m^2	Efficiency	ZDC co. rate
C_2/C_1	2	0.27	1.43	4.30	0.53	0.60	0.61	2.23
	3	0.20	1.24	3.77	0.42	0.49	0.61	1.87
	4	0.13	1.16	2.94	0.47	0.50	0.61	1.39
	5	0.11	1.29	2.41	0.54	0.57	0.61	1.46
	6	0.09	1.09	2.09	0.41	0.47	0.71	1.68
	7	0.12	0.96	1.91	0.39	0.37	0.49	2.54
	8	0.35	0.94	1.74	0.64	0.22	0.68	5.51
	9 - 20	0.32	0.98	1.03	0.58	0.68	0.79	5.37
C_3/C_2	2	0.23	1.68	3.88	0.48	0.28	0.22	2.13
	3	0.19	1.46	3.24	0.40	0.31	0.13	2.43
	4	0.08	1.18	2.33	0.36	0.28	0.24	1.10
	5	0.15	1.48	1.89	0.40	0.27	0.16	2.94
	6	0.11	1.12	1.28	0.65	0.26	0.22	2.77
	7	0.25	1.43	1.31	1.04	0.44	0.36	4.45
	8	0.70	1.80	1.47	1.17	0.65	0.33	7.94
	9 - 20	0.51	1.57	1.84	1.28	0.95	0.45	6.51
C_4/C_2	2	0.02	0.43	0.71	0.38	0.44	0.61	0.33
	3	0.01	0.36	0.64	0.31	0.33	0.52	0.53
	4	0.02	0.39	0.86	0.34	0.42	0.55	0.84
	5	0.03	0.31	0.89	0.38	0.46	0.63	1.04
	6	0.03	0.34	1.21	0.53	0.51	0.74	0.80
	7	0.05	0.69	1.42	0.79	0.69	0.89	0.97
	8	0.18	0.70	1.55	1.04	0.74	1.12	3.47
	9 - 20	0.07	0.79	1.51	0.89	0.64	1.07	1.38
C_5/C_1	2	2.24	4.61	5.86	2.83	2.59	3.57	11.88
	3	1.63	3.42	5.72	1.18	0.61	2.56	10.51
	4	2.79	3.06	6.86	2.62	1.60	2.95	14.30
	5	5.33	4.95	6.37	3.13	4.21	4.72	20.44
	6	19.25	8.66	11.88	10.23	10.07	8.52	37.82
	7	70.66	10.93	9.95	7.60	9.01	9.84	81.31
	8	216.55	17.84	29.26	14.74	18.19	11.56	140.71
	9 - 20	252.57	25.33	34.43	22.42	26.31	20.43	147.71
C_6/C_2	2	1.76	3.65	5.33	2.87	3.27	4.29	9.84
	3	0.91	3.06	4.20	2.41	2.72	3.64	6.16
	4	2.30	3.31	6.97	3.26	3.53	3.70	11.59
	5	3.01	1.85	6.15	2.68	3.39	4.81	14.77
	6	7.97	3.33	11.81	5.18	4.99	7.24	23.29
	7	32.22	14.41	16.66	11.12	12.60	11.43	48.20
	8	185.89	19.99	22.57	15.27	9.25	16.72	130.70
	9 - 20	108.13	13.50	20.54	16.72	10.93	20.51	96.90

D.3 Luminosity independent multiplicity

To check the consistency of event sample with Fig. 4.6, the average value of cumulant ratios in Figs. 4.11 and 4.6 are compared as shown in Fig. D.51. It should be note that the range used for average is $0 \leq m_{ch}^{\text{TOF}} < 20$ and $0 \leq m_{ch} < 30$, respectively to make the event sample consistent. The values of m_{ch}^{TOF} are consistent with data using mean corrected multiplicity.

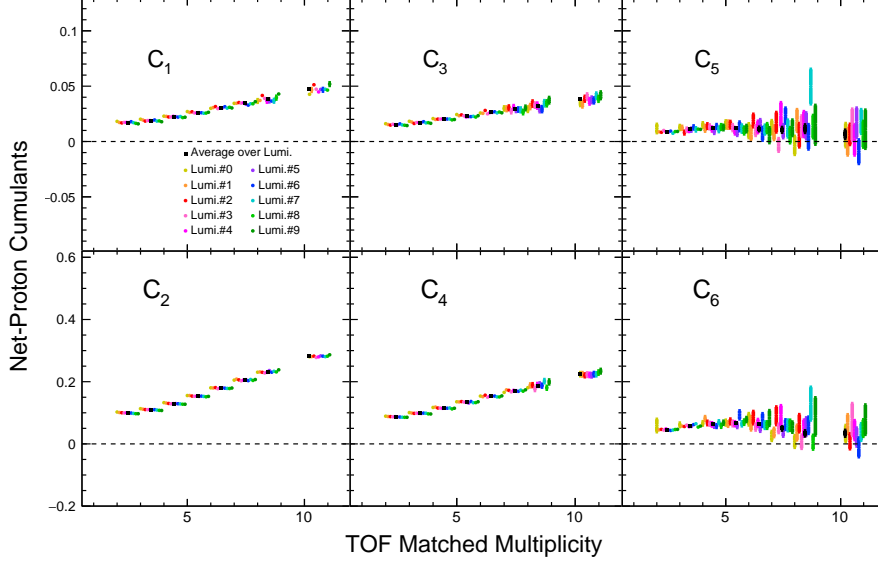


Figure D.50: TOF matched multiplicity dependence of efficiency corrected cumulants up to the sixth-order.

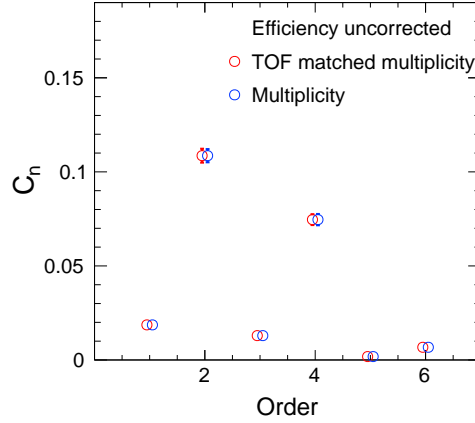


Figure D.51: Average cumulants for TOF matched multiplicity and multiplicity. The values are not corrected by efficiency. The red and blue squares represent TOF matched multiplicity and mean corrected multiplicity, respectively. The range of averaging is $0 \leq m_{ch}^{\text{TOF}} < 20$ and $0 \leq m_{ch} < 30$, respectively.

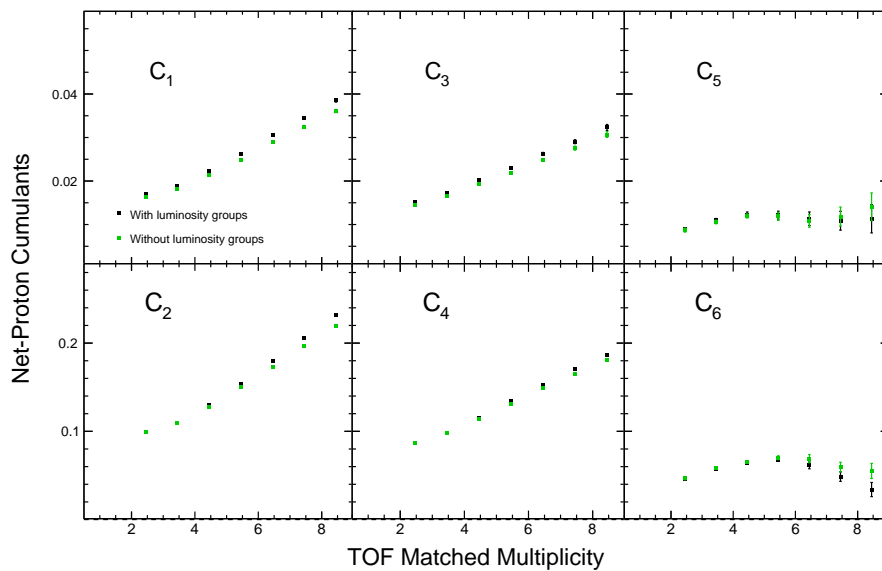


Figure D.52: Comparison of cumulants up to sixth-order with/without luminosity grouping.

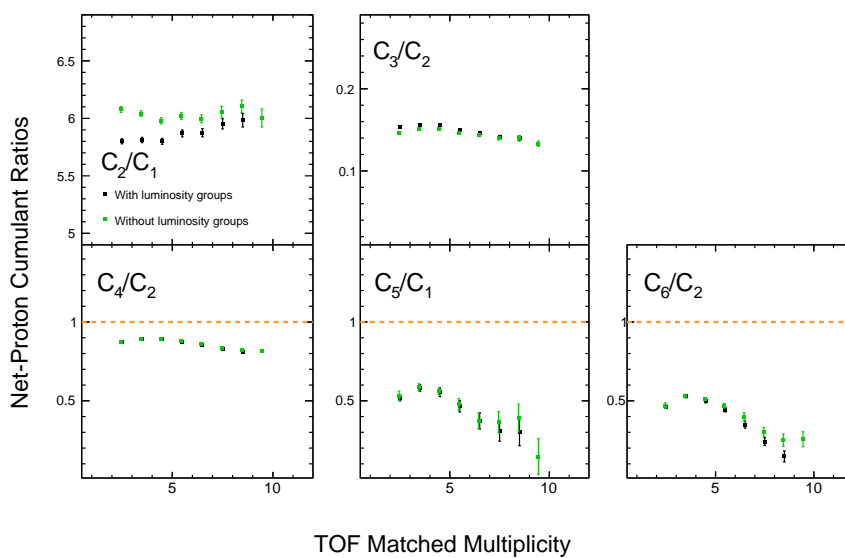


Figure D.53: Comparison of cumulant ratios up to sixth-order with/without luminosity grouping.

D.4 TOF matched multiplicity in Au+Au collisions

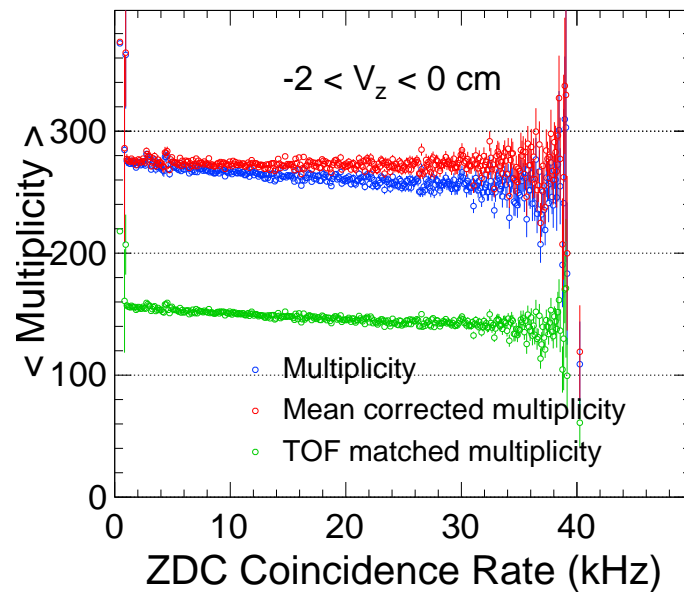


Figure D.54: ZDC coincidence rate dependence of average multiplicity measured in Au+Au collisions at $\sqrt{s_{NN}} = 200$ GeV. The blue circles are raw multiplicity and red circles are mean corrected multiplicity. The green circles are TOF matched multiplicity. The solid lines are linear fitting function.

Bibliography

- [1] Y. Wu for the STAR Collaboration. Recent results for STAR $\sqrt{s_{NN}} = 4.22$ GeV Al+Au and $\sqrt{s_{NN}} = 4.5$ GeV Au+Au Fixed-Target Collisions. *Nucl. Phys.*, A982:899–902, 2019.
- [2] M. Asakawa and M. Kitazawa. Fluctuations of conserved charges in relativistic heavy ion collisions: An introduction. *Prog. Part. Nucl. Phys.*, 90:299–342, 2016.
- [3] M. Cheng et al. Baryon number, strangeness, and electric charge fluctuations in QCD at high temperature. *Phys. Rev. D.*, 79:074505, 2009.
- [4] J. Adam et al. Nonmonotonic Energy Dependence of Net-Proton Number Fluctuations. *Phys. Rev. Lett.*, 126:092301, 2021.
- [5] M. A. Stephanov. Sign of Kurtosis near the QCD Critical Point. *Phys. Rev. Lett.*, 107:052301, 2011.
- [6] A. Bazavov et al. Skewness, kurtosis, and the fifth and sixth order cumulants of net baryon-number distributions from lattice QCD confront high-statistics STAR data. *Phys. Rev. D*, 101:074502, 2020.
- [7] B. Friman et al. Fluctuations as probe of the QCD phase transition and freeze-out in heavy ion collisions at LHC and RHIC. *Eur. Phys. J.*, C71:1694, 2011.
- [8] M. S. Abdallah et al. Measurement of the sixth-order cumulant of net-proton multiplicity distributions in Au+Au collisions at $\sqrt{s_{NN}} = 27, 54.4,$ and 200 GeV at RHIC. *Phys. Rev. Lett.*, 127, 2021.
- [9] ALICE Collaboration. Enhanced production of multi-strange hadrons in high-multiplicity proton–proton collisions. *Nature Physics*, 13:535, 2017.
- [10] ATLAS Collaboration. Measurement of long-range azimuthal anisotropies and associated Fourier coefficients for pp collisions at $\sqrt{s} = 5.02$ and 13 TeV and p +Pb collisions at $\sqrt{s_{NN}} = 5.02$ TeV with the ATLAS detector. *Phys. Rev. C*, 96:024908, 2017.
- [11] L. Adamczyk et al. Energy Dependence of Moments of Net-proton Multiplicity Distributions at RHIC. *Phys. Rev. Lett.*, 112:032302, 2014.
- [12] V.H. Rajbar and S.Y. Lee. Spin coupling resonance and suppression in the AGS. *Phys. Rev.*, 7:051001, 2004.
- [13] M. Anderson et al. The Star time projection chamber: A Unique tool for studying high multiplicity events at RHIC. *Nucl. Instrum. Meth.*, A499:659–678, 2003.
- [14] W. J. Llope et al. The TOFp/pVPD time-of-flight system for STAR. *Nucl. Instrum. Methods A*, 522:252, 2004.
- [15] C. Adler et al. The RHIC zero degree calorimeters. *Nucl. Instrum. Methods A*, 470:488, 2001.
- [16] L. Michael et al. Glauber Modeling in High Energy Nuclear Collisions. *Rev. Nucl. Part. Sci.*, 57:205, 2007.
- [17] M. S. Abdallah et al. Cumulants and Correlation Functions of Net-proton, Proton and Antiproton Multiplicity Distributions in Au+Au Collisions at RHIC. *Phys. Rev. C.*, 104:024902, 2021.

- [18] T. Nonaka. First measurement of the sixth order cumulant of net-proton multiplicity distributions in $\sqrt{s_{\text{NN}}} = 200$ GeV Au+Au collisions at the STAR experiment. *Thesis for the Doctor of Philosophy in Science*, page 71, 2018.
- [19] P. Ashish. PYTHIA model results on net-proton cumulants for p+p at $\sqrt{s_{\text{NN}}} = 200$ GeV. page https://drupal.star.bnl.gov/STAR/system/files/pythia8_pp200GeV_DECAY_0.pdf, 2021.
- [20] L. Adamczyk et al. Bulk properties of the medium produced in relativistic heavy-ion collisions from the beam energy scan program. *Phys. Rev.*, C96:044904, 2017.
- [21] S. Borsanyi et al. Higher order fluctuations and correlations of conserved charges from lattice QCD. *JHEP*, 10:205, 2018.
- [22] Y. Aoki et al. The order of the quantum chromodynamics transition predicted by the standard model of particle physics. *Nature*, 443:675–678, 2006.
- [23] E. S. Bowman and B. Kapusta, Joseph I. Critical Points in the Linear Sigma Model with Quarks. *Phys. Rev. C*, 79:015202, 2009.
- [24] M. A. Stephanov. Non-Gaussian fluctuations near the QCD critical point. *Phys. Rev. Lett.*, 102:032301, 2009.
- [25] S. Gupta ER. V. Gavai. QCD at finite chemical potential with six time slices. *Phys. Rev. D.*, 78:114503, 2008.
- [26] A. Bazavov et al. Fluctuations and correlations of net baryon number, electric charge, and strangeness: A comparison of lattice QCD results with the hadron resonance gas model. *Phys. Rev. D.*, 86:034509, 2012.
- [27] S. Borsanyi et al. Fluctuations of conserved charges at finite temperature from lattice QCD. *JHEP*, 138, 2011.
- [28] M. Kitazawa and M. Asakawa. Relation between baryon number fluctuations and experimentally observed proton number fluctuations in relativistic heavy ion collisions. *Phys. Rev.*, C86:024904, 2012. [Erratum: *Phys. Rev.*C86,069902(2012)].
- [29] M. Asakawa, S. Ejiri, and M. Kitazawa. Third moments of conserved charges as probes of QCD phase structure. *Phys. Rev. Lett.*, 103:262301, 2009.
- [30] A. Bazavov et al. The QCD Equation of State to $\mathcal{O}(\mu_B^6)$ from Lattice QCD. *Phys. Rev.*, D95(5):054504, 2017.
- [31] A. Bazavov et al. Skewness, kurtosis and the 5th and 6th order cumulants of net baryon-number distributions from lattice QCD confront high-statistics STAR data. *Phys. Rev.*, D 101:074502, 2020.
- [32] A. Kisiel. Signatures of collective flow in high-multiplicity *pp* collisions. *Phys. Rev. C*, 84:044913, 2011.
- [33] M. Aaboud et al. Measurements of long-range azimuthal anisotropies and associated Fourier coefficients for *pp* collisions at $\sqrt{s}=5.02$ and 13 TeV and *p*+Pb collisions at $\sqrt{s_{\text{NN}}}=5.02$ TeV with the ATLAS detector. *Phys. Rev.*, C96:024908, 2017.
- [34] M. Beddo et al. The STAR Barrel Electromagnetic Calorimeter. *Nucl. Instrum. Methods A*, 499:735, 2003.
- [35] J. Anthony et al. Correlated forward-backward dissociation and neutron spectra as a luminosity monitor in heavy ion colliders. *Nucl. Instrum. Methods A*, 417, 1998.
- [36] V. Koch A. Bzdak and V. Skokov. Multiplicity-dependent and nonbinomial efficiency corrections for particle number cumulants. *Phys. Rev. C*, 94:064907, 2016.
- [37] A. Bzdak and V. Koch. Local Efficiency Corrections to Higher Order Cumulants. *Phys. Rev.*, C91(2):027901, 2015.

- [38] X. Luo. Unified description of efficiency correction and error estimation for moments of conserved quantities in heavy-ion collisions. *Phys. Rev. C.*, 91:034907, 2015.
- [39] M. Kitazawa. Efficient formulas for efficiency correction of cumulants. *Phys. Rev.*, C93(4):044911, 2016.
- [40] A. Bzdak and V. Koch. Acceptance corrections to net baryon and net charge cumulants. *Phys. Rev.*, C86:044904, 2012.
- [41] T. Nonaka, T. Sugiura, S. Esumi, H. Masui, and X. Luo. Importance of separated efficiencies between positively and negatively charged particles for cumulant calculations. *Phys. Rev.*, C94(3):034909, 2016.
- [42] X. Luo. Unified Description of Efficiency Correction and Error Estimation for Moments of Conserved Quantities in Heavy-Ion Collisions. *Phys. Rev.*, C91(3):034907, 2015.
- [43] X. Luo and T. Nonaka. More simple efficiency correction procedures for cumulants of multiplicity distributions in heavy-ion collisions. *Phys. Rev.*, C99:044917, 2019.
- [44] Nonaka T., M. Kitazaw, and S. Esumi. More efficient formulas for efficiency correction of cumulants and effect of using averaged efficiency. *Phys. Rev.*, C95(6):064912, 2017.
- [45] V. Skokov et al. Volume Fluctuations and Higher Order Cumulants of the Net Baryon Number. *Phys. Rev. C*, 88:034911, 2013.
- [46] X Luo and N. Xu. Search for the QCD Critical Point with Fluctuations of Conserved Quantities in Relativistic Heavy-Ion Collisions at RHIC : An Overview. *Nucl. Sci. Tech.*, 28(8):112, 2017.
- [47] X. Luo. Error estimation for moment analysis in heavy-ion collision experiment. *Nucl. Part. Phys.*, 39:025008, 2012.
- [48] X. Luo et al. Volume Fluctuation and Autocorrelation Effects in the Moment Analysis of Net-proton Multiplicity Distributions in Heavy-Ion Collisions. *Nucl. Part. Phys*, 40:105104, 2013.
- [49] R. Barlow. Systematic errors: Facts and fictions. In *Advanced Statistical Techniques in Particle Physics. Proceedings, Conference, Durham, UK, March 18-22, 2002*, pages 134–144, 2002.
- [50] P. Sarma and B. Bhattacharjee. Color reconnection as a possible mechanism of intermittency in the emission spectra of charged particles in PYTHIA-generated high-multiplicity pp collisions at energies available at the CERN Large Hadron Collider. *Phys. Rev. C*, 99:034901, 2019.
- [51] A. O. Velasquez and P. Christiansen. Color Reconnection and Flowlike Patterns in pp Collisions. *Phys. Rev. Lett.*, 111:042001, 2013.
- [52] P. Braun et al. Bridging the gap between event-by-event fluctuation measurements and theory predictions in relativistic nuclear collisions. *arXiv*, 2016.
- [53] V. Koch A. Bzdak and V. Skokov. Baryon number conservation and the cumulants of the net-proton distribution. *Phys. Rev. C.*, 87:014901, 2013.
- [54] ALICE Collaboration. Global baryon number conservation encoded in netproton fluctuations measured in Pb-Pb collisions at $\sqrt{s_{NN}}=2.76$ TeV. *Phys. Lett. B*, 807:135564, 2020.
- [55] K. Fukushima. Hadron resonance gas and mean-field nuclear matter for baryon number fluctuations. *Phys. Rev. C*, 91:044910, 2014.